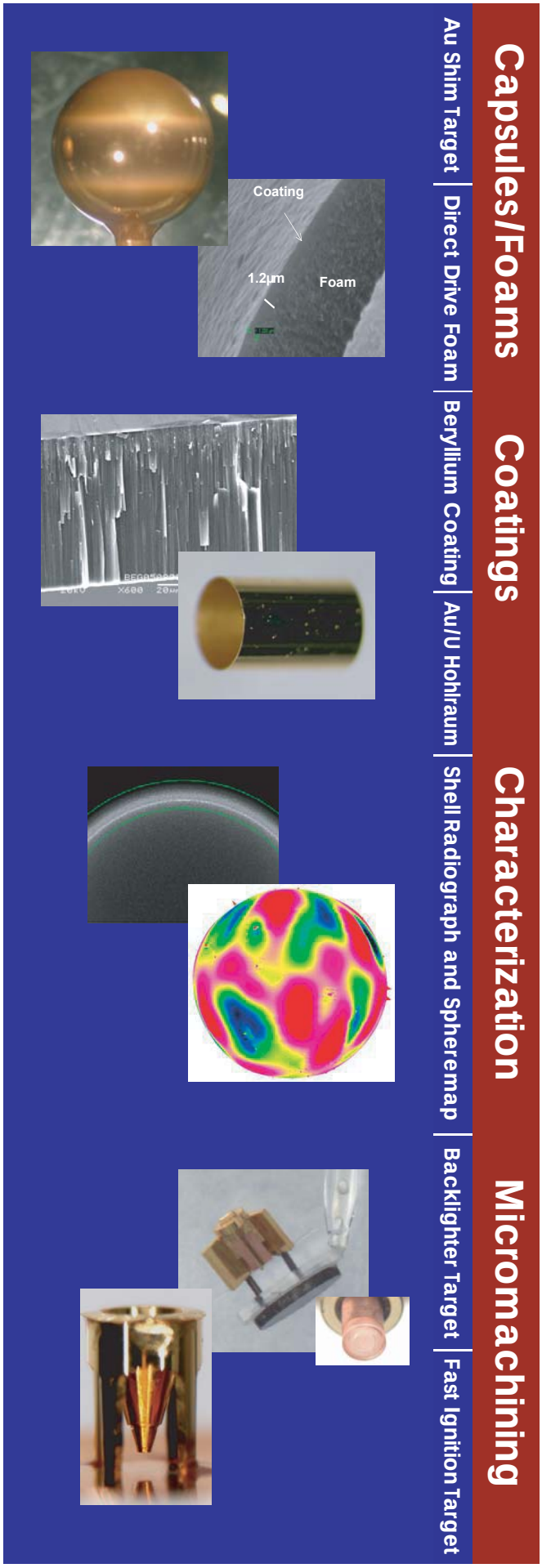

GA-A25242

INERTIAL CONFINEMENT FUSION

Annual Report

October 1, 2004
Through
September 30, 2005

Schafer

GENERAL ATOMICS

DISCLAIMER

GA–A25242

INERTIAL CONFINEMENT FUSION TARGET COMPONENT FABRICATION AND TECHNOLOGY DEVELOPMENT SUPPORT

ANNUAL REPORT TO THE U.S. DEPARTMENT OF ENERGY

OCTOBER 1, 2004 THROUGH SEPTEMBER 30, 2005

by
PROJECT STAFF

J.F. Hund, Technical Editor

Work prepared under
Department of Energy
Contract No. DE-AC03-01SF22260

GENERAL ATOMICS PROJECT 30095
DATE PUBLISHED: DECEMBER 2005

GENERAL ATOMICS

ACRONYMS

AFM	atomic force microscope
CDR	Conceptual Design Report
CPL	cryogenic pressure loader
CRF	carbonized resorcinol formaldehyde
CTM	cryogenic target mount
CW	continuous wave
D_2TS	deuterium test system
D-GDP	deuterated polymer
DT	deuterium-tritium
DTRA	Defense Threat Reduction Agency
DVB	divinylbenzene
EDAX	energy dispersive x-ray analysis
EOS	equation of state
FI	fast ignition
GA	General Atomics
GDP	glow discharge polymer
H-L	half-life
HD	hydrogen deuteride
HEDP	high energy density plasma
I-TIC	ignition-target inserter and cryostat
ICF	Inertial Confinement Fusion
IDL™	Interactive Data Language
IFE	Inertial Fusion Energy
IFT	Inertial Fusion Technology
ILE	Institute of Laser Engineering, Japan
IPA	isopropanol
IR	infrared
LANL	Los Alamos National Laboratory

LEH	laser entrance hole
LLNL	Lawrence Livermore National Laboratory
MS	mass spectrometer
NCTS	NIF Cryogenic Target System
NIF	National Ignition Facility
NNSA	National Nuclear Security Administration
NRL	Naval Research Laboratory
PAMS	poly-α-methylstyrene
PCHMS	polycyclohexyl-methylsilylene $C_7H_{14}Si$
PVA	polyvinyl alcohol
PVP	polyvinylphenol
rf	radio frequency
RF	resorcinol formaldehyde
RT	Rayleigh-Taylor
SEM	scanning electron microscopy
Si-GDP	silicon-doped glow discharge polymer
SM	spheremapper
SM/WM	spheremapper/wallmapper
SNL	Sandia National Laboratory
TARPOS	TARget POSitioner
TGA	thermogravimetric analysis
TIC	target insertion cryostat
TMG	tetramethyl germanium
TPX	commercial designation of the polymer produced by the polymerization of 4-methylpentene-1
UR/LLE	University of Rochester Laboratory for Laser Energetics
UV	ultraviolet
WBS	work breakdown structure
WETF	Weapons Engineering Tritium Facility
WM	wallmapper
XRF	x-ray fluorescence

TABLE OF CONTENTS

EXECUTIVE SUMMARY ..... **iii**

1. INTRODUCTION **1**

2. DELIVERIES **5**

2.1. Overview 5
2.2. Capsule Support for LANL 6
2.3. Capsule Support for LLNL 7
2.4. Capsule Support for SNL 8
2.5. UR/LLE Deliveries 9
2.6. NRL 10

3. DEVELOPMENT **11**

Characterization

3.1. Using Mass Spectrometry to Characterize Permeation Half-Life of ICF Targets 11
3.2. 3D Surface Reconstruction of ICF Shells After Full Surface Spheremapping 16
3.2.1. Introduction 16
3.2.2. 3D Reconstruction Method 17
3.3. Nondestructive Quantitative Dopant Profiling Technique by Contact Radiography 19
3.3.1. Introduction 19
3.3.2. Precision Digitization 19
3.3.3. Dopant Model 20
3.3.4. Applications 21
3.4. A Novel Technique for Precisely Measuring the Thickness of Witness Plates 23
3.4.1. Introduction 23
3.4.2. Instrument Configuration 23
3.4.3. Sample Analysis 24
3.5. White Light Interferometry for the Optical Characterization of Transparent ICF Shells 26
3.5.1. Introduction 26
3.5.2. Instrument Configuration 26
3.5.3. Shell Analysis 28
3.5.4. System Use 29

Aerogel and Foam Development

3.6. Development of a Production Process for Fabricating Low and High Density Resorcinol Formaldehyde Foam Shells for Direct Drive Experiments 31
3.6.1. Introduction 31
3.6.2. Low Density RF Foam Shells 31
3.6.3. High Density RF Shells 33
3.6.4. Large Pore RF Shells 34
3.7. Controlling the Pore Size and Gelation Time of Resorcinol Formaldehyde Foam for Fabrication of Direct Drive Targets for ICF Experiments 35
3.7.1. Introduction 35
3.7.2. Experimental 35
3.7.3. Discussion 36
3.8. Fabrication and Overcoating of Divinylbenzene Shells using Dual Initiators 40
3.8.1. Introduction 40
3.8.2. Fabrication of DVB Foam Shells 41
3.8.3. Overcoating of DVB Shells 42
3.9. Silica, Metal Oxide, and Doped Aerogel Development for Target Applications 45
3.9.1. Introduction 45
3.9.2. Silica Aerogels 45
3.9.3. Metal Oxide and Metal Doped Aerogels 47
3.10. Complex Planar Foam Targets for Rayleigh-Taylor Experiments 50
3.10.1. Introduction 50
3.10.2. Experimental 51
3.10.3. Laser Machining the Full Density Over-Layer 52
3.10.4. Results and Discussion 53

Beryllium Target Development

3.11. Beryllium Coatings on Spherical Surface for NIF Target Development 55
3.11.1. Introduction 55
3.11.2. Results 55
3.12. Using Focused Ion Beam Technology to Drill Holes in and Attach Fill-Tubes to a Beryllium Ablator 59
3.12.1. Introduction 59
3.12.2. Experimental Technique 59
3.12.3. Experimenal Results 60

Machining and Plating Development

3.13. Micromachining of Fast Ignition Targets 63
3.13.1. Introduction 63
3.13.2. Machining of Cone and Shell 64

3.13.3. Back Machining Gold Cone 64
3.13.4. Assembly of the Target 65
Other Target Development
3.14. The Effect of Corners on Electroplating of Hohlraum Mandrels 67
3.14.1. Introduction 67
3.14.2. Experimental Approach 68
3.14.3. Results and Discussion 69
3.14.4. Future Work 70
3.15. Multi-Layered Depleted Uranium and Gold "Cocktail" Hohlraums 72
3.15.1. Introduction 72
3.15.2. Equipment 72
3.15.3. Results and Discussion 72
3.16. Development of Sputter-Coated Glass Permeation Barrier 75
3.16.1. Introduction 75
3.16.2. Experimental 76
3.16.3. Results and Discussion 76
3.17. Improving the Yield of Target Quality OMEGA Size Poly-α-Methylstyrene Mandrels by Modifying Emulsion Components 80
3.17.1. Introduction 80
3.17.2. Results and Discussions 81
3.18. Vapor-Deposited Polyimide Coatings with Improved Surface Smoothness ... 84
3.18.1. Introduction 84
3.18.2. Wire Net Approach to Eliminate Surface Mechanical Damages 84
3.18.3. Surface Quality of As-Coated Polyamic Acid Shells 85
3.18.4. Surface Quality and Integrity of the Polyimide Shells 87
3.19. Fabrication of Graded Germanium-Doped CH Shells 89
3.19.1. Introduction 89
3.19.2. Control of Germanium Dopant Concentrations and Layer Thickness . 89
3.19.3. Characterization of Graded Germanium-Doped Shells 90
3.19.4. Removal of Mandrel by Pyrolysis 91
Development at Schafer
3.20. Overview of Schafer Target Fabrication in Support of Sandia National Laboratories 94
3.21. Planar Targets for NRL NIKE Laser 101

4. PUBLICATIONS 115

LIST OF FIGURES

1-1. Letter from NNSA administrator 4
2-1. Wallmap of a polymer capsule with a P2 shim 10
3-1. Ion current of deuterium measured on the MS system 12
3-2. Optical microscope images of GDP mandrels 14
3-3. Deuterium half-life at 25°C for bounce-coated and roll-coated shells 14
3-4. Ion current for a deuterium-filled GDP mandrel 15
3-5. Three spheremapper traces 16
3-6. 3D visualization of the process flow steps 17
3-7. PAMS shell surface reconstructed to 5 nm accuracy 18
3-8. Sample noises: 97 μm beryllium sputter coated on a 31 μm thick GDP mandrel 20
3-9. Radiography and XRF measurements 21
3-10. Radiograph analysis of a Ge-doped GDP shell 22
3-11. The physical system for witness plate thickness measurement 23
3-12. Measuring the thickness of a transparent LiF sample 24
3-13. Interferometer view of fringes reflecting off LiF surface and glass block 24
3-14. Optical dispersion causes white light fringes to lose contrast 25
3-15. Diagram of interferometry system 27
3-16. Interference fringes reflected from top surface of shell 27
3-17. Shell surface height measurement points 28
3-18. Comparison of fringe shifts from exact ray trace calculations 30
3-19. A grid of shells ready for diameter and wall thickness measurements 30
3-20. Cross-sectional view of a plasma polymer coating 32
3-21. XRF data on gas retention of RF shells overcoated with GDP 32
3-22. 180 mg/cc RF shells with improper gelation 33
3-23. From batch to batch, roughly 20% to 50% of the shells meet the NC specification of ≤ 5% 33
3-24. SEM images of RF aerogel 37
3-25. Nitrogen adsorption data showing a trend of decreased surface area 37
3-26. The SEM image represents the system with the increased amount of acid 38
3-27. NC data for shells made by route B with controlled gelation times 38

3-28. 2 mm DVB shells made with single initiator 41
3-29. Histogram of the shell wall nonconcentricity of the DVB foam shells 42
3-30. Cross-section of a PVP/GDP overcoated DVB shell 43
3-31. XRF data on gas retention of DVB shells overcoated with PVP/GDP 43
3-32. Silica aerogel shells and beads produced by microencapsulation 46
3-33. Backscatter SEM image of SnO_2 particles in an RF gel 48
3-34. Ion implanted silica aerogel cylinder 48
3-35. Calculated depth profile of 67 mg/cc silica aerogel 48
3-36. Diagram of the diamond machine and cast method to fabricate targets 51
3-37. Diagram of the laser machine method to fabricate targets 52
3-38. Pictures of planar foam targets with a GDP over-layer 52
3-39. Wyko Interferometer images of laser machined targets 53
3-40. Power spectral density analysis of 120 μm laser machined target 53
3-41. A cross-section SEM image of a ~50 μm Be shell 56
3-42. A typical AFM spheremapping power spectrum 57
3-43. A plot of high mode surface roughness RMS versus film thickness 57
3-44. Low magnification in situ SEM image 60
3-45. This SEM image shows a 12 μm diameter, 10 μm deep counter-bore 60
3-46. A glass fill-tube is shown attached via a platinum weld to the tip of the in situ Omniprobe® 61
3-47. A cross-section view of a computer model of a shell-cone fast ignition target 63
3-48. A hollow GDP shell with a machined hole 64
3-49. Examples of two possible conditions encountered when mating cone-shell pairs 65
3-50. A cone-shell fast ignition target 66
3-51. A schematic representation of the electroforming process used to fabricate a hohlraum 67
3-52. The two types of corners that are present in hohlraums 68
3-53. A scanning electron photograph of one of the specimens used in this study 68
3-54. The electroplating setup used at GA for electroplating electroformed hohlraums 69
3-55. The gold electroplated coating on a 6 mm diameter specimen with a 0.2 mm convex corner radius 69

3-56. The gold electroplated coating on a 6 mm diameter specimen with a sharp convex corner radius 69
3-57. The gold electroplated coating on a 6 mm diameter specimen with a 0.2 mm concave corner radius 70
3-58. SEM of electroplated corners 71
3-59. This SolidWorks® diagram of sputter deposition system shows the position of the six guns on the left chamber door 73
3-60. This free-standing, 1.2 mm diameter, 2.1 mm long cylinder is the result of a low-stress cocktail coating on an acrylic mandrel 73
3-61. Auger depth profile of a free-standing cocktail foil 74
3-62. Wall mapping of a typical PVA dip-coated CH shell shows major nonuniformities 75
3-63. The uniformity in SiO_2 coated shells was typically shown to be on the order of a few tenths of a micron 77
3-64. SEM images of ~ 1.5 μm SiO_2 coatings on plasma polymer mandrels 77
3-65. A comparison of typical measured half-lives of roll-coated and bounce-coated shells 78
3-66. The NC of the shells fabricated using the standard OMEGA PAMS process 81
3-67. NC of OMEGA size PAMS shells made with the modifications to the W2 83
3-68. The power spectrum of PAMS mandrel 83
3-69. The improvements made to the OMEGA PAMS shells 83
3-70. The plastic twist wire-net used for holding the shells during coating 85
3-71. Shells prepared with gentle rolling and tapping in solid pan 86
3-72. AFM traces and power spectrum of a shell made with gentle tapping 86
3-73. AFM traces of polyimide shell and power spectrum of polyimide shells 87
3-74. The graded Ge-doped CH shell design for NIF ignition 89
3-75. The contact radiograph image of graded Ge-doped shell 91
3-76. The AFM traces of graded shell show good surface finish at 150 μm thickness... 92
3-77. Contact radiograph images show the mandrel has been removed at 305°C for 10 h 92
3-78. These are graphic representations of the four target types 94
3-79. Double pinch targets from 2003 and 2005 95
3-80. First page of a QA report showing an overview of characterizations, tolerances and “as assembled” notes 96
3-81. Representations of two EOS experiments fielded on Z in 2005 97

3-82. First page of a QA report illustrating an overview of characterizations, tolerances and “as assembled” notes 97
3-83. A representation of the desired fast igniter target 98
3-84. The foam and the radiograph are representative of the target type fielded in 2003 98
3-85. A portion of a QA report for a dynamic hohlraum series 99
3-86. OMEGA targets 99
3-87. The stage portion of the dual theta assembly station 100
3-88. Polyimide gas bag target 101
3-89. Polyimide/gold sandwich films 101
3-90. RF foam with machined sinewave 102
3-91. Filmetric film mapper 103
3-92. NexIV automated measure scope 103
3-93. Ambios stylus surface profiler 103
3-94. Dual theta assembly/characterization station 103

LIST OF TABLES

2-1. First quarter FY05 deliveries 5
2-2. Second quarter FY05 deliveries 5
2-3. Third quarter FY05 deliveries 6
2-4. Fourth quarter FY05 deliveries 6
2-5. FY05 capsule support for LANL 7
2-6. FY05 capsule support for LLNL 8
2-7. FY05 capsule support for SNL 9
3-1. Radiograph and electron microprobe measurements 22
3-2. Density measurements of Be coatings 58

EXECUTIVE SUMMARY

This report documents fiscal year 2005 activity on the U.S. Department of Energy (DOE) National Nuclear Security Administration (NNSA) task order contract for Inertial Confinement Fusion (ICF) Target Component Fabrication and Technology Development Support with General Atomics (GA) and partner/subcontractor Schafer Corporation. Work performed spans development, production, and engineering of planar and spherical targets, target components, and cryogenic systems for the NNSA ICF.

For more than ten years, the GA/Schafer Inertial Confinement Technology team has partnered with the NNSA ICF Laboratories developing and providing targets and related technologies for the ICF program. The team expertise is broad with interests and capabilities in all of the relevant areas of polymer and metal component fabrication, gas filling (including tritium), machining, characterization.

In FY05, the major facilities of the ICF program operated at maximum levels firing well over 2000 shots, most of them requiring well characterized, precise targets. GA/Schafer produced well over 5000 components for the ICF facilities. GA/Schafer are registered in the ISO 9001:2000 program and maintained excellent communication with the users of the targets to continually improve the performance of the team.

In FY05, there was a major change in the target design for ignition highlighting the importance of targets for ignition. For success in ignition, the ICF program requires drivers such as NIF, OMEGA and Z, advanced simulations and targets. A major activity of the ICF program is demonstrating that the demanding cryogenic target for ignition on the NIF can be made and in sufficient quantities. In FY05 as detailed here, GA became a major contributor to the R&D required for the NIC ignition target.

As well as getting extensive and generally very positive feedback from its customers in FY05, the GA/Schafer staff authored over 40 papers in refereed journals and won two prestigious prizes in the ICF program.

Highlights of the GA/Schafer ICF technology work performed under DOE Contract No. DE-AC03-01SF22260 in FY05 comprise the subject of this report. Comments and requests for further information may be directed to the GA Inertial Fusion Technology Program Manager, Joe.Kilkenny@gat.com, (858) 455-3571.

1. INTRODUCTION

This report documents fiscal year 2005 activity of the Inertial Confinement Fusion (ICF) program, which is a research and development activity supported by the U.S. Department of Energy (DOE) National Nuclear Security Administration (NNSA). The goal of ICF research is controlled laboratory implosion of fusionable material to a condition of ignition and propagating burn.

ICF relies on inertia to confine fusionable material, usually a mixture of deuterium and tritium (DT), for the time required to create a fusion reaction. Matter, which reaches this inertially confined state by means of compression from lasers or x-rays, can be considered to be a high energy density plasma (HEDP) for essentially all phases of the process from earliest compression through energy production through replete, extinguishing burn.

The Inertial Confinement Fusion (ICF) Ignition and High Yield Campaign (the ICF Campaign, C10, or "the Campaign") supports the National Nuclear Security Administration's (NNSA's) Stockpile Stewardship Program (SSP). The ultimate goal of C10 is to develop laboratory capabilities to create and measure extreme conditions of temperature, pressure, and radiation, including thermonuclear burn conditions that approach those in nuclear weapons, and to conduct weapons-related research in these environments. Achieving high energy density physics (HEDP) conditions is critical to validate codes and to characterize weapons component performance.

The strategy to accomplish this long-term goal is centered on four objectives:

1. Achieve ignition in the laboratory and develop it as a scientific tool for stockpile stewardship.
2. Support execution of HEDP experiments necessary to provide advanced assessment capabilities for stockpile stewardship.
3. Develop advanced technology capabilities that support long-term needs of stockpile stewardship.
4. Maintain robust national program infrastructure and attract scientific talent to the SSP.

Demonstration of laboratory ignition is the highest priority and a major objective of NNSA.

The components of C10 are: (1) the National Ignition Facility (NIF) Project and the program to achieve ignition (the National Ignition Campaign, or NIC), (2) support of weapons physics, (3) pulsed power fusion and technology, (4) petawatt lasers and fast ignition, (5) inertial fusion energy technology, and (6) university activities. These six components are funded under ten major technical efforts (MTEs). Eight MTEs are in the technical program: MTE 10.1 Ignition, MTE 10.2 Support of Other Stockpile Programs,

MTE 10.3 NIF Diagnostics, Cryogenics, and Experimental Support, MTE 10.4 Pulsed Power ICF, MTE 10.5 University Grants/Other ICF Support, MTE 10.7 Facility Operations and Target Production, MTE 10.8 Inertial Fusion Technology, and MTE 10.10 High-Energy Petawatt Laser Development. Two MTEs are part of the NIF Project: MTE 10.6 NIF Other Project Costs and MTE 10.9 NIF Demonstration Program. The FY 2005 appropriated budget for the ICF program was $536M.

The ICF Campaign is being executed in FY06 at five laboratories: Los Alamos National Laboratory (LANL), Lawrence Livermore National Laboratory (LLNL), Sandia National Laboratories (SNL), Laboratory for Laser Energetics (LLE) at the University of Rochester, and Naval Research Laboratory (NRL). General Atomics (GA) fabricates and characterizes targets and target components and does research and development on target fabrication techniques.

The three major ICF facilities are the OMEGA glass laser at LLE, the Z pulsed-power facility at SNL, and the NIF glass laser at LLNL. Enhancements to Z and OMEGA, called ZR and OMEGA EP, and the plan to complete the NIF are described in Sections Vb and Vc of this Implementation Plan. OMEGA and Z, supplemented by LANL's Trident laser and NRL's Nike laser, currently provide HEDP data for stockpile stewardship. The four-beam version of the NIF provided data to the Science Campaign in FY04. After construction is completed, NIF will be able to provide data in new temperature and pressure regimes close to those in a nuclear weapon.

High energy petawatt (HEPW) lasers are needed for the SSP mission, and NNSA is adopting a phased approach to implementing these capabilities on OMEGA, Z, and NIF.

The ICF Program's four operating facilities were available for a total of 732 days during FY05: 140 days on Nike, 210 days on OMEGA, 149 days on Trident, and 233 days on Z. The OMEGA laser fires about 10 times per day and in FY05 OMEGA fired above 1500 shots. The other facilities fired at least one and sometime more shots per operating. Most of the shots on these facilities required targets which were predominantly made by GA/Schafer. In FY05, GA/Schafer produced 5627 components for these facilities of about 250 different types. Many of the components are novel and were made by techniques requiring significant development. As the targets are the initial conditions for the experiments, the targets and components need to be accurately measured and characterized for each shot. The target is destroyed during the experiment and so characterization cannot be done after the shot.

During FY05, the ICF Program, including GA, prepared a revised plan for NIF activities to be undertaken between FY05 and FY12 related to completion and activation of the NIF, the schedule for ignition and HEDP experiments, and the roles and responsibilities of the ICF laboratories related to the NIF and the National Ignition Campaign (NIC). The written version of this *National Ignition Facility Activation and Early Use Plan* (NIF AEUP) was sent to Congress on June 30, 2005.

A significant portion of the needed R&D and facilitization activities for NIC is focused on the complex target. Although there is significant success in producing characterized

targets for the smaller facilities, there is still major R&D required to produce the targets for the NIC. This is because of the more demanding specification on the ignition targets and the cryogenic capability required for ignition.

In FY06, GA became the major player in the development of the noncryogenic components of the new NIC target. These targets consist of graded doped ablators with very small fill tubes. The specifications on the surface finish, roundness, uniformity, doping fraction, fill tube fillet. etc., are demanding. An accelerated program of R&D and preparing for facilitization to produce hundreds of targets per year is required to ensure the success of the NIC.

As a first step to ensure excellent quality, GA became certified in FY05 to ISO 9001:2000 standards. The two parts of the Schafer organization that GA partner with were registered in FY04 and FY05 also. ISO is an internationally recognized program of Quality Management System. The significance of this standard is well recognized by NNSA as demonstrated in the letter from Ambassador Brooks (Fig. 1-1) the NNSA Administrator.

Department of Energy
National Nuclear Security Administration
Washington, DC 20585

September 21, 2005

OFFICE OF THE ADMINISTRATOR

Mr. E. Michael Campbell
Senior Vice President
GT-MHR, Lasers and Inertial Fusion
General Atomics
P.O. Box 85608
San Diego, CA 92121-1122

Dear Mr. Campbell:

I would like to extend my congratulations to you and the whole General Atomics organization on the achievement of ISO 9001:2000 Quality Management certification. The ISO 9001:2000 Quality Management Principles, including customer focus, supplier coordination, leadership, personnel involvement, process/systems approaches, factual analysis, and especially continuous process improvement, are the hallmarks of an effective organization. The National Nuclear Security Administration is privileged to be among the customers of General Atomics, as we are the beneficiaries of your efforts to continuously improve your organization, customer relations, and products.

Again, congratulations on this important achievement.

Sincerely,

Linton F. Brooks
Administrator

Printed with soy ink on recycled paper

Fig. 1-1. Letter from NNSA administrator.

2. DELIVERIES

2.1. OVERVIEW

GA and Schafer supply a wide range of ICF components to LLNL, LANL, NRL, SNL, UR/LLE, and others. Tables 2-1 through 2-4 summarize these deliveries by quarter.

Table 2-1
First Quarter FY05 Deliveries
(Miscellaneous components are foam assemblies and flat targets)

	Types	Capsules/ Lead Time (days)	μMachined Components/ Lead Time (days)	Miscellaneous
LLNL	28	201/82	122/53	60
LANL	7	30/47	153/49	
NRL	24			145
SNL	13	63/69	79/62	97
UR/LLE	16	237/29	31/55	
Misc.	5		41	___
Total	93	531	426	302

Table 2-2
Second Quarter FY05 Deliveries

	Types	Capsules/ Lead Time (days)	μMachined Components/ Lead Time (days)	Miscellaneous
LLNL	11	528/64	262/54	
LANL	7	46/44	258/44	
NRL	3			136
SNL	10	42/87	24/78	40
UR/LLE	10	337/60	67/26	
Misc.	__			___
Total	41	953	611	176

Table 2-3
Third Quarter FY05 Deliveries

	Types	Capsules/ Lead Time (days)	μMachined Components/ Lead Time (days)	Miscellaneous
LLNL	6	399/56	292/56	
LANL	9	92/82	108/66	
NRL	3			18
SNL	12	21/89	18/34	47
UR/LLE	8	122/53	82/44	1
Miscellaneous	__	55/31		__
Total	38	689	500	66

Table 2-4
Fourth Quarter FY05 Deliveries

	Types	Capsules/ Lead Time (days)	μMachined Components/ Lead Time (days)	Miscellaneous
LLNL	6	412/320	246/45	
LANL	9	50/12	167/52	
NRL	4			112
SNL	12	59/75	26/67	63
UR/LLE	14	113/32	102/40	23
Miscellaneous	6	412/320	246/45	___
Total	45	634	541	198

2.2. CAPSULE SUPPORT FOR LANL

LANL capsule deliveries in FY05 included "routine" as well as developmental targets. The "routine" targets delivered were: ~900 × 3 μm drop tower glass shells, ~900 × 20 μm CH capsules with an embedded titanium-doped layer, ~550 μm o.d. Ge-GDP capsules with embedded PVA layer, and ~1100 × 4 μm deuterium filled Hoppe glass shells. The most significant developmental targets were the first Hoppe glass shells filled with krypton (~900 × 3 μm in size with fills ranging from 0.01 to 1.0 atm Kr mixed with 10 atm of deuterium).

Additional support for LANL included spheremapping of calibration spheres for the LANL micromachining team; and x-radiography and analysis of carbonized resorcinol formaldehyde (CRF) cylinders.

We also set up an assembly station at LLE for LANL for mounting DT-filled capsules. Two GA scientists successfully mounted DT-filled capsules for an LANL campaign on OMEGA using the station at LLE.

Table 2-5 lists the capsules and "samples" provided to LANL in FY05.

Table 2-5
FY05 Capsule Support for LANL

Description	No. of Orders	No. of Capsules
~900 × 50 μm CH shell w/ Ti-GDP embedded layer	1	18
~550 × 50 μm shell w/ PAMS inner mandrel, PVA permeation barrier, Ge-GDP outer layer	2	40
~900 × 3 μm drop tower glass shells	1	40
Kr-filled Hoppe glass shells coated with GDP	1	24
Hoppe glass shells	3	50
1200 μm PAMS shells	1	25
X-radiography characterization of CRF cylinders	1	10
Spheremapping of calibration spheres	1	2
Total	11	209

2.3. CAPSULE SUPPORT FOR LLNL

LLNL target deliveries in FY05 included many "never made before" targets. The "routine" target deliveries consisted of: ~550 o.d. CH capsules with an embedded PVA layer, some with Ti-doped GDP mandrels, others with PAMS mandrel and a Ge-doped GDP outer layer; several varieties of Hoppe glass shells; and several varieties of ~900 o.d. CH capsules.

A significant effort was expended supporting beryllium capsule development for LLNL. Over a thousand two millimeter GDP shells were provided to serve as mandrels for beryllium coating runs at LLNL. Likewise, several batches of tens of 440 μm o.d. GDP shells were provided for production of beryllium capsules of a size suitable for experiments on OMEGA.

Table 2-6 lists the capsules and "samples" provided to LLNL in FY05.

Table 2-6
FY05 Capsule Support for LLNL

Description	No. of Orders	No. of Capsules
~550 × 35 μm shell w/ Ti-GDP inner mandrel, PVA permeation barrier, undoped-GDP outer layer	3	69
~550 × 30 μm shell w/ PAMS inner mandrel, PVA permeation barrier, Ge-GDP outer layer	4	95
2 mm GDP shells for use making beryllium shells	10	~1000
~700 × 50 μm GDP hemi-shells	1	14
Hoppe glass shells coated with GDP	2	18
200 × 8 μm Hoppe glass shells with tailored H-Ls	1	12
440 μm o.d. GDP shells for use making beryllium shells	1	50
~550 × 50 GDP shells for hole drilling development	1	20
Total	23	~1278

2.4. CAPSULE SUPPORT FOR SNL

SNL capsule support in FY05 was extensive. We fabricated 4.7 mm Ge-doped capsules shimmed with gold and developed a new method using our automated microscope to characterize the shim thickness profile.

Two and three millimeter GDP shells were fabricated for SNL having an embedded ~1.5 μm thick glass permeation barrier. We developed the means to permeation fill these shells with ~0.1 atm of argon using high temperature (~200°C) and pressure (~7 atm) fill conditions. We then developed mass spectrometry and XRF to quantify the fills using destructive and nondestructive techniques.

We continued to support efforts to fabricate cryogenic fast ignition targets for SNL. To that end, hemi-shells of various dimensions were fabricated and delivered for this development work.

For the first time, we delivered two millimeter beryllium/GDP composite capsules for experiments on Z. These capsules consisted of ~2 mm × 20 μm GDP shells overcoated with ~30 μm of beryllium. An outside vendor laser machined an ~50 μm hole in the GDP mandrel for gas filling. The hole remained open after beryllium coating and was epoxy sealed in a chamber pressurized with ~20 atm of deuterium and ~0.1 atm of argon. In FY06, we plan to establish in-house capability for laser machining holes, on the order of 10 μm in diameter, into beryllium capsules.

Table 2-7 lists the capsules and "samples" provided to SNL in FY05.

Table 2-7
FY05 Capsule Support for SNL

Description	No. of Orders	No. of Capsules
~4.7 mm Ge-GDP shell w/ gold shim	2	18
~2500 × 50 μm GDP hemi-shells	1	18
~2300 × 4 GDP hemi-shells	1	10
~2000 × 20 μm Hoppe glass shells	1	9
2 to 3 mm × 60 to 80 μm GDP/PVA/GDP shells with assorted gas fills	5	63
2 to 3 mm × 60 to 80 μm GDP shells with embedded glass permeation barrier	3	15
First "sample" of: 2 mm × 30 μm beryllium/GDP shells with DD and Ar fill	1	3
Total	14	136

2.5. UR/LLE DELIVERIES

Our group continues to coordinate delivery of a wide range of targets to LLE. We have continued to deliver virtually all orders on time or before the due date. In 2005 we delivered 1019 targets for 48 separate orders to LLE.

Our goal has been that in time the transitional and developmental targets will become routine. This was the case with the fast ignition targets delivered in 2005. Divinyl benzene (DVB) foam cylinder production also became routine for 100 mg/cc density. We are currently developing 200 mg/cc and 50 mg/cc DVB foams.

Routine types of targets such as plain CH shells are now delivered conforming to tighter specifications. Shells are now routinely delivered in the 15 to 27 μm wall thickness range with walls within ± 0.5 μm of the requested thickness.

Cryogenic experiments at LLE were supported by the production of thin walled "strong" CD capsules. These were analyzed for burst and buckle pressure and wallmapped for wall uniformity. Other deliveries include deuterium filled glass shells and multilayered shells.

One of the most challenging developmental orders for 2005 was the production of full density resorcinol formaldehyde (RF) foam planar targets with a machined sine wave GDP layer.

Targets for NLUF included DVB cylinders for astrophysics experiments. New developments for NLUF included production of polymer capsules with an intentional P2 defect, and polymer beads embedded in precise locations in RF foam cylinders. The P2 targets were used to study the control of the symmetry of direct-drive implosions with target shimming. (A wallmap of one of these targets is shown in Fig. 2-1.) NLUF experimenters also used CH and CD shells and deuterium filled glass shells.

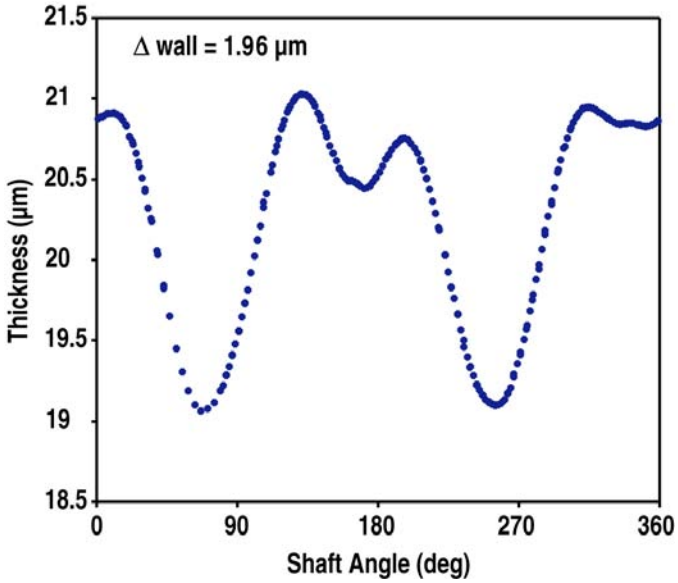

Fig. 2-1. Wallmap of a polymer capsule with a P2 shim.

2.6. NRL

Our group continues to provide extensive support to NRL both in routine targets and completely new target design requests. In spite of short lead times and tightening specifications, we were able to meet all target requests on time.

We continue to provide the standard Nike targets. These targets consist of flat or patterned polystyrene, planar RF foam thin films, patterned RF foam, planar DVB foam and several required coatings.

Many of the standard targets specifications have been tightened. The standard CTM target with polyimide and a micromachined step plate was improved through various micromachining techniques. Combining advances in machining with improved assembly the group was able to improve the standard specification considerably from 3 to 1 μm/mm.

Foam support for NRL has included delivery targets as well as development of new and unique designs and processes to achieve better quality and more uniform foams. The foams produced include DVB flat films, RF flat films, RF rippled films and targets that include RF with a polystyrene film. Recent developments include chemical surface modification on substrates to prevent cast foam films from sticking. This eliminates cracking and surface damage to the foam and produces a very uniform and flat film. Other development areas include making RF films thinner than previously available and making flat CRF films.

For the first time we delivered polyimide gas bag targets. They were fabricated by attaching a spin coated 0.5 μm polyimide film to 3 μm diameter precision machined washer. A 0.001 μm fill tube was attached to the washer which allowed the gas bags to be filled in the target chamber. This developmental effort was accomplished in just under three months.

3. DEVELOPMENT

CHARACTERIZATION

3.1. USING MASS SPECTROMETRY TO CHARACTERIZE PERMEATION HALF-LIFE OF ICF TARGETS

E.L. Alfonso, J.S. Jaquez, and A. Nikroo — General Atomics

Room-temperature shots using plastic shells will require a permeation barrier that greatly increases the half-life of the fill gas. It is important to be able to measure the quality of the permeation barrier so that the gas fill is ensured at shot time. A mass spectrometer-based system was developed to measure the permeability of ICF targets. Previous methods have had inherent difficulties. Tracking the weight change of a gas-loaded shell on a microbalance incurs systematic errors, including microbalance sensitivity of $\pm 0.5\ \mu$g and the possibility of additional weight from debris or adsorbed water. X-ray fluorescence measurements preclude the measurement of low-Z fill gases, such as deuterium. Measuring pressure rise due to a leaking shell in a small volume is only useful for measuring short half-life targets due to outgassing contributions to the measurement. Equally important, the previously mentioned methods are slow to generate data for shells with a long half-life. Finally, calculating half-life by collecting the gas from a crushed shell is destructive, thus requiring measurement on surrogates of the same type [3-1].

Residual gas analysis using a mass spectrometer (MS) is a common analytical procedure. The MS' high sensitivity and ability to detect specific gases makes it an ideal candidate to measure the permeation through ICF targets. A method was developed to translate the ion current resulting from the permeation through a spherical ICF target to the material's permeation half-life. This novel technique is simple, nondestructive, and suitable for measuring targets with short or long half-lives, i.e., very permeable or impermeable target materials, in less than 30 minutes. The data acquired by this MS-based system agreed well with established destructive techniques.

The rate of permeation through a shell wall is proportional to the pressure differential across the wall. The amount of gas inside the volume of the MS is increased by permeation from the shell, and removed by turbomolecular pumping. If gas removal is not conductance-limited, then:

$$I(t) = \alpha \frac{r^3 P_{shell}}{\tau} e^{-t/\tau} \quad , \tag{3-1}$$

where I is the ion current, α is a proportionality constant, r is the shell radius, P_{shell} is the pressure in the shell, t is time, and τ is the permeation time constant. (Half-life = τ ln2.) When τ is large (low permeability materials), $I(t)$ has zero slope over a short period of time, and Eq. (3-1) reduces to:

$$I_0 = \alpha \frac{r^3 P_{shell}}{\tau} \quad . \tag{3-2}$$

The ion current is inversely proportional to the permeation time constant and proportional to the pressure in the shell.

GDP shells with ICF-applicable dimensions have a half-life of a few minutes and thus were candidates to experimentally validate Eq. (3-1). Five similar GDP shells (~2000 μm o.d., ~30 μm wall thickness) from the same batch were filled with deuterium to 5.4 atm. The pressure cell was vented and the shells were measured sequentially in the MS system. The ion current due to the gas permeating out of the shell decays exponentially, as described by Eq. (3-1). A semi-log plot of $I(t)$ for the five shells is shown in Fig. 3-1. The slope of the line is the same for all five shells and all originate at the same value of I_0. The slope of the line yields the permeation time constant. The deuterium half-life was measured to be 4.6 minutes (τ = 0.12 min per μm thickness at 1 mm o.d.). The measured value of the time constant by mass spectrometry was consistent with that measured by other techniques [3-2].

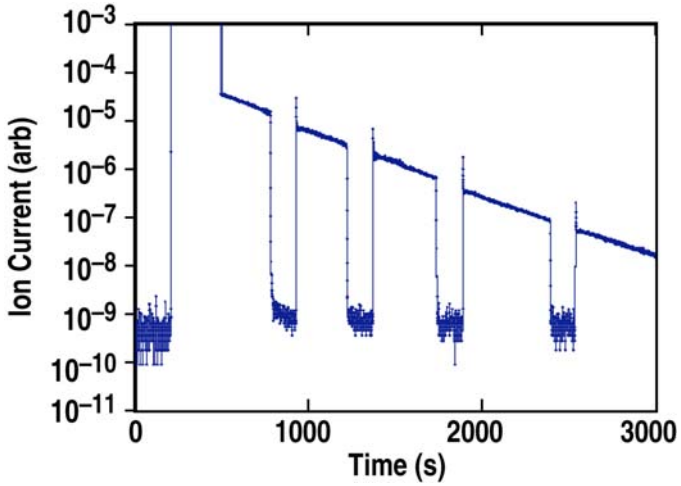

Fig. 3-1. Ion current of deuterium measured on the MS system for room-temperature permeation through GDP shells. Five similar GDP shells from the same batch (~2000 μm o.d., ~30 μm wall thickness) showed the same permeation time constant and origin at I_0. Permeation time constant calculated from $I(t) = I_0 \exp(-t/\tau)$.

The sensitivity of MS makes possible measurement of trace amounts of gas permeating from the shell. As seen in Fig. 3-1, the measurement occurs over 50 minutes (7.5 τ). The shell pressure is 1/1800 of its original pressure, yet the ion current is an order of magnitude

greater than the background noise. Thus, it may be possible to measure shells with half-lives as low as 20 s.

The ability to measure the permeation of a shell with a half-life of several days or greater is a more valuable tool. The use of Eq. (3-1) is unsuitable because the ion current has no measurable slope in the short time frame of the measurement. For relatively large half-lives, however, the time constant can be calculated from the initial value of the ion current signal on the MS, as expressed in Eq. (3-2). The value of the coefficient α must be measured before analyzing the sample shells to correctly calculate the half-life of the sample.

The experimental validation of Eq. (3-2) was performed using a shell with a long half-life as a reference. This shell was a polyvinylalcohol/sputtered aluminum-coated GDP with a room-temperature deuterium half-life of 6 days as measured by weighing. This shell was filled to several pressures and measured at each fill pressure with the MS system. A plot of I_0 versus P_{shell} yielded a straight line. The slope of the line gives the coefficient α. Due to daily fluctuations of the MS, a reference shell must be measured to calculate α along with the sample shells.

The half-life of a sample shell can be calculated by comparing its resultant ion current with that of the reference shell with known permeability. Both the sample and reference shell are filled and their individual pressures are given by $P_{i,shell} = P_{cell}[1 - \exp(-t/\tau_i)]$, where P_{cell} is the permeation cell pressure. Using Eq. (3-2), the initial ion current I_0 is measured for both the sample and reference shells and the unknown time constant can be found iteratively.

ICF targets with long permeation half-lives were developed for room-temperature experiments. Polyvinylalcohol (PVA) has been used successfully as a permeation barrier for Nova shells [3-3]. However, PVA's long fabrication time, low yield, and relatively large (up to 50%) thickness nonuniformity make it less desirable for NIF- and SNL-size capsules. More importantly, their room-temperature deuterium half-lives are typically less than one week. As an option, thin sputtered glass layers have been explored as a permeation barrier [3-4]. Optimized processing conditions have allowed us to deposit thin, uniform glass layers on plasma polymer shells with better quality than previous efforts [3-5]. The mandrels (~2000 μm o.d., ~30 μm wall thickness) were bounced or rolled in a pan during sputtering to randomize their surfaces and achieve a uniform coating. Glass thicknesses of 0.5 to 1.6 μm were deposited. The bounce-coated shells had many visible surface domes which most likely originated from collision-induced seeds that grow as coating proceeds [3-6]. These domes could allow a gross diffusion pathway in addition to standard bulk and grain boundary diffusion. The roll-coated shells displayed few of these features. Optical images of bounce-coated and roll-coated shells are shown in Fig. 3-2.

A group of bounce-coated and roll-coated shells (1.6 μm glass layer) were filled with deuterium to ~6 atm. Their half-lives were first measured (nondestructively) on the MS system, and then measured by (destructively) crushing the shells into a small volume. The agreement of the data sets is shown in Fig. 3-3. This gives confidence in the MS measurements because the crushing measurement has been shown to be an accurate measure

of fill pressure (and thus half-life). The half-lives of roll-coated shells are 10 or more times greater than those of bounce-coated shells. Bounce-coated shells typically had a room temperature deuterium half-life of 1 to 2 days. Roll-coated shells had measurable half-lives of 15 to 40 days. Some roll-coated shells had half-lives much longer than 5 weeks, as their ion current signal was so low as to be obscured in the instrument background noise. As shown in Eq. (3-2), the time constant is inversely proportional to the ion current; thus, very low signals can mean the time constant is very large. The actual value depends on the ion current value of the reference shell; in these cases with very low signal, only a lower bound on the half-life can be calculated.

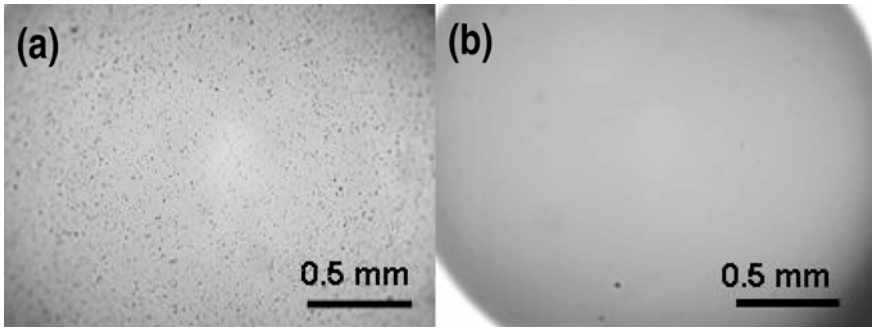

Fig. 3-2. Optical microscope images of GDP mandrels overcoated with a sputtered glass layer. The mandrels were (a) bounced or (b) rolled during the sputtering process. The bounced shell had many surface domes which grew from collision-induced defects. The rolled shell incurred fewer collisions, thus displaying a smooth surface similar to the original GDP mandrel. The deuterium half-life at 25ºC of bounce-coated shells was 1 to 2 days, while the half-life of roll-coated shells was 15 to 40 days.

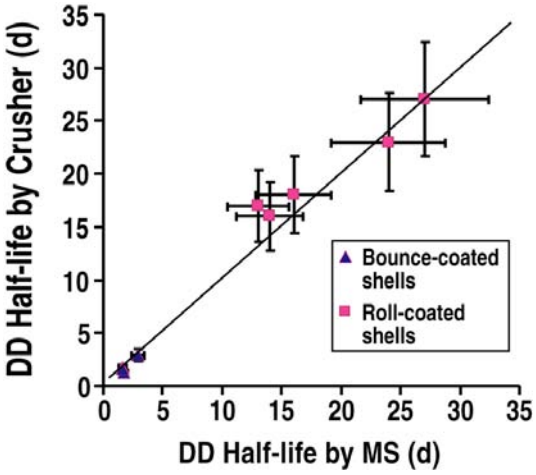

Fig. 3-3. Deuterium half-life at 25ºC for bounce-coated (▲) and roll-coated (■) shells as measured by the MS and crusher systems. The agreement of the data is shown with 20% error bars. The MS system measurements agree well with destructive testing.

The MS system has the capacity to heat the sample shell holder during operation to measure permeation at elevated temperatures. The glass-coated shell was measured at room temperature, then the sample holder was heated to 100ºC, 150ºC, and 200ºC, sequentially. Shown in Fig. 3-4 is the ion current for a deuterium-filled GDP mandrel (~2 mm o.d., 1.6 μm glass layer) at various temperatures. At 25ºC, the ion current is obscured by the instrument noise. The signal increases upon heating due to increased gas permeation. Plotting $\ln(I_0/T)$ versus $1/T$ yielded a linear plot, showing the glass layer follows $\sim\exp(-E/RT)$ behavior in this temperature range.

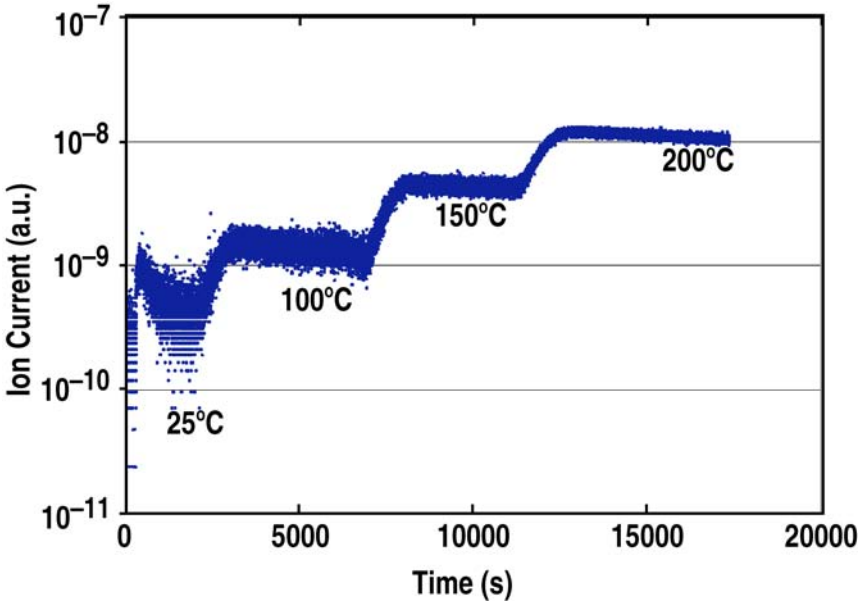

Fig. 3-4. Ion current for a deuterium-filled GDP mandrel (~2 mm o.d., 1.6 μm glass layer) at various temperatures. The signal becomes measurable for long half-life targets at elevated temperatures.

Knowing the half-life at elevated temperatures allows appropriate fill schedules to be developed. From the activation energy data, the deuterium half-life at 150ºC was about 5 to 15 h. Similar glass-coated shells were filled to 20 atm at 150ºC for 40 h and were shown to be $>97\%$ full as measured by destructive testing.

3.2. 3D SURFACE RECONSTRUCTION OF ICF SHELLS AFTER FULL SURFACE SPHEREMAPPING

H. Huang, R.B. Stephens, J.B. Gibson, and I. Valmianski — General Atomics

3.2.1. Introduction

Rayleigh-Taylor instability mandates very stringent surface finishing requirement on ICF shells [3-7 to 3-9]. Surface characterization techniques have not been adequate to satisfy these specifications. The workhorse spheremapper instrument can measure surface roughness with nanometer resolution and can detect long wavelength distortion very well. However, the limited actuator range only allows measurement within a very narrow orbit (~80 μm) around the equator. This leaves the user to wonder what defects are missed by the traces measurement and how the shell looks like in three dimensions (Fig. 3-5).

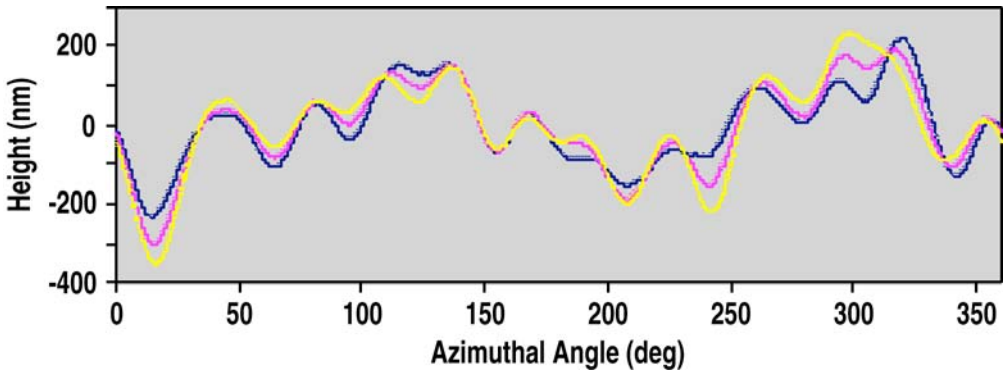

Fig. 3-5. Three spheremapper traces 40 μm apart near the equator of a NIF-sized shell. The orbit is 80 μm wide, close to the maximum possible before spheremapper hardware upgrade.

The first piece of the puzzle is solved with a spheremapper hardware upgrade, which allows 640 μm wide orbit to be measured on a NIF-sized shell. Five such orbits cover over 95% of the shell surface, with no defect with lateral dimension larger than trace spacing goes undetected within each orbit [3-10].

3D surface reconstruction, however, is far from a display problem shown in 2D with the assumption that all traces have the same radius. Spheremapper only measures the height variation, but not the height itself. Mode 0 (average radius) is inherently missing and not necessarily invariant from trace to trace. Mode 1 is partly due to shell misalignment about the rotation axis and partly due to shell distortion. Slight thermal drift, inaccuracy in shell reorientation from orbit to orbit, and imperfection in AFM traces further complicates the problem. As a result, mode 0, mode 1 and some higher mode information must be retrieved for each trace before they are coherent with each other on a nanometer scale. We have developed a mathematical algorithm to reconstruct the entire ICF shell surface to 10 nm accuracy, from which the $R(\theta,\phi)$ map with 1 deg angular resolution can be constructed.

3.2.2. 3D Reconstruction Method

Figure 3-6 visually illustrates the processing flow. Figure 3-6(a) is a straight display of trace data with all artifacts removed. It is apparent that the measured radius is multi-valued on a nanometer scale for reasons discussed earlier. Our approach is to retrieve the missing information by systematically minimizing the height difference at trace intersections. We define the new optimized trace $R^i(\theta)$ as the sum of the measured trace $H^i(\theta)$, the nominal shell radius R_0 (which is trace independent), and the mode correction terms to be determined.

$$R^i(\theta) = H^i(\theta) + R_0 + A_0^i + \sum_{k=1}^{km} [A_k^i \sin(k\theta) + B_k^i \cos(k\theta)] \quad , \tag{3-3}$$

where i is the trace index and k is the mode index. A_0^i is the mode 0 correction for trace i. All higher-mode corrections have two orthogonal components, with amplitudes specified by A_k^i and B_k^i. The mode coefficients are the unknown variables to be solved through an iterative process during which traces from one orbit at a time are held constant while the intersecting traces are adjusted. The convergence is quick and unique resulting in the traces closely retaining the original shape.

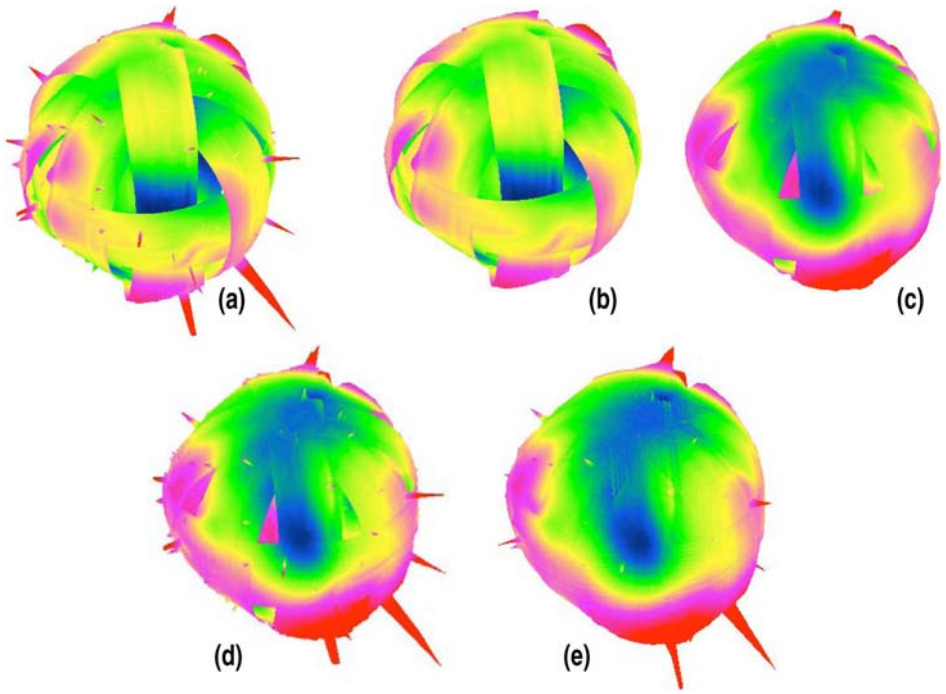

Fig. 3-6. 3D visualization of the process flow steps with all distortions magnified 300x. (The tallest defect 2.5 μm in height.) (a) Step 1: 3D Display of artifact-free data showing the intrinsic incoherency of spheremapper traces. (b) Step 2: All sharp features temporarily removed. (c) Step 3: Low-mode surface optimized by minimizing height difference at trace intersections. (d) Step 5: The difference (4 = 3 – 2) is added back to each trace (1) to produce low-mode optimized surface with all the point defects (5 = 1 + 4). (e) Step 6: $R(\theta,\phi)$ map is produced by averaging to one radius per angular coordinate with 1 deg resolution and by extrapolating in small noncovered regions.

The angle misalignment has serious implications to the optimization procedures: If a point defect is picked up by one trace but not the other at an intersection, it does not make sense trying to minimize the height difference. Therefore it is necessary to temporarily remove all point defects, as shown in Fig. 3-6(b) (Step 2 in the process flow) before performing the calculations which yield the low-mode corrected traces, as shown in Fig. 3-6(c) (Step 3). The change in each trace is captured in a difference file (4 = 3 – 2), which is added back to Fig. 3-6(a) (Step 1) to produce the low-mode optimized surface that retained all point defects, as shown in Fig. 3-6(d) (Step 5 = 1 + 4). We then produce the $R(\theta,\phi)$ map by averaging to one radius per 1 deg angular coordinate and by extrapolating into small noncovered regions, as shown in Fig. 3-6(e) (Step 6).

The most important application of the $R(\theta,\phi)$ map is target implosion simulation. The map can be used as realistic input conditions for the Hydro simulation code to predict the target performance prior to a shot, with the simulated result compared against the actual target performance to further our understanding on implosion physics. The $R(\theta,\phi)$ map also provides characterization feedback to the production engineer for process feedback. As an example, the shell in Fig. 3-5 is 3D reconstructed to 5 nm accuracy in Fig. 3-7. The shell has a pronounced mode 2 distortion that hides the extent of the mid-mode pattern. When modes < 6 are removed, the mid-mode Marangoni pattern becomes conspicuous. These surface patterns are caused by within-the-wall convection cells formed during the PAMS drying process [3-11, 3-12]. The amplitude is intimately linked to the process conditions and can be completely tuned out through process optimization.

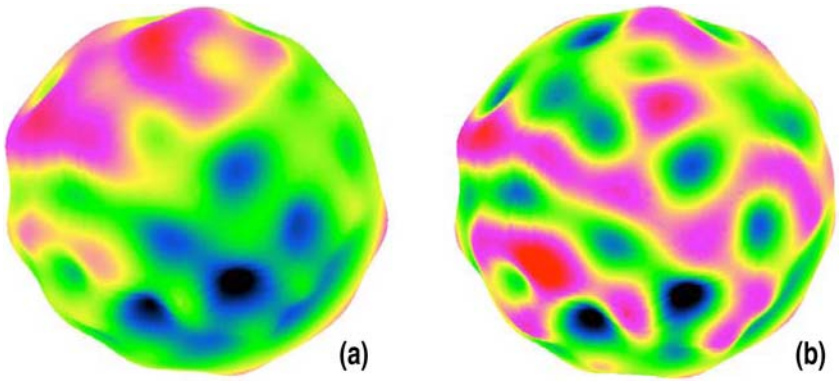

Fig. 3-7. PAMS shell surface reconstructed to 5 nm accuracy showing distinctive mid-mode process defects (distortion magnified by 300x). (a) All modes. (b) Mode 5 and below removed.

Our current focus is to reduce the angular uncertainty in shell repositioning through hardware improvement. If the wobble when releasing a shell can be reduced from 3 to 5 deg to 2 deg, we expect the reconstruction accuracy to be routinely controlled to 5 nm. We plan to use machine vision to provide the feedback and motorized stages to deliver the shell to the precise xyz location.

3.3. NONDESTRUCTIVE QUANTITATIVE DOPANT PROFILING TECHNIQUE BY CONTACT RADIOGRAPHY

H. Huang, R.B. Stephens, S.A. Eddinger, A. Nikroo, K.C. Chen, H.W. Xu — General Atomics

3.3.1. Introduction

We have developed the only nondestructive technique to profile graded dopants in ICF shells to the precision required by the NIF specifications (doping level must be accurate to 0.03 at. % and its radial distribution accurate to submicron precision). This quantitative contact radiography method was based on precision film digitization and a dopant simulation model. The measurements on Cu/Be and Ge/CH shells agree with those from electron microprobe and x-ray fluorescence.

3.3.2. Precision Digitization

X-ray film is an efficient photon detector. We choose the Microchrome Technology's Type K1a film, which has the emulsion on glass substrate to support our stringent dimension requirement. The film has a grain size less than 0.5 μm and covers a large dynamic range (o.d. > 5). In this project, we have developed the imaging equipment and analysis techniques needed to perform quantitative digitization. Three important aspects are discussed here:

1. **CCD Camera.** CCD arrays allow us to measure small shells with the required resolution and field of view. We maximize the intrinsic CCD dynamic range with the selection of a scientific-grade cooled CCD camera with a ~9 electrons-per-pixel read noise. When combined with shutter speed variation, the camera is capable of linearly covering the entire optical density range of the film. A special "Honeycomb" fiber-optics lamp house combined with CCD flat-field correction reduces light fall off to ~0.1% level.

2. **Lens.** Even the best lens has unacceptable spatial distortion for our purposes. For example, a 10X lens can have ~2.5 μm pincushion distortion towards the edge of the CCD array and > 5 μm towards the corner, which if left alone would produce major errors in radius and shape measurements. We choose PLAN APO lenses for their large numeric aperture, flat image plane, and low chromatic dispersion. We then perform lens-specific correction with a line-patterned Cr-on-glass standard, and built the correction algorithm into the image analysis software. We verify the accuracy of image correction algorithm with a circle-patterned and stainless steel ball with NIST traceable diameters.

3. **Noise Reduction.** Proper noise reduction is essential to dopant profile analysis. A typical single-line radial profile contains 2% to 3% noise. The noises come primarily from three sources: X-ray photon shot noise, film grain, the sample (Fig. 3-8). However, we take advantage of the circular symmetry and average azimuthally a large

number of line profiles. A larger CCD allows larger noise reduction. However, the CCD size makes it imperative to correct lens error and flatten uneven illumination.

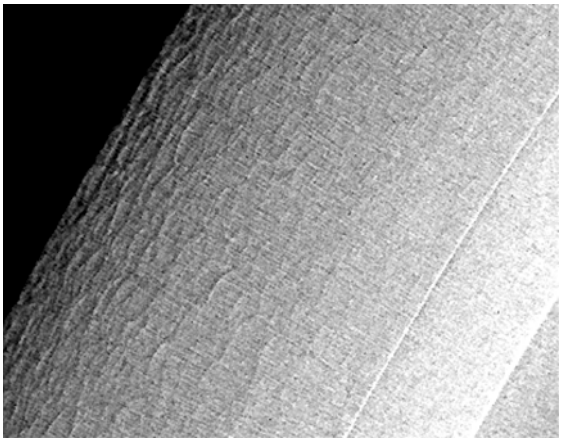

Fig. 3-8. Sample noises: 97 μm beryllium sputter coated on a 31 μm thick GDP mandrel. The tangential chords are due to surface topology (which disappears after polishing) and the radial chords are due to columnar grain structure.

With proper component selection and error treatment, we have constructed a precision digitizer, which measures dimension with 0.2 μm repeatability, and determines radial transmission profile with $<0.1\%$ noise. This system is sufficient to meet the NIF characterization requirement. However, a model is needed to translate gray-scale into dopant profile.

3.3.3. Dopant Model

For photons with energy E, the film exposure $I(E)$ is proportional to the film spectral sensitivity $F(E)$ and the x-ray transmission along path x, as shown in Eq. (3-4),

$$I(E) = F(E) \cdot Exp[-\int \mu(E, \rho, Z)dx] \quad , \tag{3-4}$$

where μ is the material absorption strength, which is a function of photon energy E, material density ρ and elemental composition Z. For a graded shell, μ is a function of the radius. The total exposure is determined by integration over all photon energies, as shown in Eq. (3-5)

$$I = \int S(E) \cdot I(E)dE \quad , \tag{3-5}$$

where $S(E)$ is the x-ray spectrum. Based on the total exposure I, the optical density D can be calculated if the film property Φ is known.

$$D = \Phi(I) \quad , \tag{3-6}$$

By comparing D in Eq. (3-6) to the measured value, we can determine μ as a function of radius in an iterative process, which gives the dopant concentration profile.

It is evident from this conceptual discussion that the dopant model accuracy depends on our knowledge of the x-ray spectrum, the x-ray flux, the film spectral response and the film exposure response. We measured the x-ray spectrum with a Si-detector and determined x-ray flux to ~3% by co-exposing flat standards with the shells. The film response was calibrated against plastic and copper flat standards. The use of bulk-produced polypropylene (with small 10 μm thickness increment) allows us to accurately sample a wide range of thicknesses and optical densities, which probe a wide range of x-ray spectra and film responses relevant to a typical ICF capsule exposure. In its current state, the model measures the x-ray absorption strength, μ, to better than 10% accuracy for each shell layer, which corresponds to better than 0.03 at. % accuracy for copper and germanium in the two alternative target designs.

3.3.4. Applications

We applied the film model to GDP shells uniformly doped by germanium. The radiography measurement agrees to x-ray fluorescence (XRF) measurement within the 10% error of uncertainty (Fig. 3-9).

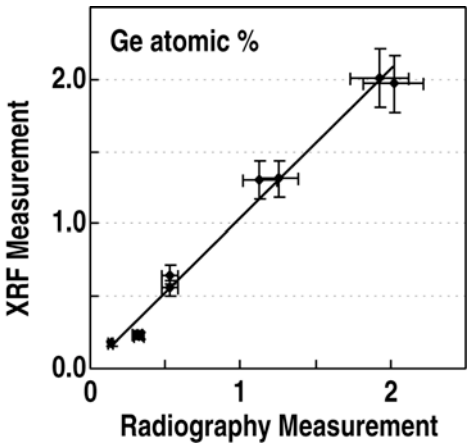

Fig. 3-9. Radiography and XRF measurements agree with each other for uniformly doped germanium dopant in GDP shells.

We then measured graded doped GDP shells. Figure 3-10(a) is transmission profile used to match the calculation to the data and therefore determine dopant concentration. Figure 3-10(b) is the second derivative profile of a partial transmission profile. It shows the first three surface/interfaces as peak/valley pairs. By matching the peak/valley locations, the surface/interface positions can be determined to 0.2 μm. Phase contrast induced phenomena, such as the intensity spike at the inner shell surface in Fig. 3-10(a), is not included in our model. How to obtain the transmission profile and the second derivative profile from local Taylor expansion was reported in earlier literatures [3-13, 3-14].

We then measured graded doped Be shells. In a blind experiment on a graded shell, radiography predicted the dopant levels at half the targeted values. This finding was later confirmed through destructive electron microprobe measurement (Table 3-1). The unexpectedly low doping level was attributed to a bias change in the sputtering settings.

At its current stage of development, radiography can quantitatively measure the material absorption strength (as a function of radius) but is unable to identify individual elements. Therefore, the effect of "unknown" contaminant will be rolled into the error budget. As a rule of thumb, an uncertainty of ± 1 at. % oxygen in GDP shells would lead to an uncertainty of ± 0.05 at. % in germanium; and an uncertainty of ± 0.1 at. % in argon in Be shells would lead to an uncertainty of ± 0.05 at. % in copper.

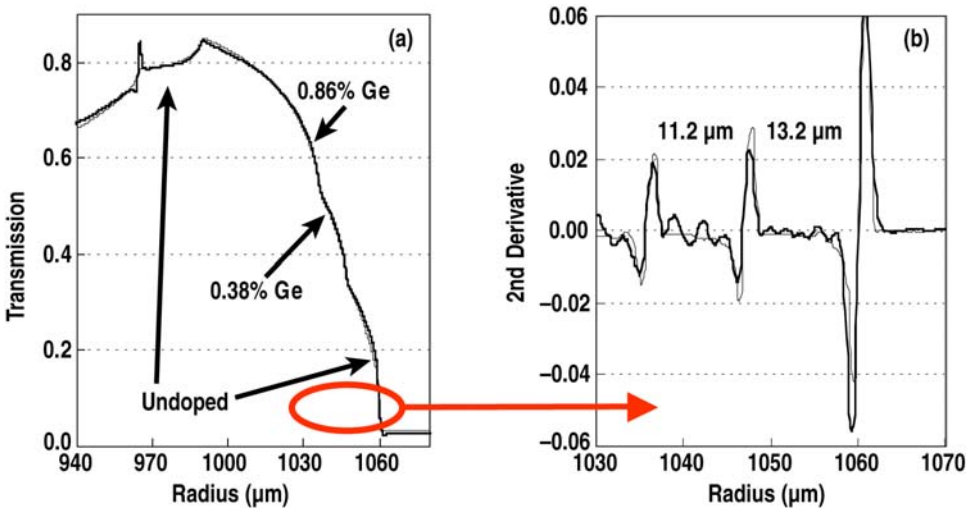

Fig. 3-10. Radiograph analysis of a Ge-doped GDP shell. (a) Transmission gives dopant concentration to 10% (b) second derivative with simulation gives interface to 0.2 μm.

Table 3-1
Radiograph and Electron Microprobe Measurements Agree with Each Other for Cu Dopant Concentration (at. %) in LLNL "Christmas" Shells

	Radiography (Nondestructive)	Electron Microprobe (Destructive)
Layer 1	0	0
Layer 2	0.16 ± 0.02	0.15 ± 0.02
Layer 3	0.33 ± 0.03	0.30 ± 0.03
Layer 4	0.17 ± 0.02	0.15 ± 0.02
Layer 5	0	0

We can extend our analysis to other samples, such as measuring dopant redistribution and oxygen infusion after pyrolysis, or measuring dopant level in flat samples with the thickness determined independently by another method. This analysis may also be used for measuring interface radius and wall thickness for DVB foam shells where the surface might be too wavy and the contrast too weak for vision-based image processing tools.

3.4. A NOVEL TECHNIQUE FOR PRECISELY MEASURING THE THICKNESS OF WITNESS PLATES

D.A. Steinman, R.B. Stephens, M.L. Hoppe — General Atomics

3.4.1. Introduction

Witness plates fabricated for HED and ICF programs are typically one millimeter squares of aluminum 100 μm thick. Their thickness must be measured to better than 1 μm to precisely determine shock wave velocities. We have developed a simple technique using white-light interferometry of a sample mounted on a precision z-stage to locate surfaces and derive thickness, independent of the index of refraction of the sample.

3.4.2. Instrument Configuration

Figure 3-11 shows the physical system. The sample sits on a glass block mounted on a z-stage with a 2 mm range, whose height is monitored with a highly accurate ($\pm$0.01 μm), long-working-range (5 mm) height sensor [3-15]. The sample is illuminated by white light through a Michelson interferometer objective on a stable microscope [3-16]. Fringes appear where the reflecting surface is nearly the same distance from the objective as the reference mirror. Five to ten fringes are visible, with the zero-offset fringe having the most contrast and neighboring fringes having progressively less contrast. The zero-offset fringe can be set on a reference point (in this case the center of the sample) with an accuracy of approximately one-third of a fringe spacing ($\pm$0.1 μm). The sample is translated vertically with a hybrid manual/piezo micrometer spindle, to bring each surface into focus in sequence.

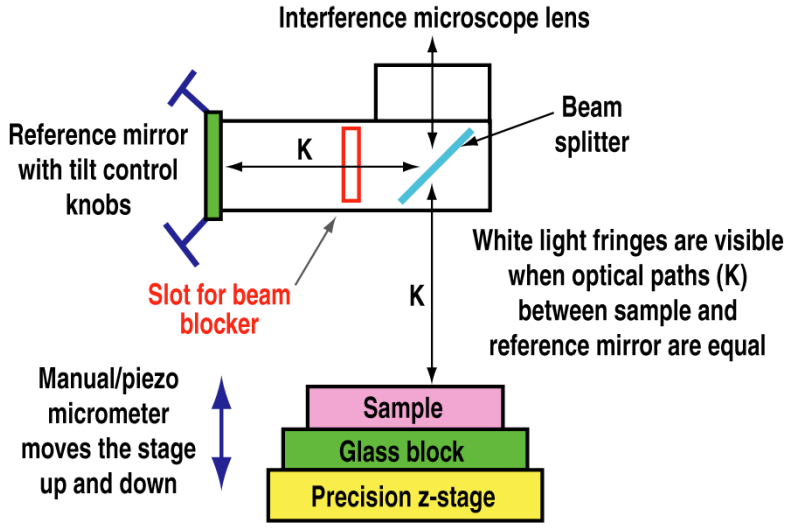

Fig. 3-11. The physical system for witness plate thickness measurement uses a precision z-stage assembly and a Nikon interference microscope.

3.4.3. Sample Analysis

The thickness measurement relies on basic geometry. The witness plate is positioned above an optically flat glass block. The distances from both the top and bottom surfaces of the witness plate to the glass block are measured. The difference between those two measurements is the thickness of the witness plate (see Fig. 3-12).

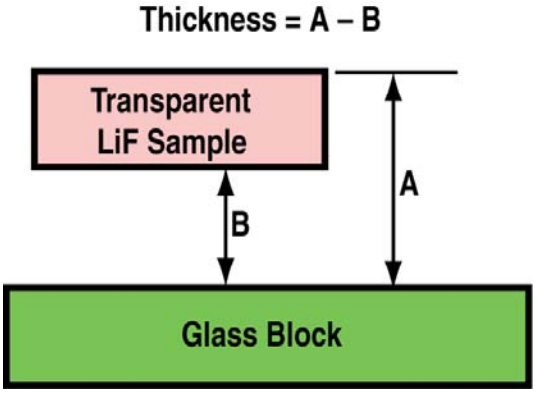

Fig. 3-12. Measuring the thickness of a transparent LiF sample relies on simple geometry as illustrated above.

The measurement from the top surface of the sample to the surface of the glass block is straightforward. Using the white light reference fringes, the spacing between the two surfaces is defined by the z-stage travel (see Fig. 3-13).

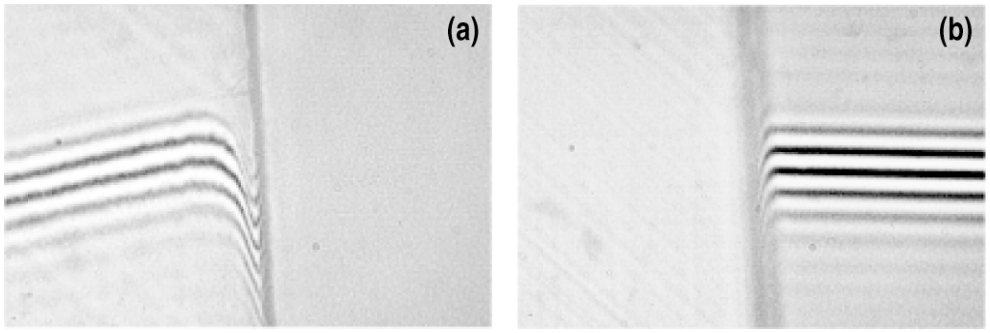

Fig. 3-13. Interferometer view of fringes reflecting off LiF surface (a) and glass block (b). The z-stage is zeroed when white light fringes reflect off the top surface of the LiF sample (a); the stage is then raised until the reference fringes reflect off the glass block (b) thereby defining the vertical separation of the two surfaces.

Our technique requires that the sample be transparent in order to directly measure the spacing between its bottom surface and the glass block. A transparent lithium fluoride sample (about 2 mm^2 and 500 μm thick) meets this requirement. However, the measurement is compromised by optical dispersion. When white light is transmitted through an optical medium such as LiF, optical dispersion causes the color spectrum to shift as a function of wavelength. The net result is that the fringes lose contrast and the reference fringe becomes

ambiguous. We addressed this problem by inserting a glass coverslip into the beam blocker slot of the interferometer lens assembly. We found that a glass coverslip ~200 μm thick has dispersion properties similar to those of the ~500 μm thick LiF sample. With the glass coverslip placed in the microscope reference mirror arm, dispersion was substantially reduced (see Fig. 3-14).

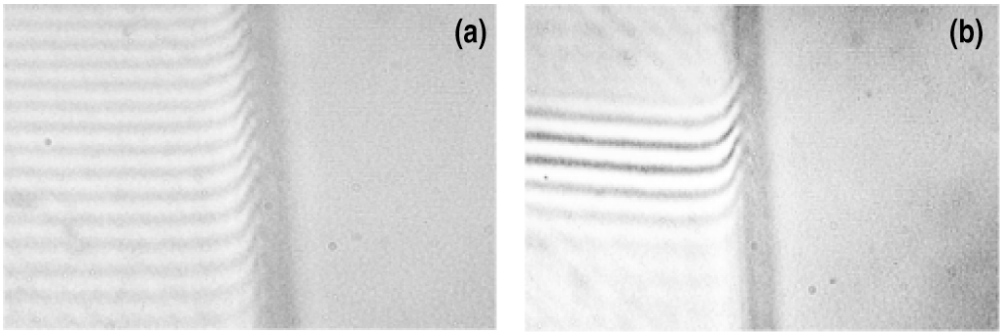

Fig. 3-14. Optical dispersion causes white light fringes to lose contrast as the color spectrum shifts as a function of wavelength for light passing through the LiF sample (a). Inserting a glass coverslip approximately 200 μm thick into the reference arm of the interferometer effectively eliminates dispersion so that a specific reference fringe can again be identified (b).

Likewise, the reference fringe reflecting off the glass block as seen through the transparent LiF sample is readily identifiable with the coverslip in place. Thus, the distance from the bottom surface of the sample to the glass block is determined using the z-stage micrometer system. With the two sets of surface spacing measurements now known, the thickness of the sample is calculated. To test the efficacy of our technique, we measured a LiF sample twenty times. Those measurements gave a sample thickness of 494.7 μm with a standard deviation of 0.04 μm and a range of ± 0.1 μm.

Summary for Section 3.4.

We have developed a new technique that effectively eliminates optical dispersion to characterize transparent witness plates to better than 0.2 μm resolution, using a white light interferometry system — microscope, stage, and height sensor.

The measurement of opaque witness plates uses a modified version of the technique described above. In this case, a tripod of three balls is mounted on the glass block to support the witness plate. To measure the "support height" of each ball, a piece of a glass cover slip is placed on the tripod and a second glass coverslip of equal thickness is inserted into the reference arm of the interferometer. Because dispersion is now essentially eliminated as one looks through the supported coverslip, an accurate measurement can be made of the "support height" of each ball. To find the thickness of the opaque witness plate at each ball contact point, the "support height" is subtracted from the "glass block to top of sample" distance using the reference fringe methodology.

3.5. WHITE LIGHT INTERFEROMETRY FOR THE OPTICAL CHARACTERIZATION OF TRANSPARENT ICF SHELLS

R.B. Stephens, D.A. Steinman, M.L. Hoppe — General Atomics

3.5.1. Introduction

Inertial confinement fusion requires the assembly of DT fuel at 500 g/cc, corresponding to radial compression of the initial fuel pellet by ~20x. A very high level of spherical symmetry — in both drive and areal mass — is required to achieve such high compression. Accurate characterization of both the ablation shell and the fuel layer has long been a major concern of the inertial fusion community. The requirements have evolved over the years; currently a 1 mm diam, 50 μm thick plastic shell to be used in an OMEGA experiment must have wall thickness that varies by < 1 μm (nonconcentricity of inner and outer surface < 0.5 μm). X-radiography, necessary for opaque shells, has proved capable [3-17 to 3-22], but optical interference techniques have proved more suited for rapid evaluation of transparent shells. A wide variety of techniques have been developed [3-23 to 3-28]. In all these cases, measurement of the nonconcentricity of a shell required (1) either rotating it so the offset vector lay in the plane of observation or taking two orthogonal images, and then (2) using the observed fringe pattern(s) to determining actual shell wall nonconcentricity from: fringe offset, duplication of observed fringes using a computer model [3-28] or a proportionality constant valid for a restricted range of shell dimension [3-26].

We have developed a simple system and rapid procedure that allows accurate thickness and nonconcentricity measurements of shells with a very wide range of parameters, without rotating the shell. It utilizes white-light interferometry of a shell mounted on a precision z-stage to locate surfaces and a modeling-derived empirical relationship between fringe off-set and nonconcentricity that is valid for the transparent shells we make. Sections 3.5.2 and 3.5.3 describe the components of this system and the analyses needed to achieve these results. Section 3.5.4 describes the use of this technique.

3.5.2. Instrument Configuration

Figure 3-15 shows the physical system. The shell sits on a mirror mounted on a z-stage with a 4 mm range, whose height is monitored with a highly accurate (±0.01 μm), long-working-range (5 mm) height sensor [3-29]. The shell is illuminated by white light through a Michelson interferometer objective on a stable microscope [3-30]. The image is collected by a ccd camera and displayed on a computer monitor. Fringes appear where the reflecting surface is nearly the same distance from the objective as the reference mirror [Fig. 3-16(a)]. Five to ten fringes are visible, with the zero-offset fringe having the most contrast and neighboring fringes (indicating an offset in height ~0.3 μm) having progressively less contrast. The zero-offset fringe can be set on a reference point (in this case the center spot of the shell) with an accuracy of approximately one-third of a fringe spacing (±0.1 μm). The

shell is translated vertically with a hybrid manual/piezo micrometer spindle, to bring each surface into focus in sequence. The piezo has a range of ~30 μm, allowing smooth translation through the thickness of a shell wall without perturbations caused by touching the spindle or the jumps inherent in stepping motor drives. The stage has a total range of 4 mm, so one can determine the position of all the shell surfaces, top and bottom, in the z-direction. The accuracy of the height sensor (~ ± 0.1 μm over 2 mm) is verified with sapphire spheres (typically < 0.1 μm out-of-round) that have been referenced to NIST standards.

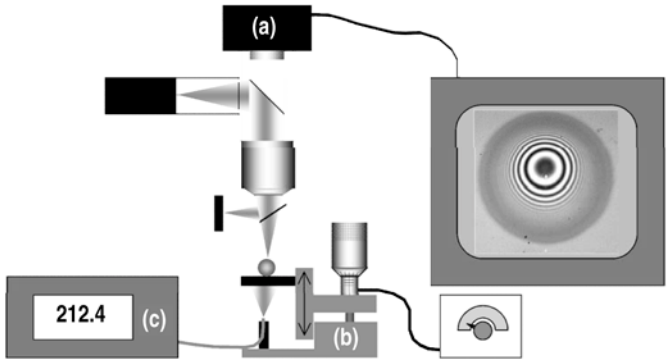

Fig. 3-15. Diagram of interferometry system. A shell is examined under a white light Michelson interference microscope (a) while sitting on a z-stage (b) with a precision height sensor (c) located directly underneath the shell.

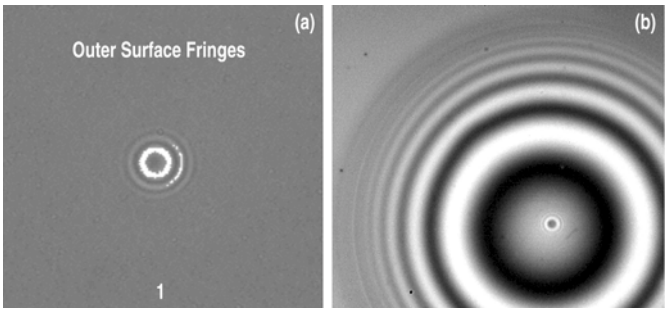

Fig. 3-16. Interference fringes reflected (a) from top surface of shell, (b) from mirror underneath shell.

One can also focus on the fringes from the mirror surface under the shell [Fig. 3-16(b)]. This fringe pattern shows the variation in optical thickness looking through the shell. If the shell is perfect, they will form a bulls-eye pattern centered in the image of the shell. The image center is indicated by a small, circular self-interference pattern where the spherical surface touches the flat mirror (e.g., Newton's rings). Any offset between the center of these fringes and the Newton's rings is assumed to be caused by a transverse nonconcentricity of the interior and exterior shell walls.

3.5.3. Shell Analysis

The apparent vertical position of the surfaces and the offset of the mirror fringes are both strongly affected by the index of refraction of the shell wall. We have developed algorithms that take that effect into account and give actual physical distance.

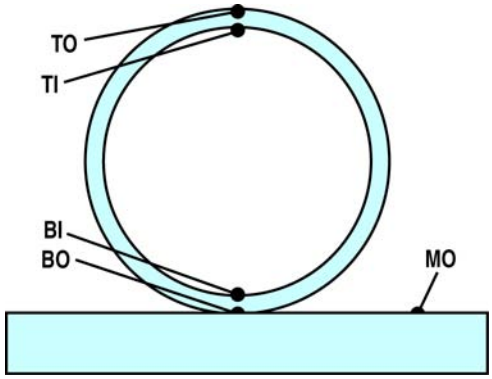

Fig. 3-17. Shell surface height measurement points.

The measurement points are shown in Fig. 3-17. For both of the inside surface measurements (TI, BI) the lens focuses through the same thickness of shell material, so the inside diameter, $ID = TI - BI$, needs no correction (assuming shell is filled with air). Neither of the two outside measurements (TO, MO) are influenced by the shell material, so the outside diameter $OD = TO - MO$. Therefore, the average measured wall thickness is

$$W_{av}^{*} = (OD_r - ID) = 1/2(TO - MO - TI + BI) \quad . \tag{3-7}$$

The outside diameter as measured through the shell, $OD_r = TO - BO$, includes the effect of two shell walls, so the wall thickness calculated using that measurement

$$W_{av}^{*} = (OD_r - ID) = 1/2(TO - BO - TI + BI) = n_{sh} W_{av} \quad . \tag{3-8}$$

Then the wall thicknesses are

$$W_u = (TO - TI)/n_{sh} \quad , \tag{3-9a}$$

$$W_l = (BI - BO)/n_{sh} \quad . \tag{3-9b}$$

So

$$NC_z = 1/2(W_u - W_l) \quad . \tag{3-10}$$

Note that n_{sh} is a number that depends on the details of the spectrum, so is not the same as the index of refraction at any single wavelength $n_{sh} \sim n(\lambda_0) - \alpha \lambda_0$ (where λ_0 is the center wavelength of the detector and $\alpha \equiv \partial n(\lambda)/\partial \lambda$; see Ref. 3-31). Also, the apparent shift in height is exactly $\propto n_{sh}$ only for perpendicular rays [3-32]. However, our microscopes have ultra long working distance objectives, with very small numerical apertures (~0.05), so that correction is insignificant in our case.

The lateral nonconcentricity, NC_{xy}, is determined by offset of fringes from light reflected off the mirror [as in Fig. 3-16(b)]. That is also affected by refraction, in a more complicated way. There is no closed form for that calculation; a power-series description of fringe positions was developed for perfect shells [3-33], but it could not handle nonconcentricity. Analyses have instead used exact ray tracing models to calculate the fringes for a specific case, from which a proportionality constant between fringe offset and nonconcentricity was derived that was valid for a narrow range of shell dimensions [3-26, 3-28].

We have developed an empirical equation that combines the exact ray tracing results with shell parameters in a manner that allows accurate calculation of nonconcentricity from fringe shift over a very wide range of shell parameters using only a single proportionality constant. We hypothesized that the ratio of d/r (fringe offset, d, normalized to shell radius, r) to NC_{xy}/th (shell nonconcentricity, NC_{xy}, normalized to the average wall thickness, th) should be a simple function of the index of refraction. Examination of exact ray tracing calculations of this ratio led us to

$$NC_{xy} = C \times \frac{d}{r} \times \left[\frac{(n-1)}{\sqrt{n}}\right] \times th \quad , \tag{3-11}$$

where $C_{plastic} = 0.367 \pm 0.003$ over a very wide range of plastic shell parameters (Fig. 3-18). A similar analysis gives $C_{SiO2} = 0.284$ for silica shells.

The vertical and horizontal nonconcentricities [Eqs. (3-10) and (3-11)] are added by vector addition, so

$$NC_{tot} = \left(NC_z^2 + NC_{xy}^2\right)^{1/2} \quad . \tag{3-12}$$

3.5.4. System Use

This system has, because of ease of use, replaced the previously used x-radiography (for transparent shells) and fringe-shape analysis. A batch of shells placed in a grid on a mirror (Fig. 3-19) are sequentially characterized for the height of each interface and the offset of the fringes. The measurement z-stage height reading is electronically entered into a spreadsheet that calculates the diameter and nonconcentricity. A grid of shells can be measured at about one shell per minute. Experience with repeated measurements of the same shells in differing orientations show that the NC measurements have an uncertainty of ~1% of the wall thickness, average wall thickness ~0.2 μm, and diameter ~0.5 μm so long as there are no significant higher order mode wall or diameter fluctuations. Wallmapper measurements [3-34], which give a precise measure of the wall thickness and fluctuations on a single equatorial path (not necessarily oriented along the largest nonconcentricity) are in agreement with the simpler measurements described here.

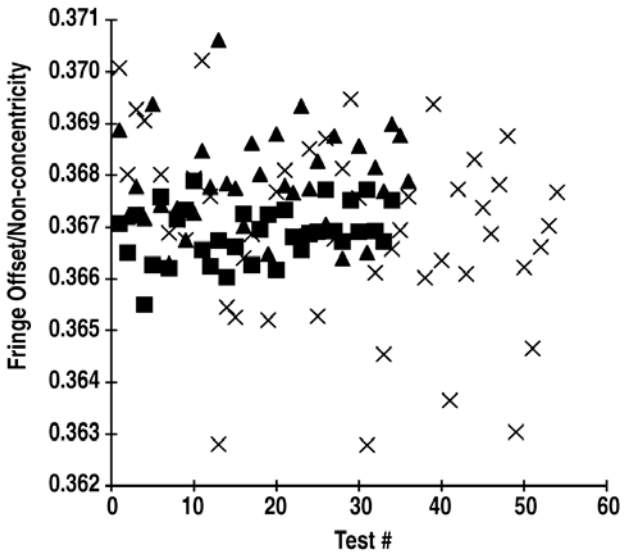

Fig. 3-18. Comparison of fringe shifts from exact ray trace calculations to those predicted by empirical equation for a wide range of shell parameters. The square data points are for a three layer PS/PVA/GDP shell with radius 196 μm viewed in reflection. The thicknesses of these layers varied from 3–4 μm, 2–4 μm, and 30–70 μm, respectively. The triangles and xs are for a two layer PS/GDP shell with radius 300 to 700 μm containing only a PS layer (2 to 4 μm) and a GDP layer (30 to 70 μm) viewed in reflection (triangles) or transmission (xs).

Fig. 3-19. A grid of shells ready for diameter and wall thickness measurements.

Summary for Section 3.5

A white light interferometry system — microscope, stage, and height sensor — has been developed for the characterization of transparent shells. The use of simulation-derived analysis algorithms allow rapid determination of the diameters of the inner and outer surfaces, their nonconcentricity, the location of interfacial layers, the average index of refraction of the walls, and the thickness of discrete layers within the shell wall.

AEROGEL AND FOAM DEVELOPMENT

3.6. DEVELOPMENT OF A PRODUCTION PROCESS FOR FABRICATING LOW AND HIGH DENSITY RESORCINOL FORMALDEHYDE FOAM SHELLS FOR DIRECT DRIVE EXPERIMENTS

R.R. Paguio, C.A. Frederick, J.F. Hund, D.G. Czechowicz, A. Nikroo, M. Takagi,[1] O. Acenas,[2] and M. Thi[3]

General Atomics
[1]Lawrence Livermore National Laboratory, Livermore, California
[2]Cal State University San Marcos, California
[3]University of California San Diego, La Jolla, California

3.6.1. Introduction

Foam shells are needed for and have been used on current direct drive experiments on OMEGA at the Laboratory of Laser Energetics (LLE) and for future experiments on the National Ignition Facility (NIF). The shells needed for OMEGA experiments require diameters of ~ 800 to 900 μm. These are scaled down versions of the targets that are required for high gain wetted foam direct drive ignition designs on NIF [3-35]. The required shell diameter for OMEGA experiments is ~800 to 900 μm. The required wall thickness and foam density depend on the application. Cryogenic targets require a wall thickness of 50 to 100 μm with a foam density of 30 to 150 mg/cc. The room temperature foam shell surrogates, mimicking the D_2 or DT ice layer, need to have a wall thickness of 80 to 120 μm and a foam density of 180 to 250 mg/cc. These targets are designed to reduce the need for difficult to field cryogenic shots with the foam serving to simulate the cryogenic fuel layer. Many types of foam/aerogel systems have been proposed for these wetted foam direct drive experiments. One of these foam systems that has been fabricated and used for these direct dive experiments on OMEGA is resorcinol formaldehyde (RF). This paper will discuss the key factors in shell fabrication using both the low (100 mg/cc) and high (180 to 250 mg/cc) density RF formulations, which are proper chemistry of the foam/aerogel system and proper agitation of the shells/beads during the curing process.

3.6.2. Low Density RF Foam Shells

RF was chosen as the system of choice for foam shell fabrication because of its characteristically small pores ($\gtrsim$0.10 μm), making the foam transparent. This allows use of routine characterization, which is used for full density polymer shells. Fabrication of RF foam shells was developed by Lambert et al. [3-36]. We have extended this work by transforming the process into a repeatable, reliable, high yield production process to fabricate 100 mg/cc RF foam shells [3-37]. Two factors that improved the yield of shells were the gentle agitation of the shells during the curing process, and changes in the chemistry that

slowed down the gelation time. This improved the yield of intact shells from 30% to 95%. Slowing down the gelation time also improved the nonconcentricity

$$\left(NC = \frac{\text{Offset of the Inner} - \text{Outer Wall}}{2(\text{Avg. Wall Thickness})} \right) ,$$

of the shells by giving the shells time to center. By modifying the gelation time, ~30% to 50% of the shells meet the NC specification of < 5%.

A permeation barrier needed to be developed and deposited on the foam shells for gas retention. The permeation barrier that was chosen was glow discharge polymer (GDP) [3-37]. It took approximately 3 to 4 μm of GDP to create a pinhole free permeation barrier (Fig. 3-20). The shells were tested for gas retention by filling them with argon (Ar), and analyzing the shells by x-ray fluorescence (XRF), by following the decay of Ar signal in the shells as a function of time (Fig. 3-21). This has become a standard gas retention technique for the overcoated foam shells. Approximately 60% to 70% of the shells were gas retentive. Developing a production process and permeation barrier for 100 mg/cc RF foam shells enabled the first cryogenic foam shots in the U.S., which produced a yield over clean (YOC) of 100% [3-38].

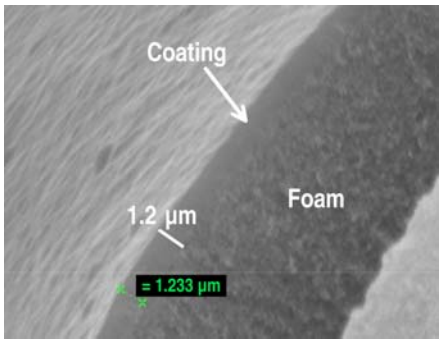

Fig. 3-20. Cross sectional view of a plasma polymer coating (GDP) on a RF foam shell.

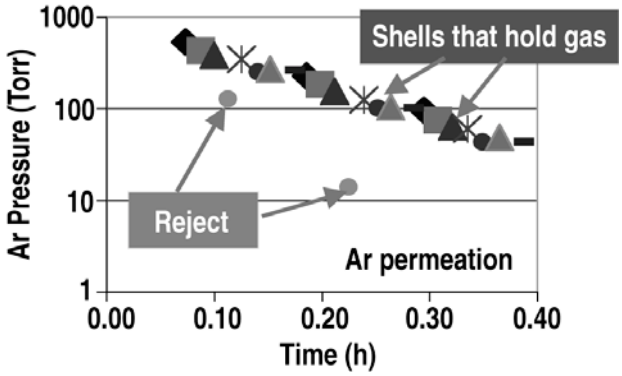

Fig. 3-21. XRF data on gas retention of RF shells overcoated with GDP. The shells that hold gas show that the Ar decays gradually (coating pinhole free), while the rejected shell that does not hold gas decays more rapidly.

3.6.3. High Density RF Shells

We have extended this work to develop a production process for higher density RF foam targets (180 to 250 mg/cc). Again, the gelation time played a key factor in fabricating a high yield of intact shells with good wall uniformity. A gelation time that was too slow or too quick resulted in a low yield of intact RF shells with poor surfaces and bad wall uniformity [Fig. 3-22(a)]. A gelation time similar to that of the 100 mg/cc RF foam shells resulted in high yield of intact shells without wrinkled surface finish which was another usual failure mode in fabrication of these targets [Fig. 3-22(b)].

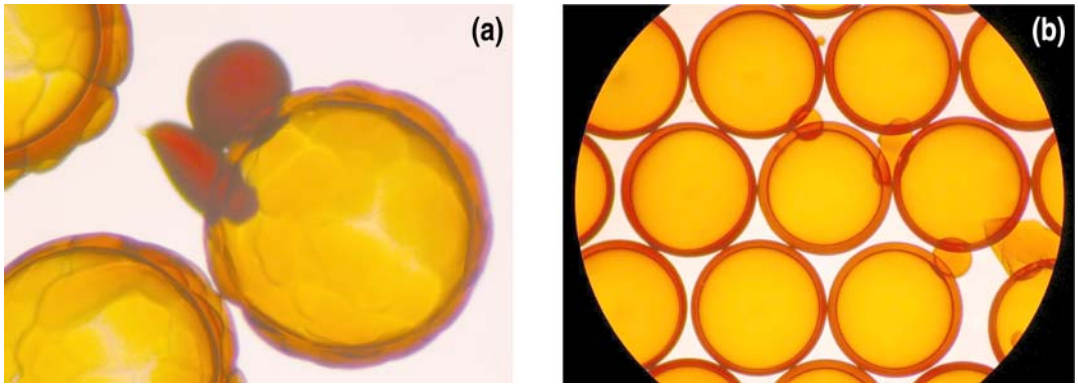

Fig. 3-22. (a) 180 mg/cc RF shells with improper gelation, which leads to shells with bad surfaces (soccer ball type shells). (b) 180 mg/cc RF foam shells with proper gelation, which produces good surfaces and higher yield of intact shells.

Density matching of the inner oil droplet with the RF solution, as well as a gelation time that would give the shells time to center was also key in producing shells with good wall uniformity and NC. Approximately 20% to 50% of the shells analyzed meet the NC specification of ≤ 5% (Fig. 3-23). GDP was also used as the permeation barrier for these high-density RF shells, and the gas retention of these shells is similar to the 100 mg/cc RF shells. This allowed the first gas filled foam shells to be shot at room temperature in the U.S.

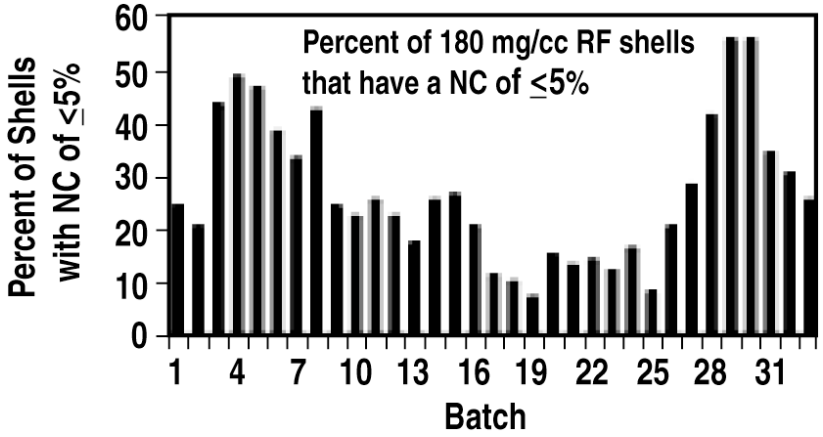

Fig. 3-23. From batch to batch, roughly 20% to 50% of the shells meet the NC specification of ≤ 5%.

3.6.4. Large Pore RF Shells

A direct extension of the work on RF foams shells for direct drive experiments was fabrication of large pore foam shells in order to increase the cryo-fill fraction when these shells were cryogenically layered with D_2. Optical clarity of the D_2 ice layer was severely reduced when the standard RF foam shells were cryogenically layered [3-39]. It was theorized that because the pore size of standard RF foam is < 100 nm, it can lead to under-filling of the D_2. This would cause voids or micro-ice structures that scatter light, reducing the clarity of the ice layer. If larger pore foams were used, it could increase the cryo fill fraction, which could lead to a clearer ice layer. More details on the development and fabrication of large pore RF foam and foam shells will be discussed in another chapter in this report (Section 3.7).

Conclusion for Section 3.6

RF foam targets in the form of shells have been developed and fabricated for direct drive experiments on OMEGA. The fabrication of these foam shells has been developed into production process for both the low and high density RF foam.

3.7. CONTROLLING THE PORE SIZE AND GELATION TIME OF RESORCINOL FORMALDEHYDE FOAM FOR FABRICATION OF DIRECT DRIVE TARGETS FOR ICF EXPERIMENTS

C.A. Frederick, R.R. Paguio, A. Nikroo, J.H. Hund, O. Acenas,[1] M.Thi[2]

General Atomics
[1]Cal State University San Marcos, California
[2]University of California San Diego, La Jolla, California

3.7.1. Introduction

Inertial fusion confinement experiments require spherical foam lined shells. The foam density is typically 100 mg/cc. The shells will be loaded with cryogenic liquid deuterium and tritium (DT) fuel on the inside surface of the shell [3-40]. Resorcinol formaldehyde (RF) was the organic foam chosen to fabricate the spherical shells due to its optical clarity. It is a low-atomic-number foam that will increase laser absorption while also helping to support and symmetrize the fuel during fusion experiments [3-41]. Fabrication of ~ 100 mg/cc "standard" pore foam shells with large enough yield (~ 30%) of target quality shells (wall uniformity < 5%) was demonstrated by Nikroo et al. [3-42]. Problems encountered with the optical clarity of the deuterium ice layer formed in the "standard" pore foam during experiments at the University of Rochester Laboratory for Laser Energetics necessitated fabrication of foam shells with a larger cell size. It was postulated that the small pore size of "standard" RF leads to underfilling of the foam structure with deuterium during the cryogenic layering. This, in turn, leads to scattering centers in the form of small voids inside the ice/foam layer. A larger pore foam should alleviate this problem leading to a more transparent layer.

Therefore, we investigated modifications to the "standard" RF shell formulation to obtain larger pore sized shells. The most substantial factor in the RF chemistry affecting pore size is the molar ratio of resorcinol to carbonate (R/C). We examined reduction of the carbonate concentration (increasing R/C ratio) following the technique developed previously for bulk foam fabrication [3-43]. We shall refer to this technique as route A. In addition, we also examined an alternative route to increasing the pore size by increasing the amount of acid catalyst in the system while keeping the R/C ratio constant. This will be referred to as route B. The second route was needed as route A led to several problems in shell fabrication discussed below. Both routes were then successfully extended to shell fabrication. However, in order to fabricate shells using large pore RF formulations, precise control over the gelation time needed to be developed. In this article, we describe the details of the modifications used to fabricate high quality (NC $\lesssim$ 5%) large pore shells on a regular basis.

3.7.2. Experimental

RF aerogels were synthesized in the usual polycondensation polymerization reaction of resorcinol and formaldehyde in a heated slightly basic solution [3-44]. Briefly, carbonate is

used as the catalyzing agent in the reaction of resorcinol and formaldehyde. Small RF aggregates are then further brought together to form the foam matrix by an acid catalysis step. Benzoic acid is usually added in some excess to the RF solution to achieve this in a more rapid fashion. The gels are then exchanged in isopropanol to remove any remaining water in the porous gel network for the subsequent liquid CO_2 supercritical drying to yield the final foam product. Shells were fabricated using the usual triple orifice generator developed by Takagi [3-45]. For our experiments the molar ratio of resorcinol to formaldehyde remained constant throughout all experiments at 1:2. Variations of the molar ratio of resorcinol to carbonate (R/C) were investigated ranging from 170 (standard ratio), 215, 300, and 450 by decreasing the carbonate amount to obtain large pore RF through route A. For route B, the amount of benzoic acid in the system was increased from 0.110 to 0.177 g while keeping R/C constant at 170.

In addition, a number of characterization techniques were used for pore size distribution determination for route A only (due to time constraints) which included SEM imaging, nitrogen gas adsorption, visible light spectroscopy, and small angle x-ray-scattering (SAXS).

3.7.3. Discussion

Increasing R/C had the most drastic and noticeable effects on the pore size of the RF. With each increasing step in R/C there was a noticeable change in the pore size of the foam. The first experimental indication of these phenomena was the decreased optical clarity of the bulk RF gels. It has been proposed that the decrease in the amount of carbonate in the system allows for larger "clusters" or particles to be formed before they aggregate into networks [3-43]. These larger clusters therefore aggregate into structures of larger size, resulting in larger pores. The SEM images (Fig. 3-24) confirmed these results.

It is visible from the SEM images that with each increasing R/C step there is an increase in pore size. We also used nitrogen adsorption to gain an insight into the distribution of pores in this formulation as shown in Fig. 3-25. As the diameter of the pore structure increases the effective surface area decreases due to geometrical limitations.

This route A formulation was then used in the shell fabrication process. The shells were initially fabricated and cured in the same manner as the standard RF. This led to shells with very large delta wall values ($> 10\ \mu$m) because gelation time had increased substantially and there was not enough time for the shells to "center". Modifications were made to the cure temperature and times in order to better control gelation. In addition, the fast gelation time resulted in the solution often gelling in the droplet generator. Therefore, the initial cure temperature was lowered for a period of time before being raised to the standard cure temperature. Different combinations of cure temperatures and times were tried until the appropriate conditions were found to yield shells with nonconcentricity (NC) $\lesssim 5\%$. The key to obtaining better NC was modifying the process so that the route A formulation gelled at about the same time as the "standard" solution.

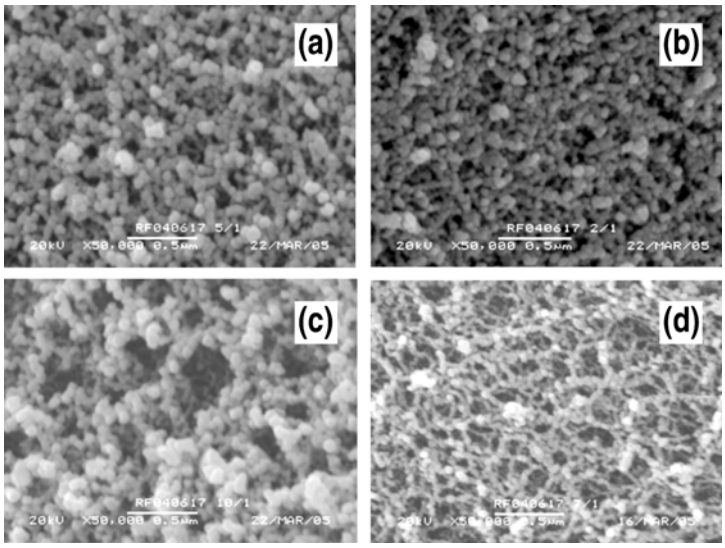

Figs. 3-24. SEM images of RF aerogel made with (a) 5/1 9 (b) 2/1 (c) 10/1 (d) 7/1 resorcinol to carbonate (R/C) ratios.

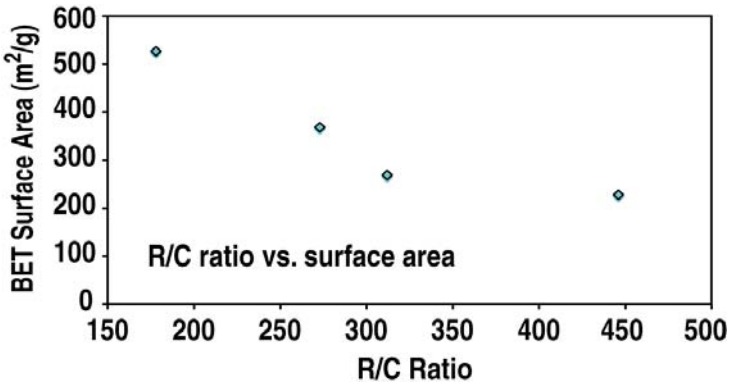

Fig. 3-25. Nitrogen adsorption data showing a trend of decreased surface area with an increase in R/C value for route A.

A number of other issues presented themselves after these shells were supercritically dried. The first was their lack of light transmittance did not allow for white light interferometry characterization. While this was expected due to the larger pore size, it still meant that these shells would have to be characterized with another very time consuming technique such as radiography. More importantly, the density of the dried shells was consistently substantially lower than the calculated value expected. The shells had a measured density of ~ 70 mg/cc rather than the expected calculated 100 mg/cc. Finally, we also encountered a problem in depositing a permeation barrier on these much larger pore shells. The smaller pores of the "standard" formulation shells can be closed with ~ 3 μm glow discharge polymer (GDP) coating [3-42]. But, the route A shells required over 10 μm of GDP to yield gas retentive shells. Despite these issues, gas retentive route A larger pore RF shells were made and sent to LLE to test the under filling hypothesis during cryogenic

layering. In examinations at LLE these shells did indeed lead to a more transparent (characterizable) fuel layer.

Encouraged by the success in improved transparency of the route A shells, we set out to solve the problems associated with these shells. We pursued the above mentioned route B. In this route the R/C was to remain constant at the standardized ratio of 170, to minimize unreacted resorcinol to maintain full density, and the amount of acid catalyst in the system was increased from 0.111 to 0.177 g. Bulk gel samples made using route B did indeed exhibit less optical transparency than the "standard" RF from simple visible inspection. Larger pores are seen in the SEM image (Fig. 3-26).

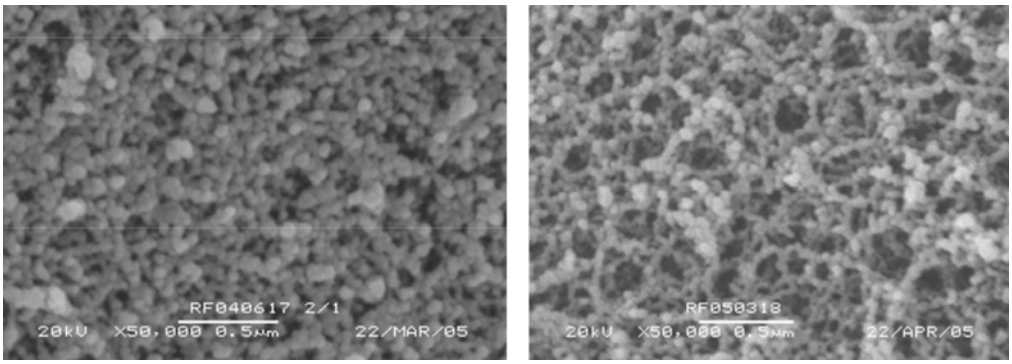

Fig. 3-26. The SEM image represents the system with the increased amount of acid.

Density measurements of dried samples indicated the decrease in density observed with route A shells had been eliminated in route B with the densities agreeing within 5% of the calculated density, which is the same as the "standard" RF case (Fig. 3-27). Also the shells were sufficiently transparent despite the larger pore size for the rapid visible interferometry measurements.

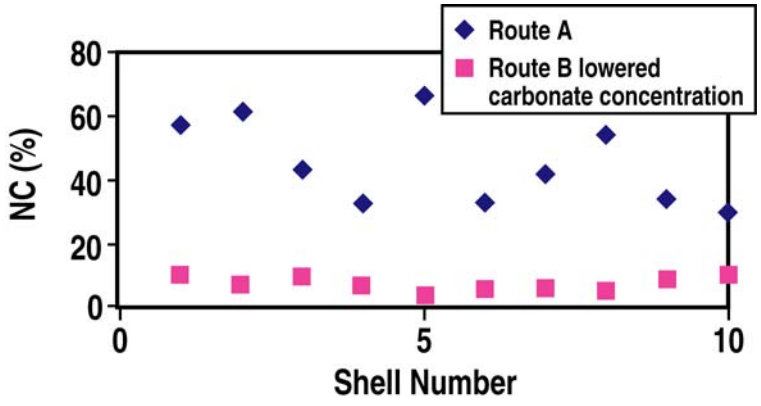

Fig. 3-27. NC data for shells made by route B with controlled gelation times by lowering sodium carbonate concentration.

However, increasing the amount of acid in the system consequently decreased the gelation time. As mentioned previously, this leads to poorer NC for shells. To control the

gelation to a suitable time for shell fabrication, the carbonate concentration was lowered to increase gelation time. Solubility limitations of benzoic acid at room temperature limited how low of a carbonate concentration could be used while still maintaining a theoretical density of 100 mg/cc and using 0.177 g of acid in the system. Lambert has proposed that increased reaction rates are present in a more concentrated solution causing a faster gelation [3-46].

The shells were fabricated and had a high yield: 35% of shells with the desired NC of $\lesssim 5\%$ due to gelation times similar to the standard RF, which allowed the shells to "center."

Due to the slightly smaller pore size of these shells, we found that 3 to 4 μm GDP overcoating yielded gas retentive shells as in the case of "standard" RF. These overcoated shells await cryogenic testing at LLE.

Conclusion for Section 3.7

Large pore RF foam shells were successfully fabricated using two different methods to yield more transparent cryogenic ice layers inside RF shells. The first method, route A, of increasing the molar ratio of resorcinol to formaldehyde created the largest pore foams but had a decrease in expected density and characterization difficulties due to its nontransparency. The second method, route B, of increasing the amount of acid and lowering the carbonate concentration created mid range pore size between route A and the "standard" formulation. Changes to both formulations to obtain gelation times comparable to "standard" RF led to fabrication of high quality NC $\lesssim 5\%$, shells using both techniques. Route A shells were used at LLE in cryogenic experiments that confirmed formation of more transparent ice layer in these larger pore foams. While route B shells have not been tested at LLE, they do offer the advantages of obtaining the expected dry foam density and increased transparency for route optical characterization in the processing stages and gas retention with a thinner overcoating. Pore size characterization was done on samples made using both methods confirming the large pore size and obtaining a quantitative measure of the pore size distribution although in a limited pore size range $\lesssim 100$ nm.

3.8. FABRICATION AND OVERCOATING OF DIVINYLBENZENE FOAM SHELLS USING DUAL INITIATORS

R.R. Paguio, A. Nikroo, M. Takagi,[1] O. Acenas[2]

General Atomics
[1]Lawrence Livermore National Laboratory, Livermore, California
[2]Cal State University San Marcos, California

3.8.1. Introduction

Foam shells are required in new high-gain designs for direct-drive ignition on the National Ignition Facility (NIF) [3-47]. Resorcinol formaldehyde (RF) foam shells using this new high-gain design are currently fabricated for a scaled-down version for shots at OMEGA [3-48]. The diameter of the scaled-down shell must be the standard OMEGA size, which is currently ~800 to 900 μm. Specifications for these wetted cryogenic foam shells were discussed in Section 3.6. Because the foam is porous, the foam shell must be overcoated with a pinhole-free permeation barrier so that the shells can hold the DT or D_2 gas when it is filled and cooled to cryogenic temperatures. RF shells have been made with the desired specifications and were the first foam shells to be cryogenically filled and shot in the U.S. [3-48, 3-49].

A direct extension of the work on RF foam shells for direct drive experiments was fabrication of large pore foam shells in order to increase the cryo-fill fraction when these shells were cryogenically layered with D_2. Optical clarity of the D_2 ice layer was severely reduced when the standard RF foam shells were cryogenically layered [3-50]. It was theorized that because the pore size of standard RF foam is < 100 nm, it can lead to under-filling of the D_2, reducing the clarity of the ice layer. If larger pore foams were used, it could increase the cryo fill fraction, which could lead to a clearer ice layer. Because divinylbenzene (DVB) characteristically has large pores, it becomes a candidate for fabricating large pore foam shells.

DVB shells are opaque because of its large pore size. The opaqueness of the shells precludes visible-light characterization, the current method used to characterize transparent foam and full density shells. Because of this difficulty, different techniques needed to be developed to characterize these shells. DVB shells have also been developed and previously fabricated [3-51]. This traditional way to fabricate DVB foam shells creates shells that crack and implode during the fabrication process; this leads to a low yield of intact shells. We improved the yield of this process using a dual initiator system, which led to more robust shells that can survive the fabrication process.

This paper discusses the changes that have been made to the DVB shell production process, which produces more robust DVB shells that can survive the fabrication process. The issues and results of overcoating the gas permeation barrier on these shells as well as the characterization of these shells will also be discussed.

3.8.2. Fabrication of DVB Foam Shells

The fabrication of DVB shells is a direct extension of the microencapsulation process of full-density poly-α -methylstyrene (PAMS) shells [3-52, 3-53]. The shell diameter and shell wall produced were controlled by producing the shells with a triple orifice droplet generator [3-48, 3-51 to 3-57]. Previous work on investigating the production of DVB shells was done using one thermal free radical initiator such as azobisisobutyronitrile (AIBN) [3-51]. When this process is used to make DVB foam shells by the microencapsulation process, many of the shells crack or implode during the solvent exchange process [Fig. 3-28(a)]. The current production shells that we make such as PAMS or RF do not show this problem.

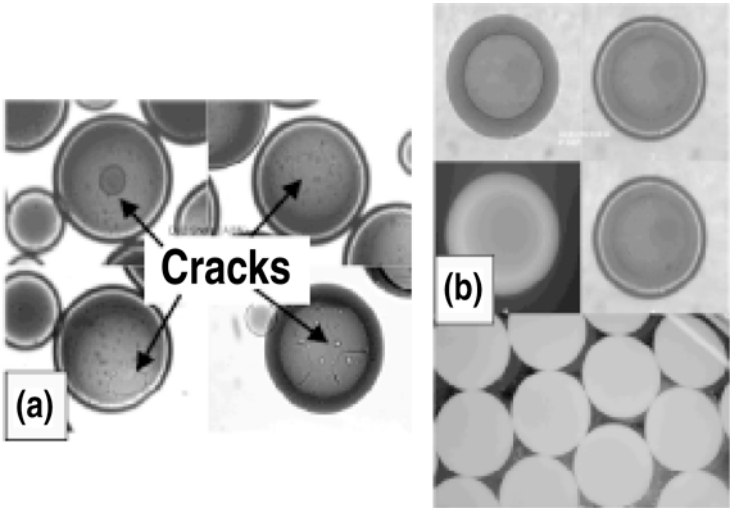

Fig. 3-28. (a) 2 mm DVB shells made with single initiator (shells cracked during solvent exchange). Cracking of shells during the solvent exchanges produces lower yields of intact shells. (b) 3.5 mm DVB shells made with dual initiator (no cracking), leads to a higher yield of shells.

In some polymer systems, a combination of initiators has a synergistic effect on the system, which can affect the physical properties, as well as polymerization time of the polymer. These synergistic effects are only seen when the combination of initiators is used, and not seen when only one of the initiators in the combination is used. Because of this we combined AIBN with another thermal azo type thermal initiator from Wako Chemicals, 2,2'-Azobis4-methoxy-2,4-dimethylvaleronitrile (V-70) in the DVB/DBP solution. When the dual initiator DVB solution was implemented in the fabrication process for DVB shells the shells were able to survive the solvent exchange process into isopropyl alcohol (IPA) to remove the water and DBP in the shell [Fig. 3-28(b)]. This was observed in shells made in the OMEGA (800 to 1000 μm) and NIF (2000 to 3500 μm) size range. The yield of intact shells after IPA exchange was ~95%. The dual-initiator system worked for strengthening the DVB shells to complete the IPA exchanges without cracking or imploding, greatly improving yield as compared to the single-initiator system.

Like any other ICF spherical target, DVB shells must be accurately characterized for wall thickness and uniformity, diameter, and nonconcentricity. As stated previously, the DVB shells are opaque and visible characterization could not be used. Because of this, we developed another way to characterize these shells by using wet characterization. This was done by placing the DVB shells in an index-matching fluid. Benzyl salicylate was used as the fluid to measure DVB shells [3-58]. By placing the DVB shells in a fluid that had the same refractive index as the DVB, the shells would appear transparent, which allowed us to measure the shell wall and its wall uniformity. The results show that a majority of the shells (75%) meet the wall uniformity standard (NC ≤ 5%) and have a nonconcentricity (NC) of < 5% (Fig. 3-29). As an alternative, x-ray radiography may be used in the future to characterize the DVB shells, this will be able to give us the sphericity and wall uniformity of the shell when it is dried.

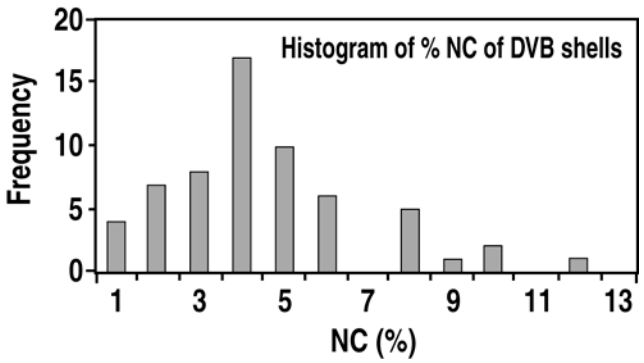

Fig. 3-29. Histogram of the shell wall nonconcentricity of the DVB foam shells. From the plot it shows that a majority (75%) of the shells meet the wall uniformity specifications and have NC values of 5% or less.

3.8.3. Overcoating of DVB Shells

A key requirement for these foam shells was an overcoat of a full-density gas permeation barrier. The process used to close the RF foam pores was to apply a polymer coating through the glow discharge polymer (GDP) process [3-48, 3-59, 3-60]. GDP could not be used as the permeation barrier because it could not close the large pores of the DVB foam at thicknesses of a few μms. Polyvinylphenol (PVP) has been used as an overcoat on other large pore foams in the past and is deposited on the shell by a polycondensation reaction [3-51, 3-59]. One issue in using the PVP is that there is a 20% diameter shrinkage when 5 μm or more is coated on the foam [3-48]. This could lead to densification of the foam shell, which is not desired. When < 3 μm of PVP is coated there is little to minimal shrinkage of the diameter, but it was found that a 3 μm coating could not provide a pinhole free permeation barrier. Therefore, the permeation barrier used was a dual coating of PVP and GDP (Fig. 3-30). The DVB shell was coated with 2 to 3 μm of PVP, which helped fill most of the larger pores with minimal shrinkage; the rest of the pores were filled with a 3 to 4 μm coating of GDP. The shells with

the dual coatings were tested for gas retention using XRF and ~70% of the shells had a pinhole-free permeation barrier and were gas retentive (Fig. 3-31).

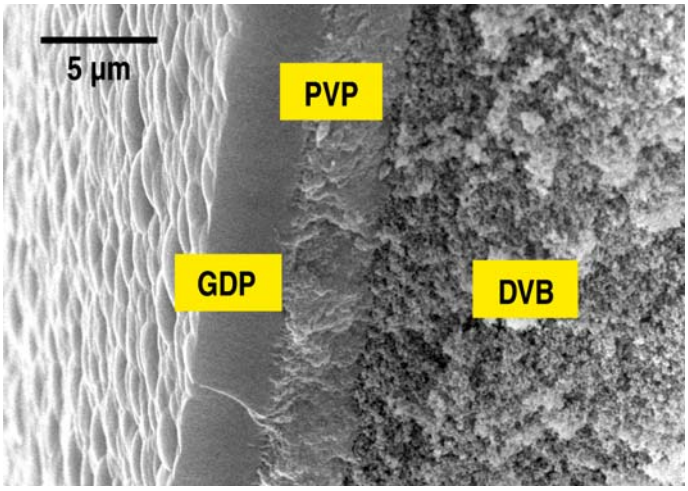

Fig. 3-30. Cross section of a PVP/GDP overcoated DVB shell.

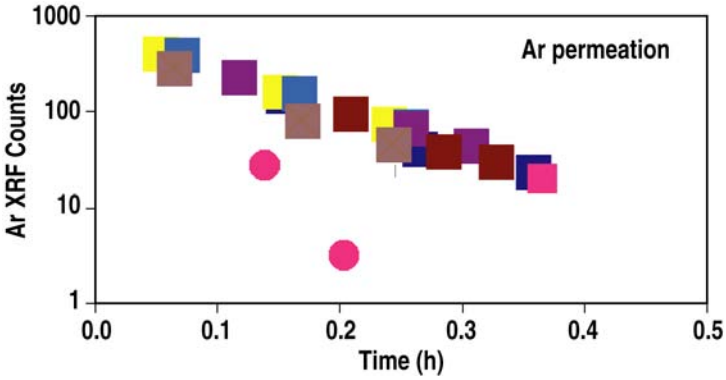

Fig. 3-31. XRF data on gas retention of DVB shells overcoated with PVP/GDP. The shells that hold gas show that the Ar decays gradually (coating pinhole-free), while the rejected shell that does not hold gas decays more rapidly.

These shells were also buckle tested by over-pressurizing the shells in a pressure cell and observing through a viewing window at what pressure they fail. The shells that were tested were shells that held gas with a diameter of 3.5 mm. The shells did not implode catastrophically at 20 psi, at this pressure cracks can be seen. Shells were then tested at 10 psi, at this pressure nothing was observed in the viewing window but when examined under a microscope small micro cracks were seen. Other shells were tested and some of the shells did not appear to crack or buckle through the viewing window at 98 psi. But like the shells at 10 psi when observed under a microscope, micro cracks were observed. Because the shells are opaque, we could not tell if the shells developed micro cracks at that pressure or at a lower pressure. If this is the buckle strength of these shells, it may be a problem when

filling larger diameter shells. If this is the case, future work may include trying to increase the robustness of the DVB shells even further. More buckle strength testing must be done on these shells to understand their strength limits.

Conclusion for Section 3.8

DVB shells were fabricated using this new dual-initiator approach. This new approach made the DVB shells more robust to survive the fabrication and overcoating process, producing a high yield of intact shells (~95%). The resultant DVB shells could be produced with the current spherical and wall uniformity specifications for wetted foam shells on OMEGA. We also successfully overcoated a pinhole-free gas permeation barrier on the DVB shell with PVP /GDP coating. This work was also transferred to the Inertial Fusion Energy (IFE) group, which desires a pure CH foam shell [3-51]. These shells still need further testing to see if the permeation barrier is suitable at cryogenic temperatures to allow D_2 liquefaction and ice layering. Finally, more work must be done on testing and improving the buckle strength of these shells.

3.9. SILICA, METAL OXIDE, AND DOPED AEROGEL DEVELOPMENT FOR TARGET APPLICATIONS

J.F. Hund, R.R. Paguio, C.A. Frederick, A. Nikroo — General Atomics

3.9.1. Introduction

Aerogel and foam targets are utilized in a variety of different experiments such as ICF, plasma radiation [3-61], high energy density physics, and laser plasma interaction experiments. A variety of silica, metal oxide, and metal doped aerogels are currently being developed for use as target materials for these and future applications.

Aerogels are interesting materials because the densities can be modified over a wide range, from low density aerogels (~1 mg/cc) to full density sol-gel materials (~1 g/cc). Typically the average pore size is 100 nm or less for these materials, so that the density is also uniformly distributed at small length scales. Typical aerogel synthesis begins with an alkoxide or inorganic precursor that is made to gel via a catalyst. By controlling solvent and precursor quantities the density can be controlled in many of these systems. The hydrogel can then be supercritically dried to prevent shrinkage and cracking, preserving the low density structure of the resulting aerogel. The ability to make these aerogels into spherical shells with very precise specifications is important for ICF experiments, and has been done for resorcinol formaldehyde (RF) aerogels [3-62]. Our improvements to the RF shells are continuing, and we have been able to modify those techniques recently to produce silica aerogel shells as well.

Metal oxide aerogels can also be employed as target materials. Tantalum oxide (Ta_2O_5) has been used in radiation transport experiments [3-63] and can be an alternative to silica aerogels whenever a higher average atomic number material is needed. Low density tin or tin oxide (SnO_2) is of interest as a high efficiency extreme ultraviolet (EUV) light source, because of its emission at 13.5 nm [3-64].

Aerogels with embedded metal particles have application in high energy density physics and radiation experiments [3-61]. Several methods for producing these composite aerogels are being explored. Each method limits excessive aggregation of the metal so that the end product has a uniform loading of small metal particles.

3.9.2. Silica Aerogels

Silica aerogels are typically prepared from an alkoxide such as Tetraethyl orthosilicate (TEOS). A variety of catalysts can be used [3-65], but our experience has led us to concentrate on ammonium hydroxide or amines. In a typical procedure, a prehydrolyzed TEOS precursor (Silibond 40 HF) in ethanol is catalyzed by ammonium hydroxide. The ratio of TEOS to ethanol in this solution is chosen based upon the target density; for low densities

a higher proportion of ethanol is used. At low densities (< 50 mg/cc) ammonium hydroxide is no longer an efficient catalyst, so an amine catalyst such as diethylene amine is preferred.

Recently, our group has produced 100 mg/cc spherical silica shells and beads with controlled diameters between 500 to 2000 um. The dried spherical shells are transparent (Fig. 3-32). To our knowledge, this is the first time that a triple orifice droplet generator has been successfully used to produce spherical silica aerogel shells. This system creates a double emulsion of an inner oil (O1), silica precursor, and an outer oil (O2). The O1 solution is forced through a needle and is encapsulated by the silica precursor solution that is fed through a slightly larger concentric needle. The outer oil then strips the droplet off the needle and into the collection tube. The shells and fluid are collected in a rotating flask to complete the gelation. Finally, the shells are cured, solvent exchanged with isopropyl alcohol and dried with supercritical carbon dioxide.

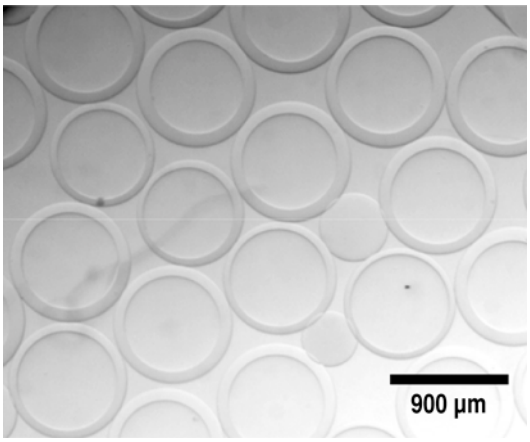

Fig. 3-32. Silica aerogel shells and beads produced by microencapsulation.

This procedure is an alternative to a previous, NH_4OH-vapor-column method described by Kim et al. [3-66] to produce silica aerogel shells. The advantage to using a droplet generator is that good control of shell diameters and walls can be accomplished, so that a large volume of similar shells of a specified size can be made [3-62, 3-67]. It also allows the silica precursor solution a longer gelation time (~15 min), so that the shells can rotate longer allowing better concentricity of shells. During this work, two challenges had to be addressed: control of gelation time and identifying good candidates for O1 and O2 to create the double emulsion. The gelation time is essential to obtaining shells with good inner and outer wall concentricity with our method. If the gelation time is too short, then the inner wall is formed off center and the shell is not radially symmetric. Identifying a good emulsion system for the silica precursor solution was the more difficult problem to solve. The oil used to form the inside of the shell (O1) and the oil used to strip the shell off of the nozzle (O2) had the correct density, interfacial surface tension, and immiscibility with the silica precursor solution.

3.9.3. Metal Oxide and Metal Doped Aerogels

Tantalum oxide aerogels are produced from tantalum ethoxide through acid catalysis with HNO_3 [3-68]. Additional catalysts are being investigated in an effort to further control the density and gelation rate. So far a range of densities from 140 to 500 mg/cc have been made by our group, and both transparent (small pore size) and opaque (large pore size) monoliths have been produced.

Low density tin oxide aerogels have been produced with a process that starts with an inorganic tin precursor, $SnCl_4$ hydrate. The tin precursor is dissolved in an excess of water and ethanol, and over a period of days several exchanges are made with water to remove the excess chloride ion [3-69]. Solvent evaporative drying then removes excess solvent until the solution begins to gel. Then the gel is supercritically dried with CO_2, providing an aerogel with density as low as 250 mg/cc. Silica, tin oxide and tantalum oxide can withstand relatively high temperatures and are good candidates for rapid supercritical extraction [3-70]. This drying process is being explored for these gels and we are currently looking into differences in the two drying techniques.

Further versatility in applications can be achieved by loading aerogels with metal or metal oxide particles [3-71 to 3-73]. Particles can be added to the aerogel matrix prior to the sol-gel transition [3-73]. The primary challenge of this method is the prevention of aggregation of the added particles. If the solution is agitated via sonication, aggregation can be limited so that micrometer sized particles form and stay suspended until gelation of the host aerogel. We have employed this method to produce SnO_2 doped RF aerogels. RF gels of 100 mg/cc were doped with commercially available SnO_2 particles (Nanostructure Amorphous Materials, Inc.) with 60 nm average diameter. The SnO_2 particles were added to water, which was sonicated while cooling, and then the resorcinol, formaldehyde, and carbonate solution were added. Several different concentrations of SnO_2 were added corresponding to 0.1%, 0.5%, and 1.0% of full density (6.95 g/cc) tin oxide. The solution was subsequently rotated in a flask at 60°C for 45 minutes for the base catalysis step. Prior to addition of the benzoic acid solution, another sonication was done to keep the particles from aggregating. After the acid catalysis a postcure was performed at 70°C. Finally the gels were solvent exchanged in isopropyl alcohol and supercritically dried with CO_2.

This tin composite material can be applied just as a SnO_2 aerogel for EUV experiments. Initial laser experiments of this material have produced line narrowing of the plasma emission at 13.5 nm [3-74]. Figure 3-33 shows a backscatter SEM image of the SnO_2 particles in the RF matrix. For comparison, an image from an aerogel with tin oxide particles added with a sonicating probe and without.

Ion implantation allows controlled metal loading of aerogels with a narrow depth distribution below the surface, unlike the metal loading techniques discussed above. The previous techniques can produce a uniform distribution of particles in the aerogel matrix but with little spatial control. With ion implantation, the depth at which the dopant is placed can be controlled through choice of ion energy, and by varying the energy layers or gradients of dopant can be made. Another unique advantage to this method is that the dopant can be implanted in

the aerogel after gelation and drying, so that no post processing is required after the metal is added. Initial work has begun with the implantation of gold in silica aerogels. Gold was chosen as the implant material because of its high atomic number and resistance to oxidation.

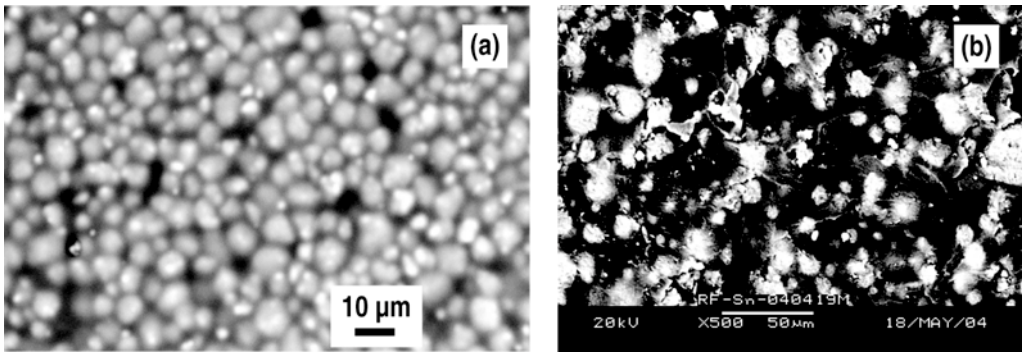

Fig. 3-33. Backscatter SEM image of SnO_2 particles (which appear as bright areas) in an RF gel prepared (a) with sonication and (b) without sonication of precursor solution and SnO_2 particles.

In our initial experiments, gold was implanted in 67 mg/cc silica aerogel cylinders (Fig. 3-34). The silica samples were exposed to 1 MeV Au^- until a total fluence of 8×10^{15} and 4×10^{16} ions/cm^2 was reached. The rate of implant was $4 \times 10^{13} - 5 \times 10^{13}$ ions/cm^2 per minute. From SRIM [3-75], the calculated maximum concentration of such an exposure was estimated to be 1 and 5 at. % Au, respectively. The calculated depth profile is shown in Fig. 3-35. The exposed rectangular area is approximately 9 mm^2 and is visible in Fig. 3-34. X-ray florescence (XRF) spectroscopy confirms the presence of gold in the silica monolith. Qualitatively, a sharp boundary can be seen between implanted and non implanted area gold layer. Small ripples in the aerogel suggest that some minor damage may be occurring to the silica surface above the gold layer due to the high energy of the incoming ions. Full characterization of the gold implant is continuing, and future work will explore other energies and target aerogel densities.

Fig. 3-34. Ion implanted silica aerogel cylinder.

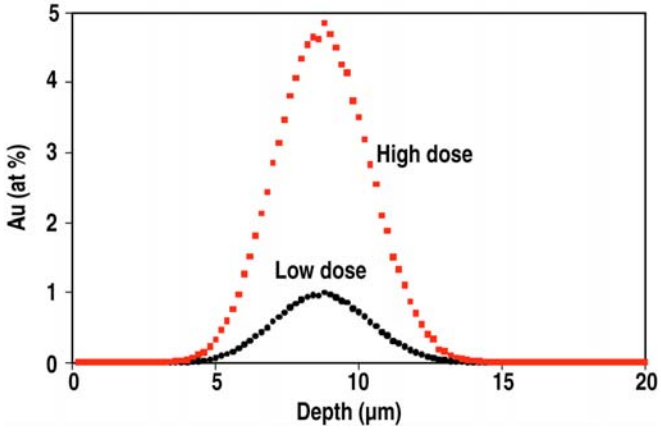

Fig. 3-35. Calculated depth profile (from SRIM [3-75]) of 67 mg/cc silica aerogel exposed to 8×10^{15} (low dose) and 4×10^{16} (high dose) Au^- ions/cm^2. The concentration is given in atomic percent Au.

Conclusion for Section 3.9

Tantalum oxide aerogels are produced from tantalum ethoxide through acid catalysis with HNO_3 [3-68]. Additional catalysts are being investigated in an effort to further control the density and gelation rate. So far a range of densities from 140 to 500 mg/cc have been made by our group, and both transparent (small pore size) and opaque (large pore size) monoliths have been produced.

3.10. COMPLEX PLANAR FOAM TARGETS FOR RAYLEIGH-TAYLOR EXPERIMENTS

R.R. Paguio, C.A. Frederick, A. Nikroo, D.G. Czechowicz, O. Acenas[1]

General Atomics
[1]Cal State University San Marcos, California

3.10.1. Introduction

Perturbations on the surface of direct drive targets can be amplified by Rayleigh-Taylor (RT) instabilities, which can affect or ruin the implosion of the target [3-76 to 3-79]. Experiments have been done to study the evolution of a single mode perturbation from RT instabilities using planar targets with a single sinusoidal wave pattern [3-76 to 3-79]. These experiments can lead to better implosion simulations, which can lead toward a specification on the types of surface perturbations that are tolerable or detrimental to the implosion of these targets [3-76 to 3-80]. Previous experiments used 20 to 90 μm thick full density planar targets made out of polyimide or polystyrene with a sinusoidal wave pattern. Other experiments used 120 μm thick planar foam targets with densities of 100 to 400 mg/cc made out of resorcinol formaldehyde (RF) or divinylbenzene (DVB) with a sinusoidal wave pattern on a 20 to 90 μm full density over-layer [3-79, 3-80]. A similar target with different specifications was requested for these types of RT instability experiments on OMEGA at the Laboratory Laser Energetics (LLE). RF is one of the primary foam systems used for wetted foam direct drive experiments at LLE. In order to study the effects of RT instabilities on this particular foam target, planar RF foam targets with a sinusoidal pattern on a full density over-layer were needed.

The specification for this target is a 200 mg/cc planar RF foam target that is 100 μm thick. The density and target thickness required is to mimic the DT or D_2 ice layer in a cryogenic wetted RF foam target [3-81]. The full density over-layer must have a thickness of 5 μm. This thickness is similar to the full density permeation barrier that is deposited on the wetted RF foam shells [3-81]. The wavelengths of the sinusoidal wave patterns requested on the full density over-layer were λ of 60 to 120 μm, with amplitudes ranging from 0.25 to 1 μm.

These targets are very different than the traditional planar targets that have been used for RT experiments [3-79, 3-80]. Traditional targets had a thicker full density layer that was 20 to 90 μm. The foam density for traditional planar foam targets for RT experiments was approximately 390 mg/cc, which is denser than the targets requested [3-79, 3-80]. This paper discusses the variety of techniques that have been attempted to fabricate these targets for RT instability experiments and how these targets were successfully fabricated through laser machining.

3.10.2. Experimental

Several techniques have previously been attempted to fabricate this target without success. The techniques that were investigated will be discussed here. The first attempt to fabricate these targets used the traditional method in which the full density over-layer was machined with a sinusoidal pattern and glued to the planar foam target [3-80]. The first challenge was to try to diamond machine a sinusoidal pattern placed on a piece of polystyrene (PS) that was 5 μm thick. The traditional targets were also diamond machined, but these targets were a lot thicker.

In the first attempt to machine the PS, we placed a 5 μm thick piece of PS on a flat piece of Copper (Cu). The sinusoidal pattern was then diamond machined on the polystyrene. When this was performed, the PS peeled off, creating a poor sine wave. The second attempt was to use glow discharge polymer (GDP) as the full density over-layer. Unlike the PS, the GDP is overcoated onto the flat copper piece; this allowed the GDP to adhere to the Cu better than the PS. After 5 μm of GDP was overcoated on to Cu, the GDP was then diamond machined with a sinusoidal pattern. The issue with this technique is that the GDP chips during the machining process, which creates a poor sinusoidal pattern in the GDP.

The next attempt to fabricate this target was to diamond machine the sinusoidal pattern on the flat Cu piece. 10 μm of GDP was then overcoated on the machined copper piece, which created a sinusoidal pattern on the Cu/GDP interface. Because the top of the GDP was not smooth from the perturbations on the Cu, the GDP was back machined, which created a flat top surface. The Cu was then removed by immersing the target in a nitric acid solution. Once the Cu was removed, the GDP with the sinusoidal pattern was glued on top of an 100 μm thick 200 mg/cc RF foam. The problem with this method was the micro-gaps in between the Foam/GDP interface, which were not desirable. Another issue with this method was the rippling of the target after the GDP was glued to the foam, causing the target to not be flat.

In order to solve the micro-gap issue, the last procedure was repeated with a slight modification. The modification was to cast a RF mold on top of the back-machined GDP (Fig. 3-36). By implementing this modification, no micro-gaps were observed in the GDP/foam interface. Though the micro-gap issue was solved, the target was still wrinkled, and flatness of the target was still an issue.

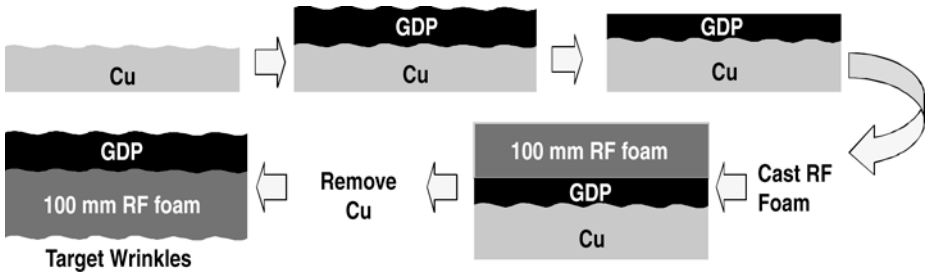

Fig. 3-36. Diagram of the diamond machine and cast method to fabricate targets. This results in a wrinkled target with no micro-gaps.

3.10.3. Laser Machining the Full Density Over-Layer

After several failed attempts to fabricate this target by diamond machining and casting, the target was fabricated by laser machining the sinusoidal pattern on a GDP overcoated RF planar foam target. The target was prepared by casting a 200 mg/cc RF foam that was ~100 μm thick. The foam was then exchanged in isopropanol (IPA) and was cut to a specific dimension of (2 × 2 mm^2). After the foam was exchanged in IPA for several days, the RF foam was dried in a supercritical CO_2 drier. Next the foam was characterized to see if it met the thickness and density specifications of 100 μm (± 10 μm) and a foam density of ~200 mg/cc. If the RF planar target met the specifications, the foam targets were coated with ~5 μm of GDP. The targets were then mounted on a Mylar washer and were sent to Exitech to be laser machined.

The targets were machined by a 248 nm Excimer laser at Exitech Inc. There, GA provided a chrome-on-quartz mask which had the particular wavelength patterns that were to be machined. The laser then hits the mask, which machined a particular sinusoidal pattern on the GDP (Fig. 3-37). Several machining parameters were investigated in order to successfully fabricate the specific sinusoidal wavelengths and amplitudes that were requested. The mask controlled the wavelength produced. The amplitude was controlled by the amount of fluence or laser power that hit the machined target. The amount of shots/unit area determined the shape of the sinusoidal pattern; it took at least 100 shots to make a well-defined sinusoidal pattern. Once the proper parameters were investigated to produce these targets, the targets were laser machined (Fig. 3-38).

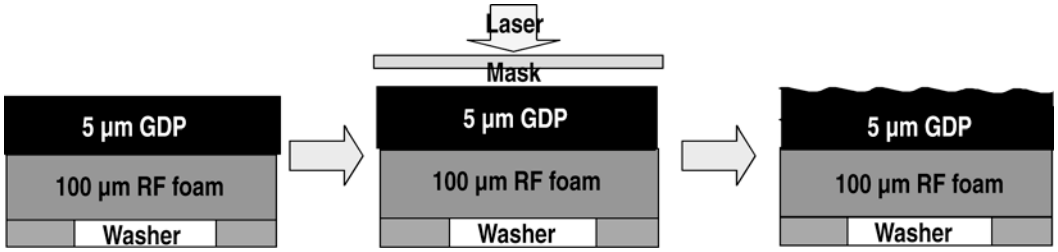

Fig. 3-37. Diagram of the laser machine method to fabricate targets. Results in a planar target with no wrinkling or micro-gaps.

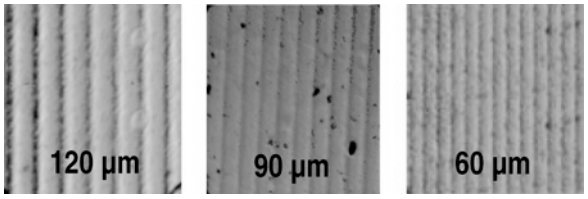

Fig. 3-38. Pictures of planar foam targets with a GDP over-layer that were laser machined. The sinusoidal wave patterns produced were 120 to 60 μm.

3.10.4. Results and Discussion

After the targets were laser machined, they were measured on a Wyko interferometer to see if they met the desired specification. On the Wyko, the targets were measured for the wavelength, amplitude and radius of curvature. The wavelengths that were successfully laser machined on a GDP overcoated RF foam ranged from 60 to 120 μm with amplitudes of 0.5 to 1 μm (Fig. 3-39). A power spectral density analysis (PSD) was also taken on these targets by using the Wyko interferometer. The PSD analyzed the purity of the sine wave. The results from the PSD analysis showed that the sine wave was pure (Fig. 3-40).

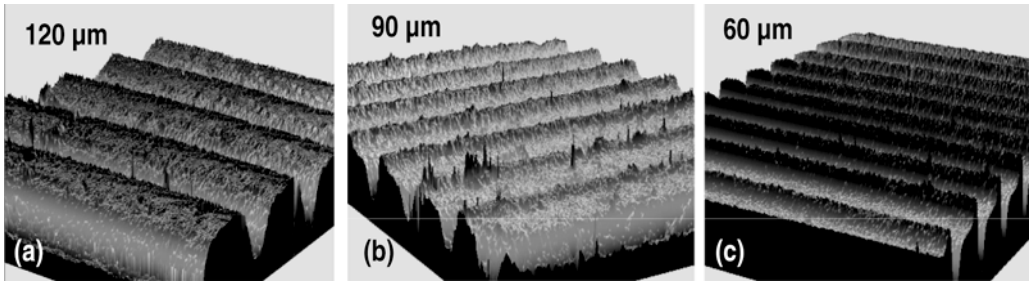

Fig. 3-39. Wyko Interferometer images of laser machined targets.

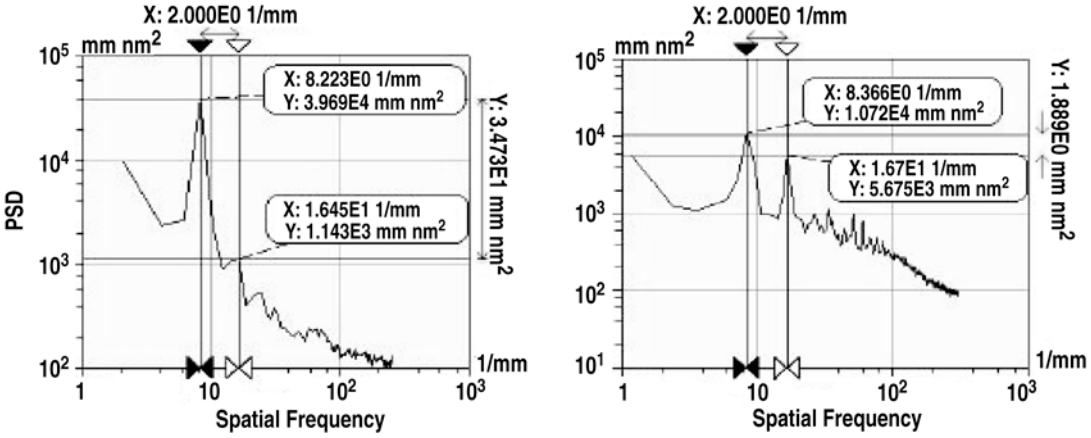

Fig. 3-40. Power spectral density analysis (PSD) of 120 μm laser machined target. (a) Shows a target with a pure sine wave, with no distinct secondary perturbations. (b) Shows a target with a sine wave that is not pure; there are two distinct perturbations instead of one.

From the use of laser machining we were able to produce these targets. Smaller or larger wavelengths can also be fabricated by use of a mask. The limitations occur in fabricating wavelengths with low amplitudes. The amplitude is controlled by the laser fluence. The higher the fluence the more material the laser ablates, which creates a larger amplitude. To fabricate a wavelength with low amplitude, the laser fluence is lowered, but there is a limit to how much you can lower the fluence. At a low enough fluence, no ablation occurs, this is called the ablation threshold. If the fluence of the laser is just above the ablation threshold the amplitude produced is ~0.25 μm. At this point, if the fluence is lowered further, no

ablation will occur. Therefore, the limit to this technique is producing a sine wave with an amplitude lower than 0.25 μm.

Conclusion for Section 3.10

Complex planar RF foam targets with a sinusoidal pattern in a full density over-layer were successfully developed and fabricated for Rayleigh-Taylor experiments at LLE. The wavelengths that were successfully laser machined on the full density range from 120 to 60 μm, with amplitudes of 0.5 to 1 μm. The targets successfully met all specifications and were sent and shot at LLE. We are still awaiting the results of these experiments.

BERYLLIUM TARGET DEVELOPMENT

3.11. BERYLLIUM COATINGS ON SPHERICAL SURFACE FOR NIF TARGET DEVELOPMENT

H. Xu, A. Nikroo and J. Wall — General Atomics

3.11.1. Introduction

Beryllium is one of the preferred ablators for achieving ignition on the National Ignition Facility (NIF) [3-82]. Sputter coating of beryllium on plastic mandrels is one possible means of producing beryllium shells for NIF and has been investigated for some time [3-83 to 3-86]. It is potentially the only technique that would allow a graded copper doped ablator as is currently proposed for NIF due to its superior stability during implosion. However, due to the directional nature of the sputter coating process and low temperature limitation of plastic mandrels, such coatings can suffer from low density and high defect density. The coating surface roughness also generally increases with film thickness. A better understanding of coated Be film density, the development of void defects in the film and how they are affected by surface roughness will help to develop strategies for improving film qualities. Although a number of modifications to the baseline coating process have been investigated to improve the coating quality in the past, such as addition of a bias to the substrates or incorporating impurities, etc., there is still a gap in meeting NIF specifications. In this effort, we have investigated several issues related to the coatings and the parameters used in order to obtain a better understanding of the process. These include the evolution of surface roughness with coating thickness to determine the effects of self shadowing due to the spherical nature of the substrates, the effect of coating rate on micro-structure of the coatings, as well as examining possible effects due to doping of the coatings with copper. This work has been performed in a beryllium coater established in the dedicated beryllium certified enclosure at UCSD's energy research center, which has extensive ventilation to prevent the potential respiratory diseases associated with Be particles. In this preliminary work, only coating thicknesses of approximately ≤ 50 μm were examined for the most part.

3.11.2. Results

We initially prepared numerous 50 μm Be coatings on CH mandrels at 100 W of power to the three Be sources to examine the reproducibility of the process. Fracture cross sections of coatings were examined in the SEM to examine the microstructure. It is seen from Fig. 3-41(a) that the fracture cross section of a ~50 μm coating on a capsule indicates columnar texture of the Be capsule throughout coating. This type of structure was consistently seen when growing at the coating rate of ~ 0.5 μm/h typical of deposition at 100 W for the 3 guns. For comparison purposes, a SEM cross section of Be coating on a flat surface is shown in Fig. 3-41(b). Similar columnar texture is also observed. This suggests that columnar texture is a common structure of magnetron sputtering independent of the

substrate shape. Measurements of the temperature of the bounce pan indicate a temperature of ~ 130ºC to 150ºC during Be coating. This corresponds to a temperature that is ~0.25 of the melting temperature of the beryllium metal agreeing with the expected structure from the zone T growth from Thornton's structure zone model (SZM) [3-87]. Cu doped films have been made with doping levels of ~ 0.5 to 3 at. %. Cu doping does not appear to affect the evolution of the film microstructure. Coatings at higher powers lead to a transition to an undesirable low density twisted structure. This structure can be avoided while coating at a higher rate by cycling the power to sputter sources (cycling coating rate).

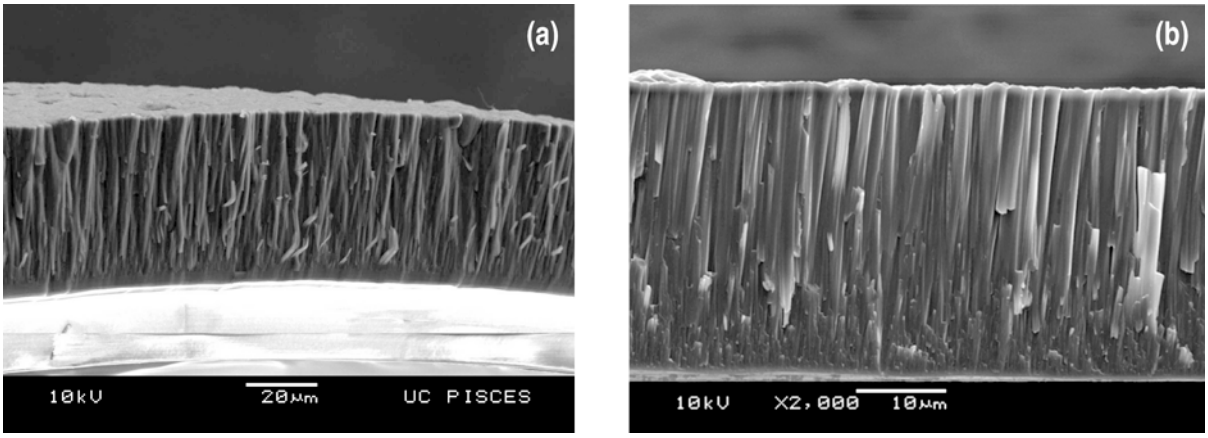

Fig. 3-41. (a) A cross-section SEM image of a ~50 μm Be shell showing consistent columnar structure. (b) A cross-section SEM picture of a Be coating on a flat Si substrate, which also shows columnar grain growth.

The surface roughness information is useful in identifying the film surface roughening mechanism. Normally as coating thickness increases, the film surface becomes rougher. The surface roughness RMS versus film thickness follows a power law, $R \sim d^{\beta}$, R is surface roughness RMS, d is film thickness and β is a power component [3-88]. Roughness in the surface is related to rough internal interfaces and may introduce more defects in the film. In order to understand coating-surface roughening mechanisms, we investigated the film roughness versus film thickness by AFM. Figure 3-42 shows an AFM power spectrum of a typical capsule surface. The high mode surface roughness indicates that the surface is fairly rough. Surface roughness RMS (101 to 1000) is 282 nm for a ~ 50 μm coating. Figure 3-43 shows plots of film surface roughness with high mode RMS versus film thickness for two groups of samples. The first group of samples prepared at 10 mTorr, with 3 to 6 shells in each batch and bounced at 120 Hz ~0.9V, showed a power exponent of $\beta \sim 0.78$. The other group of samples were prepared at 10 mTorr with 12 to 15 shells in each batch and bounced at ~110 Hz and up to 1.9V. The power component for this group of samples is 1.19. These roughness power components are higher than those normally observed on flat surfaces, which are typically < 0.5 to 0.6 [3-88].

According to the ballistic deposition model, the exponent will have a value of one-third at small angles of incidence (near normal) and increases with incident angle to approach one-half for large angles [3-89]. Considering the shadowing effect, which describes high spots

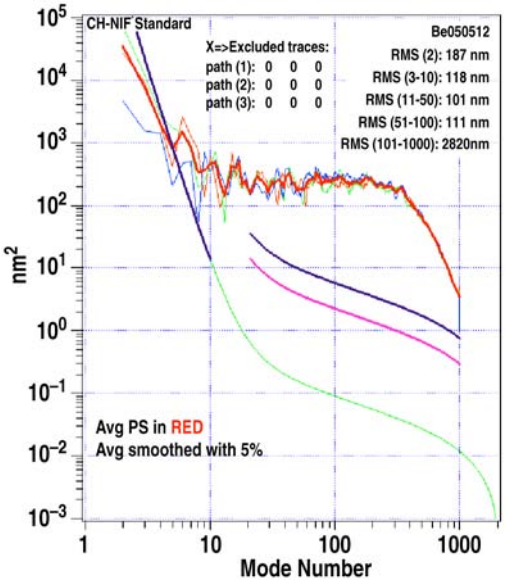

Fig. 3-42. A typical AFM spheremapping power spectrum of a ~50 μm Be coating on a 2 mm CH mandrel.

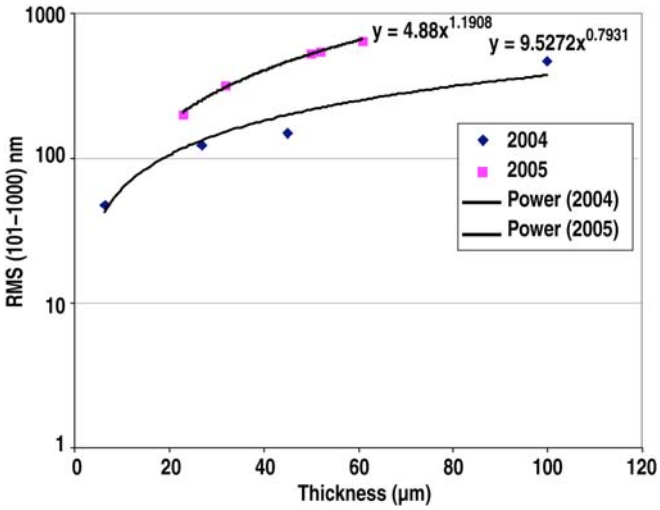

Fig. 3-43. A plot of high mode surface roughness RMS versus film thickness. Two groups of samples give RMS component from 0.78 to 1.19.

shadow low spots on a surface and is more pronounced at off-normal incidence, value increased to ~ 0.7 to 1.0 depending on incident flux angle distribution [3-90]. The value of RMS roughness component of our coatings on spherical surface is inconsistent with shadowing dominated mechanism. Since our coating is on spherical mandrels, an incident flux is at an angle to a surface normal, which changes from the middle of the mandrel surface to the edge. The large angles near the edge of the mandrel surface lead to stronger shadowing effect and fast roughening behavior. This could be the reason for our observation of faster growth of the RMS power exponents. Micro-particles, generated during coating by either shell agitation or sputter source debris incorporation, were also found to contribute to fast film roughening.

One of the important parameters for NIF targets is the sputtered Be film density. Two different ways to measure the Be film density were used. By weighing the shell and getting the diameter and thickness from x-ray radiograph, Be coating density is calculated by $\rho = W/V$, where W is the weight of the Be coating and V is the volume of the Be coating. The second method to determine the density is to use buoyant force measurement of mandrel removed shards. The measurements from two methods give similar results. Table 3-2 showed a few measurements of Be coating density by two methods. Since Be bulk density is 1.847 g/cc, our measurements of the density by the first method suggest that Be coating is ~95% to 96% of the bulk density after deposition. Although the measurements have an accuracy of $\pm$ 3%, it is still encouraging that sputtered Be film showed near full density. The second method gives a slightly higher density, which can be explained by some surface oxidation during annealing. These data suggest that the coated Be film density is fairly high. However, the measurements here are limited to coatings of ≤ 50 μm thickness.

Table 3-2
Density Measurements of Be Coatings

ρ = m/V Measurements		Buoyant Force Measurements	
Be Shells	Density (g/cc)(± 32%)	Be Shells	Density (g/cc) ± 0.01 g/cc
Be050325, 49 μm	1.8082	Be050325, 49 μm	1.84
Be050408, 53 μm	1.7981	Be050408, 53 μm	1.84
Be050414, 43 μm	1.7880	Be050215, 23 μm	1.85
Be050420, 53 μm	1.7981		

Conclusion for Section 3.11

Be coatings on CH mandrels have been prepared and initial characterization indicates the films with thickness < 50 μm can be produced at ~ 0.5 μm/h with consistent columnar structure that have densities within several percent of bulk Be density. The surface roughness of the coatings has been studied to identify the roughening mechanism. The roughness RMS growth exponent of 0.8 to 1.2 of the films suggests the dominant roughening mechanism is self-shadowing. Coatings at higher powers lead to a transition to an undesirable low density twisted structure. This structure can be avoided while coating at a higher rate by cycling coating rate. Micro-particle, generated during coating by either shell agitation or sputter source debris incorporation was also found to contribute to fast film roughening. Cu doped films have been made with doping levels of ~ 0.5 to 3 at. %. Cu doping does not appear to affect the columnar grain growth of the film. Biased diffusion, ion etching and ion assisted deposition are believed to be effective in improving film density by suppressing the self-shadowing effect and improving film surface/interface smoothness.

3.12. USING FOCUSED ION BEAM TECHNOLOGY TO DRILL HOLES IN AND ATTACH FILL-TUBES TO A BERYLLIUM ABLATOR

H.L. Wilkens, A.V. Hamza,[1] A. Nikroo, and N.E. Teslich[1]

General Atomics
[1]Lawrence Livermore National Laboratory, Livermore, California

3.12.1. Introduction

Successful simulated performance of a Cu-doped Be ignition target makes it the current material of choice for the ablator in a National Ignition Facility (NIF) scale capsule [3-91]. Work is underway to find the best way to fill a Be capsule, which will be upwards to 170 μm thick. In the current design [3-92] the through-hole is 5 μm in diameter on the surface of the shell, with a 12 μm diameter counter-bore hole centered over the through-hole. A glass fill-tube needs to be placed inside the counter-bore hole and somehow sealed to the shell. Collaborative work between General Atomics and Lawrence Livermore National Laboratory (LLNL) is underway to examine using focused ion beam (FIB) technology in many fabrication aspects of this fill-tube design, including drilling the through- and counter-bore holes as well as manipulating and attaching the fill-tubes.

3.12.2. Experimental Technique

In general, FIB systems use a finely focused beam of ions that are used at low beam currents for imaging or high beam currents for site specific sputtering or milling [3-93]. By using a series of electrostatic lenses and apertures to control the size and current density of the ion beam, and a system of scan generators and coils to control the beam location, material can be selectively removed from areas of sub-micron dimension. When impinging on the sample surface, the ions create a cascade of events which result in the ejection of a sputtered particle; an appreciable fraction of the ejected material is typically re-deposited on the side-walls, so it can be difficult to control the amount of material removed by sputtering, especially in some geometries. It is this material re-deposition which ultimately limits the aspect ratio of a sputtered hole. Another result of the sputtering process is that implantation of the ions on the order of several hundred nanometers is to be expected [3-94, 3-95].

The FEI Nova600 FIB system at LLNL consists of a dual (gallium) ion/electron beam system, which allows the imaging capability of an integrated scanning electron microscope (SEM) in addition to images created from collecting secondary electrons created in the sputter process. The system is also outfitted to make in situ x-ray ultramicroscopy (XuM) images.

3.12.3. Experimental Results

The initial study involved using the FIB to drill through-holes in a shell with a 47 μm Be wall thickness. Starting with 40 μm diameter hole, holes of progressively smaller diameters were then created with the FIB, down to a 15 μm diameter hole. Two of these holes are shown in the low magnification SEM image in Fig. 3-44. The holes were clean on the sidewalls, though XuM images show that the holes of smaller diameter tapered at the bottom, likely due to redeposition of the sputtered material. Drilling of smaller holes is theoretically possible, but aspect ratio limitations will make drilling a 5 μm diameter hole through a NIF-scale ablator impossible using only the ion beam. An additional drawback of the technique is the length of time required to drill the holes: several hours with a FIB as compared to just minutes with a laser. The possibility of using chemically assisted FIB machining is being pursued which may help to overcome the aspect ratio limitations, as well as to enable faster drilling by increasing the sputter yield [3-96 to 3-98].

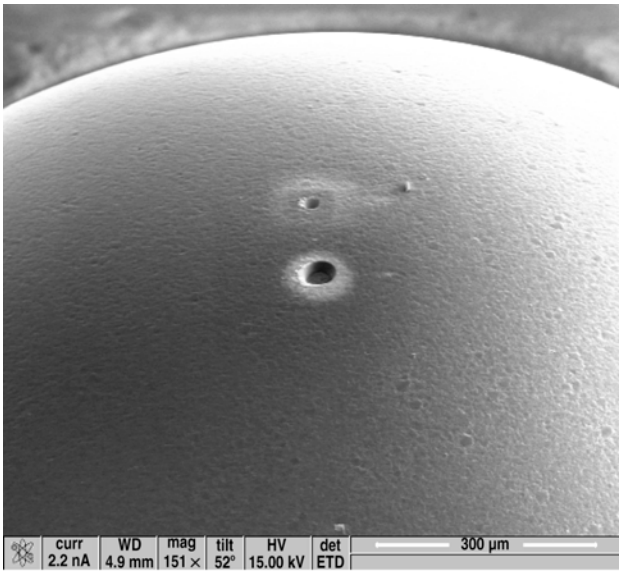

Fig. 3-44. Low magnification in situ SEM image of 20 and 40 μm diameter holes made in the FIB system.

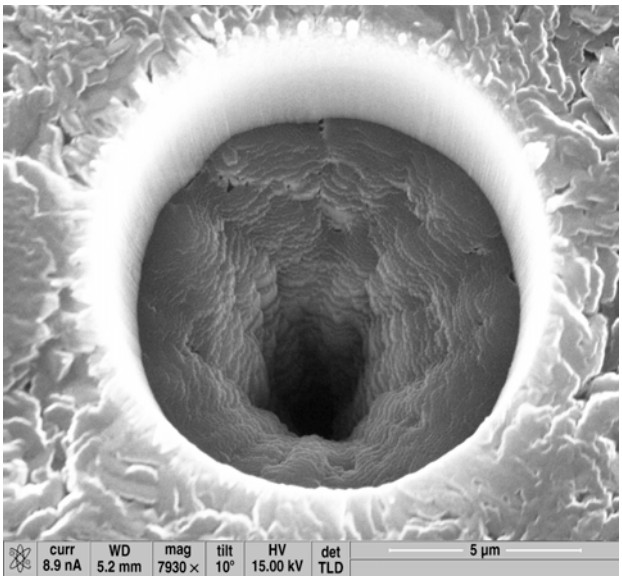

Fig. 3-45. This SEM image shows a 12 μm diameter, 10 μm deep counter-bore created over an existing 5 μm hole in a Be shell.

The next experiment conducted was to use the FIB to create a counter-bore on top of a pre-existing hole. This experiment met with quite good success since the in situ SEM in the FIB system allows the operator to quite easily center the counter-bore over the hole with an accuracy of much less than a micron. This success was welcomed in the target fabrication community due to the fact that previous work by other groups using electrical discharge machining (EDM) did not have good results: in most cases the EDM made counter-bore missed centering over the pre-existing hole by many tens of microns. Figure 3-45 is an SEM image of a counter-bore made over a FIB-drilled 5 μm diameter, 10 μm deep hole that was made in the shell for this proof-of-principle

experiment. The image shows how well the counter-bore is aligned on top of the hole, and confirms that the opening to the FIB-drilled hole remains open after drilling the counter-bore. The process time to create this counter-bore was less than 30 minutes.

With the Omniprobe®, an in situ microprobe in the FIB system at LLNL which has a range of ~5 mm in each direction, we have shown that we can pick up a fill-tube lying next to the shell and align and place the fill-tube with the counter-bore. It is this series of tasks which we attempted to complete with both a nominally 55 μm thick Be wire and a tapered glass fill-tube with an outer diameter of ~10 μm at its tip. Work started with the Be wire since a glass fill-tube was not then available, figuring that if the work could be done with the Be wire, being approximately five times larger than a glass fill-tube, it would be safe to assume that the same work can be done with the smaller and more manageable glass fill-tube. In both cases, ion beam assisted chemical vapor deposition was used to weld the tip of the in situ probe with platinum to the surface, as shown in Fig. 3-46(a) on a glass fill-tube. In the case of the Be wire we took the next step and moved it into place over the counter-bore as can be seen in Fig. 3-46(b), and placed it into the counter-bore, after which time the platinum weld was removed leaving the Be wire seated in the hole, as shown in Fig. 3-46(c).

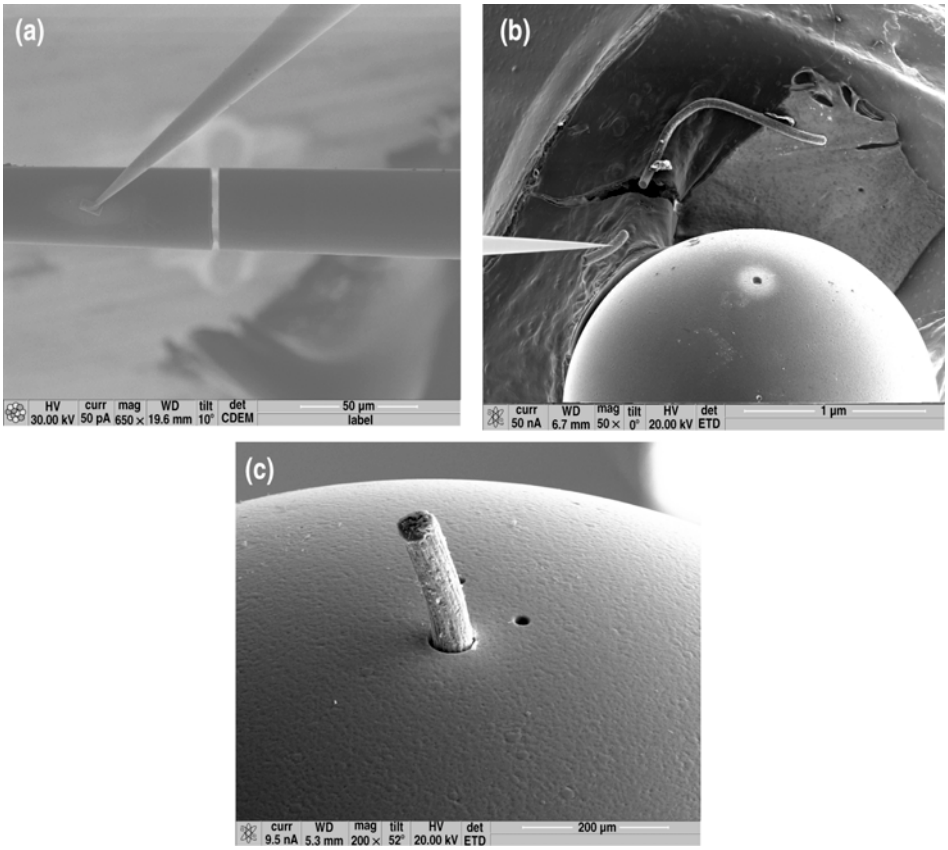

Fig. 3-46. (a) A glass fill-tube is shown attached via a platinum weld to the tip of the in situ Omniprobe®; the cut in the tube was done with the FIB and took approximately 15 minutes. (b) A 55 μm thick Be wire being manipulated with the Omniprobe® inside the FIB chamber. The remaining Be wire from which this piece was cut can be seen in the image above the shell. (c) A 55 μm thick Be wire shown placed in a counter-bore after the platinum weld between the wire and the Omniprobe® has been removed.

Conclusion and Future Work

The FEI Nova600 FIB system at LLNL has been used to show the promise of using FIB technology to drill holes, create counter-bores, and place fill-tubes into a Be ablator. Working from these results, plans are being made to continue this collaborative effort with LLNL by investigating the use of a chemically assisted etch to enhance the physical sputter rate of the FIB to create a 12 to 15 μm diameter counter-bore and a subsequent 5 μm diameter hole through a Be ablator of NIF scale. Experiments will soon commence on the first and most necessary step required for success, which is defining a chemical which is reactive with Be.

MACHINING AND PLATING DEVELOPMENT

3.13. MICROMACHINING OF FAST IGNITION TARGETS

M.P. Mauldin, A.L. Greenwood, M.N. Kittelson, C.H. Shearer, J.N. Smith, Jr., and D.M. Woodhouse — General Atomics

3.13.1. Introduction

The concept of fast ignition involves the compression of fuel within a shell accompanied by a laser pulse that acts as an ignitor in the reaction. The fast ignition targets described here are composed of a hollow shell that sits on a gold cone penetrating to the center of the shell. Lasers are used to first compress the fuel filled shell on to the tip of the cone. A Petawatt laser pulse is then shot through the hollow cone to the location of the compressed fuel to start the reaction. Typical targets made recently by GA contain a shell of diameter less than 1 mm and total cone length of 5 mm. Other given specifications include gold thickness and location of the shell center in relation to the gold cone tip. The shell center must be within 5 μm of the cone tip in the radial direction and within 10 μm of a given specification in the axial direction. A cross-section view of the design of a fast ignition target is shown in Fig. 3-47 with an example of given specifications. These targets have been produced for several years at General Atomics as described by Hill et al. [3-99]. More recently our process for creating them has been improved for efficiency and consistency and this paper will focus on the machining aspects in this effort.

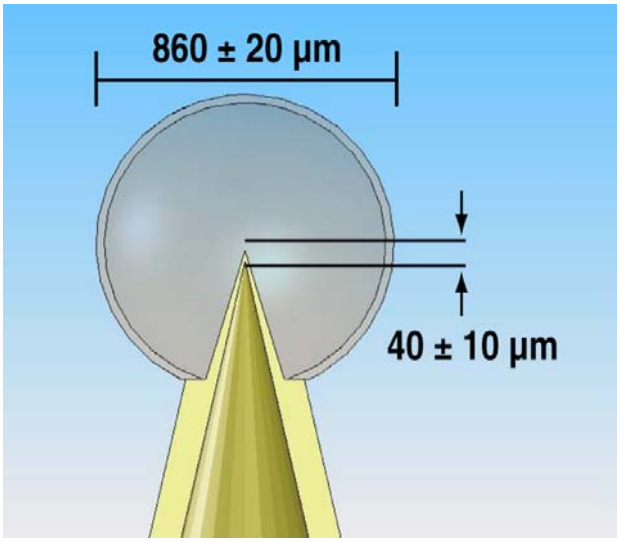

Fig. 3-47. A cross-section view of a computer model of a shell-cone fast ignition target.

3.13.2. Machining of Cone and Shell

The first step in creating these targets is making a mandrel and electroplating it with gold. Copper is used as a mandrel material because it is easy to work with and etch away in later stages of assembly. The shape of the mandrel will determine the inner profile of the cone portion of the target. A cylinder is first machined from stock copper rods on a CNC lathe. Next, the copper part is placed in a precision diamond turning lathe and a series of machining programs and tools are used to create a cone of the proper form. After the copper cone has been made it is plated with gold approximately 120 μm thick. This amount of gold is necessary to accommodate for the back machining of the cone that will take place in a later stage.

A hollow glow discharge polymer (GDP) shell is used for fast ignition targets and is produced by the PAMS-GDP method as explained by Nikroo et al. [3-100]. The shell is glued onto a glass slide that allows it to be placed on the vacuum chuck of the diamond turning lathe. From the known values of the shell diameter, shell wall thickness, and desired final target dimensions, the amount of shell material to be removed from the crown of the shell is calculated to provide the correct size hole. The shell is placed in the diamond turning lathe and repetitive cuts across the front of the shell are made to the calculated depth. The shell is next released from the glue on the slide and examined under a microscope to check the quality of the cut hole. Figure 3-48 is a picture of a shell with a hole machined in it. Measurements are taken again of the shell's outer diameter and wall thickness along with the diameter of the hole and how well it is centered on the shell.

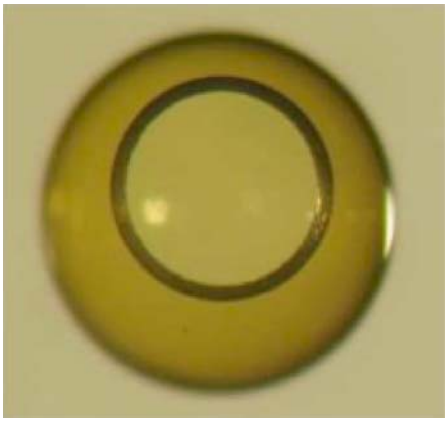

Fig. 3-48. A hollow GDP shell with a machined hole to be placed on top of a fast ignition target.

3.13.3. Back Machining Gold Cone

The final machining process for the fabrication of these targets is machining the gold surface of the plated copper mandrel. A shelf is cut into the gold surface toward the tip of the cone on which the GDP shell will sit. When making these targets in the past, the shells and cones were machined independently of each other. Pairs of cones and shells were then chosen that fit together well enough to meet specifications. We have modified this step in the fabrication process by machining the gold tip of each cone to match a specific shell that has already been cut. The final target shell must sit at a height so its center is a specific distance from the gold cone tip. This vertical offset dimension is the factor used to determine exactly how the cone tip is to be machined. By using the measurements of the shell diameter, shell wall thickness, and final desired dimensions of the target, the location of the shelf to be cut into the cone is calculated. Making each cone tip specific to a shell greatly reduces the error in the vertical distance from the cone tip to shell center. The gold plated copper mandrel is put in the diamond turning lathe and a 5 μm radius tool is used to form the desired shape.

The process of gluing and releasing the shell from the glass slide sometimes slightly affects its dimensions. This is why shell measurements taken after it has been cut are used to calculate the necessary profile of the gold cone tip. This calculation gives the necessary cone tip to shelf distance and indicates how the base of the cone (at the shelf) and inner diameter of the shell hole will fit together. There are three possible conditions for this fit. The cone tip angle may accommodate a shell so that it can sit on the shelf with no clearance between the cone base and inside radius of the shell hole. This means that when the shell is placed onto the cone, it fits perfectly with no room for shell movement on the shelf. A second possible condition occurs when the size of the shell hole is larger than the cone base diameter. This case results in clearance between the cone base and inside radius of the shell cone. An illustration of this condition is shown in the left side of Fig. 3-49. When positioned on the cone, this type of shell has the ability to move around on the shelf. The third possible situation occurs when the shell hole is too small to accommodate the base of the cone. In this case, there is interference between the inside radius of the hole and the base of the cone. An extra step in machining is necessary when this condition occurs. The base of the cone is machined with a flat side in the axial direction of the cone, perpendicular to the shelf. This decreases the circumference where the shelf meets the cone tip allowing the shell to fit. The picture on the right side of Fig. 3-49 displays a drawing of a target that has been modified in this manner. Without this modification the shell would not rest on the shelf but on the sides of the cone and its position would result in an error in the vertical offset.

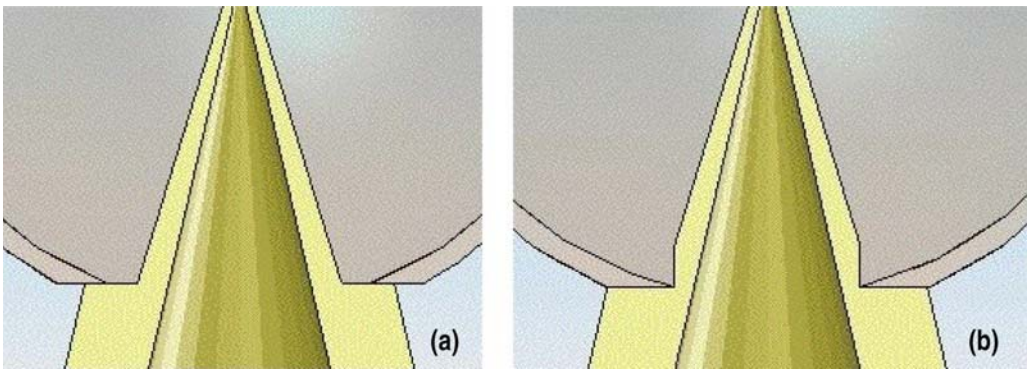

Fig. 3-49. Examples of two possible conditions encountered when mating cone-shell pairs. On the left there is extra space between the diameter of the shell hole and cone base. On the right, the cone base had to be modified to account for interference between the two.

3.13.4. Assembly of the Target

The fast ignition target is ready to be assembled after matching pairs of cones and shells have been created. The copper mandrel is first removed by placing the cone in a nitric acid solution. The GDP shell is placed onto the cone tip so that the machined surface of the shell sits on the gold shelf. The shell must be centered so the shell center is within 5 μm of the cone tip in the radial direction. After the shell is in the correct position, a bead of glue is applied around the joint of the shell and the assembly process is complete. After assembly,

the target is examined under microscope and characterized to be sure that all the required specifications have been fulfilled. A picture of a completed fast ignition target with a 26 deg cone angle is show in Fig. 3-50.

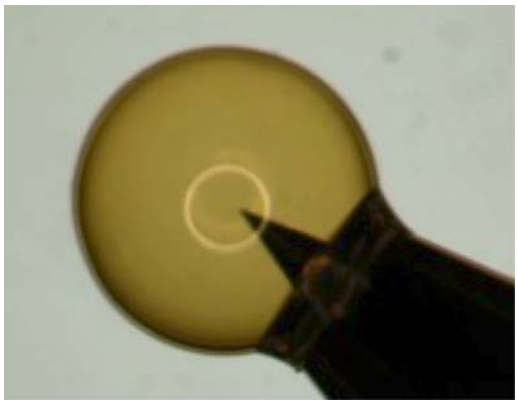

Fig. 3-50. A cone-shell fast ignition target with a cone angle of 26 deg.

Conclusion for Section 3.13

At General Atomics we have been able to consistently produce fast ignition targets that are within required specifications. Fabricated targets have had gold cones ranging from angles of 24 to 70 deg with wall thicknesses ranging from 10 to 30 μm. The GDP shells used in these complex targets have been smaller than a millimeter in diameter and accurately assembled with the finished gold cones we have machined. Modifying the process of machining the target cones has resulted in more repeatable and efficient fabrication. By forming each individual cone to fit a specific shell, instead of simply matching pairs together that complement each other to an acceptable degree, no extra cones are necessary and we produce a final product that matches the desired dimensions within given tolerances.

OTHER TARGET DEVELOPMENT

3.14. THE EFFECT OF CORNERS ON ELECTROPLATING OF HOHLRAUM MANDRELS

J.L. Kaae and D.M. Woodhouse — General Atomics

3.14.1. Introduction

Hohlraums as well as other ICF target components are made by gold electroforming, a process where the substrate of a gold electroplated component is dissolved or leached away leaving the gold coating free standing. This process is shown schematically in the case of a hohlraum in Fig. 3-51.

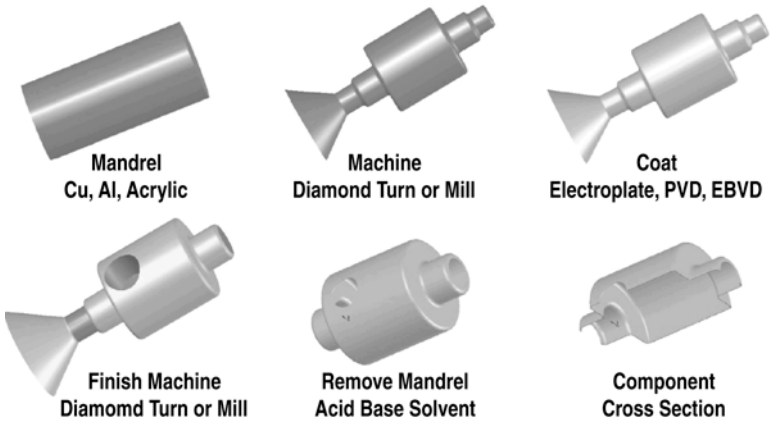

Fig. 3-51. A schematic representation of the electroforming process used to fabricate a hohlraum.

The overall average deposition rate of material on the cathode surface during electroplating is given by:

$$dw/dt = mJ/vF \quad . \tag{3-13}$$

Where

- dw/dt = deposition rate
- m = molecular weight of deposition element
- v = valence of depositing element
- F = Faraday's constant
- J = current density

Migration along electric field lines is not the only way that ions arrive at the region near the cathode surface. Concentration difference driven diffusion and convection driven

migration are also important driving forces for migration. It is well known that the rate of electroplating at corners can differ from that on the body of a component [3-101]. This can be explained by the fact that the electric field is increased at convex corners over that on parallel sections, and the electric field is decreased at concave corners over that on parallel sections. Thus, the electric field driven component of deposition can be affected by corners, but the other components are not necessarily altered by corners.

Since there are corners on hohlraum mandrels (as well as the mandrels for many other target components made by electroforming), the question is what happens to the plating at corners. We consider both convex and concave corners, which are shown schematically in Fig. 3-52. Because of the factors other than the electric field that influence electroplating, the behavior at corners needs to be determined empirically. Such a study is reported in this paper.

3.14.2. Experimental Approach

Standard copper specimens of two different diameters, 6 mm and 3 mm, were used in this study. A scanning electron microscope photograph of one of these specimens is shown in Fig. 3-53. The radii of the corners were varied to determine the effect of the radii of curvature on plating. Also, plating times were varied to examine deposits of differing thicknesses.

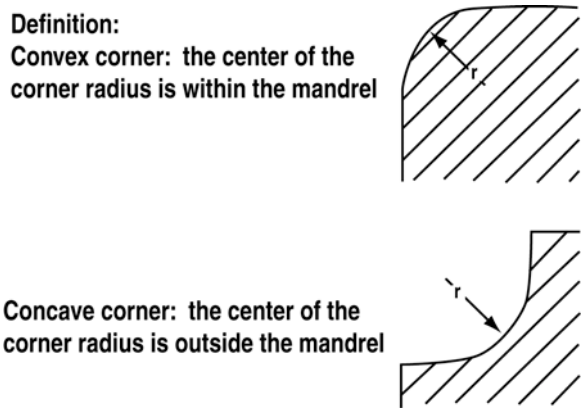

Fig. 3-52. The two types of corners that are present in hohlraums and other types of target components.

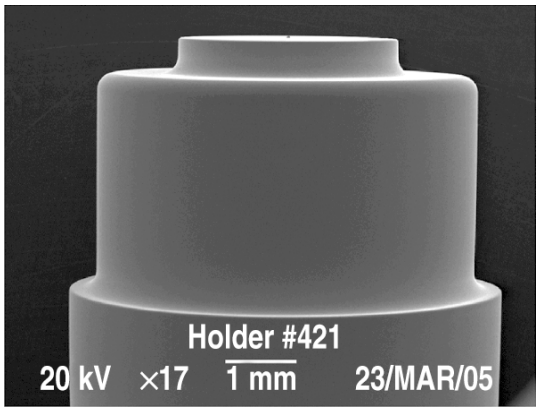

Fig. 3-53. A scanning electron photograph of one of the specimens used in this study.

The specimens were plated in the standard setup used at General Atomics for hohlraum production. A photograph of this setup is shown in Fig. 3-54(a), and the device is shown schematically in Fig. 3-54(b). Note that the anode is relatively distant from the specimens. The electrolyte employed was auro sulfite; the temperature was 40°C; the electrolyte was stirred vigorously; and, various current densities in the range 4.3 to 7.4 ma/cm^2 were investigated. With this system the gold is derived from the electrolyte and not from the anode.

After plating the specimens were sectioned, and the plating distribution was examined in a scanning electron microscope.

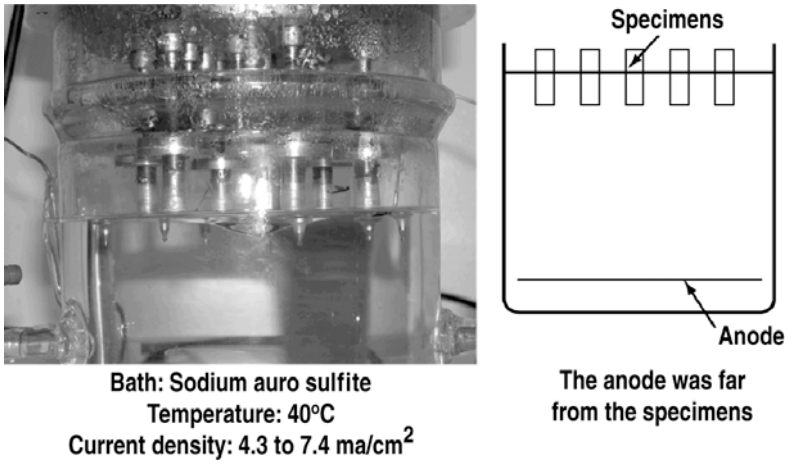

Fig. 3-54. The electroplating setup used at GA for electroplating electroformed hohlraums and other similar target components. (a) A photograph of the setup. (b) A schematic drawing of the setup.

3.14.3. Results and Discussion

3.14.3.1. Convex Corners. The plating distribution on a 6 mm diameter specimen with a 0.2 mm convex corner radius plated at a low current density is shown in Fig. 3-55. The coating is uniform throughout the corner.

At the other extreme consider the plating distribution on a 6 mm diameter specimen with a sharp convex corner coated at a high current density shown in Fig. 3-56. The coating thickness also is uniform at the corner. This uniformity leads to rounding of the corner in this case.

The same effects were observed in 3 mm diameter specimens.

Thus, for the conditions used to electroplate hohlraums, convex corners are always plated uniformly, and the plating uniformity leads to rounding of sharp corners.

3.14.3.2. Concave Corners. The plating distribution on a 6 mm diameter specimen with a 0.2 mm concave corner radius plated at a low current density is shown in Fig. 3-57. The coating is uniform throughout the corner.

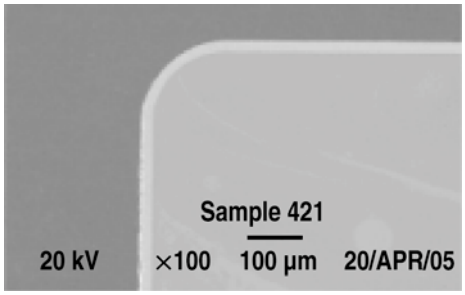

Fig. 3-55. The gold electroplated coating on a 6 mm diameter specimen with a 0.2 mm convex corner radius. The coating is 25 μm thick and was deposited at 4.3 ma/cm^2. The coating is uniform throughout the corner.

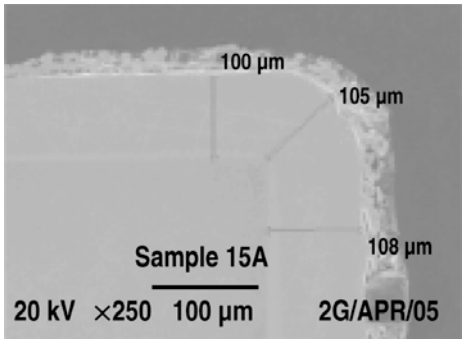

Fig. 3-56. The gold electroplated coating on a 6 mm diameter specimen with a sharp convex corner radius. The coating is about 100 μm thick and was deposited at 6.9 ma/cm^2. The coating is uniform around the radius which has led to corner rounding. Note that the mounting material has pulled away from the specimen leading to the granular appearance outside of the coating.

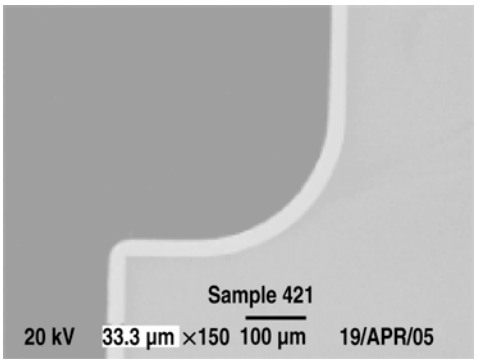

Fig. 3-57. The gold electroplated coating on a 6 mm diameter specimen with a 0.2 mm concave corner radius. The coating is 25 μm thick and was deposited at a current density of 4.3 ma/cm^2. The coating is uniform throughout the corner.

Interestingly, when a sharp concave corner was plated at a low current density, the coating was thicker in the corner than in the adjoining parallel regions (Fig. 3-58). This is opposite to the coating distribution that would have been predicted from the electric field alone. As a result of the thicker coating, the sharpness of the corner is increased under these conditions. When the same sharp corner of Fig. 3-58(a) was plated at a high current density, exactly the opposite effect was produced. A deep groove formed in the corner [Fig. 3-58(b)]. This is a very dramatic effect. The groove is only a few microns thick in the corner and is about 100 μm thick elsewhere. How can this difference between these two coating distributions produced by the high and low current densities be explained? One possible explanation is that because of the higher current density the electric field component of the deposit is larger and this affects the distribution of the deposit in and near the corner. However, this explanation is not entirely satisfactory because a small diameter specimen with the same corner radius coated under similar conditions had a very narrow crack as shown in Fig. 3-58(c). At this time more work is required to elucidate the mechanism of groove formation.

3.14.4. Future Work

There are two studies that might spread some light on the mechanism causing the grooves. It was suggested in discussions of this paper that ultrasonic agitation of the electrolyte would tend to produce a more uniform concentration throughout the electrolyte. And, calculation of the electric field variation at the corners for various corner radii and specimen diameters would be revealing.

The specimen arrangement of this study was such that the corners faced the anode. It would be interesting to examine what would happen if the corners face away from the anode. Finally, since the groove differed significantly between the 6 mm and 3 mm diameter specimens it would also be of interest to examine the electroplated corners in 1.5 mm diameter specimens which are the diameters of typical small hohlraums.

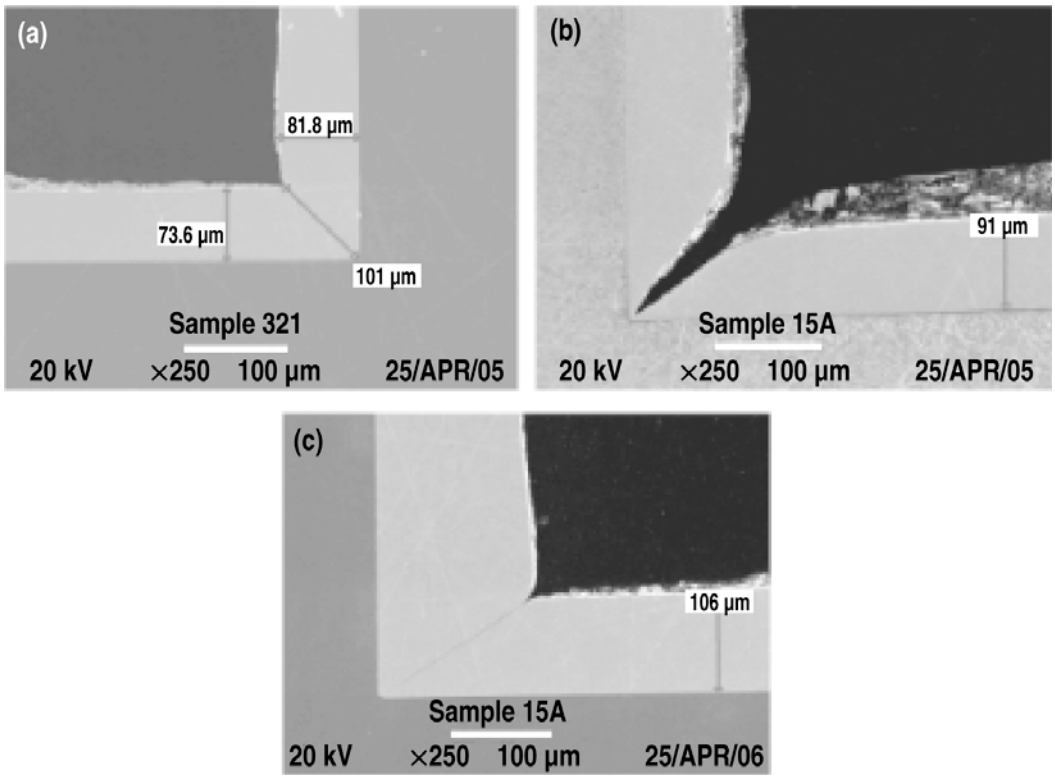

Fig. 3-58. SEM of electroplated corners. (a) The gold electroplated coating on a 6 mm diameter specimen with a 0.005 mm radius concave corner. The coating is about 80 μm thick and was deposited at a current density of 4.3 ma/cm^2. The coating is thicker at the corner than in the parallel sections. The thicker corner leads to a sharpening of the corner radius. (b) The electroplated gold coating on a 6 mm diameter specimen with a 0.005 mm radius concave corner. The coating is about 90 μm thick and was deposited at a current density of 6.9 ma/cm^2. There is a wide deep groove in the corner. (c) The electroplated gold coating on a 3 mm diameter specimen with a 0.005 mm radius concave corner. The coating is about 100 μm thick and was deposited at a current density of 7.4 ma/cm^2. A very narrow groove is present in the corner.

3.15. MULTI-LAYERED DEPLETED URANIUM AND GOLD "COCKTAIL" HOHLRAUMS

H.E. Wilkens, J. Gunther,[1] M.P. Mauldin, A. Nikroo, J. Wall, D. Wall, and R.J. Wallace[1]

General Atomics
[1]Lawrence Livermore National Laboratory, Livermore, California

3.15.1. Introduction

The calculated efficiency of the energy conversion that takes place at the hohlraum wall increases with the addition of a high-Z material like depleted uranium to the traditional gold hohlraum [3-102]. The process of making multi-layered depleted uranium (DU) and gold "cocktail" hohlraums is being developed in a sputter-coater recently designed and assembled at General Atomics. Experimenters at Lawrence Livermore National Laboratory (LLNL) have been making cocktail coatings by co-sputtering DU, Dy, and Au from the same sputter source, though the performance of the co-sputtered materials are not consistently meeting the theoretically predicted efficiency increase [3-103]. Experiments and calculations show that the likely culprit is oxidation of the DU and Dy. Therefore the motivation to create multi-layered films is to encapsulate the DU in gold, disrupting the path of oxygen into the cocktail. Current design requirements do not include Dy in the multi-layered films. Early experimental results show that the multi-layered cocktail films show promising resistance to oxidation.

3.15.2. Equipment

The main chamber of the deposition system used to produce multi-layered cocktail materials, diagrammed in Fig. 3-59, consists of six fixed magnetron [3-104] sputter sources, also called guns, and a rotating part holder arm. Each part holder on the arm, designed to sit opposite a given gun, also rotates. The position of the part holder arm is computer controlled, allowing precise timing of the deposition on a given mandrel — an important feature since the timing of the sputter deposition defines the thickness of the various layers in the cocktail material. Due to safety concerns related to the use of radioactive depleted uranium, the coater sits in a HEPA-filtered fume hood, as does the dedicated lathe used for machining cocktail-coated parts.

3.15.3. Results and Discussion

It is well known that materials deposited by magnetron sputtering contain residual stress [3-105], so the primary experimental challenge in producing the cocktail hohlraum coatings has been reduction of stress in the coatings. Such stress depends primarily on the pressure at which the material is coated, and if not controlled can lead to materials which crack and disintegrate when the constituent DU comes into contact with air. By systematically examining the cocktail coatings at various pressures, a regime in which low-stress coatings are produced has been found.

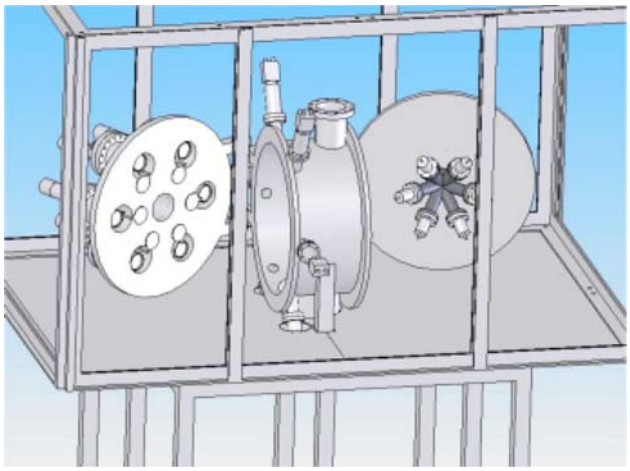

Fig. 3-59. This SolidWorks® diagram of sputter deposition system shows the position of the six guns on the left chamber door, and the rotating part holders positioned opposite the guns on the right chamber door. View ports for monitoring the process are located on the main chamber at each gun location. The chamber is shown inside the fume hood designed to hold it.

To create a cocktail cylinder, a rotating acrylic mandrel, machined in the shape of a cylinder with the desired dimensions, is indexed in front of the Au and DU guns. Using the measured deposition rates for each material, the thickness of a given layer is defined by the amount of time the mandrel sits in front of a given gun. The thicknesses are set by the desired composition of the total cocktail coating. A 75 at. % DU:25 at. % Au cocktail composition, for example, requires layer thicknesses of 30 nm DU and 8.2 nm Au, respectively. These layers are repeated many times to create a cocktail coating on the order of a couple of microns thick. A thin (100 nm) Au layer is deposited under the cocktail multi-layers, as is a thick (>2 μm) Au capping layer on top of the cocktail material to protect the cocktail coating from oxidation. After the mandrel is removed from the coater, approximately 22 μm of gold is electroplated onto the sputtered material to provide structural support. The full thickness of the coated material is back-machined to the desired length, and subsequently the mandrel is leached in acetone to provide a free-standing cylinder, an example of which is shown in Fig. 3-60. The free-standing cylinders can then be used in the fabrication of cocktail hohlraums, which is currently done at LLNL.

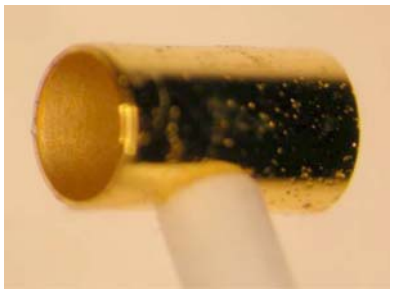

Fig. 3-60. This free-standing, 1.2 mm diameter, 2.1 mm long cylinder is the result of a low-stress cocktail coating on an acrylic mandrel.

Free-standing foils of hohlraum wall material are being produced for burn-through and re-emission experiments. These experiments are designed to test the efficiency of materials before being used in a fully integrated hohlraum [3-106]. Free-standing foils of Au, cocktail multi-layers, and DU with 50 nm Au capping layers are created in the cocktail sputter system by depositing material onto stretched cellulose acetate films. After sputtering the materials onto the film, the cellulose acetate is leached in acetone, leaving a free-standing foil

approximately 1 cm in diameter which can be cut to required dimensions. Free-standing foils of total thickness between 0.6 μm and 3 μm have been successfully produced for LLNL and SNL for this purpose, and have proved to be quite robust.

Since the results of experiments that test the efficiency of hohlraums are only meaningful when the composition of the hohlraum is well understood, great efforts are going into the proper characterization of the multi-layered cocktail materials. Depth profiling Auger electron spectroscopy (AES), which uses a beam of electrons to knock electrons out of inner-shell orbitals which have an element-specific energy, is used to measure the concentration of oxygen within the multi-layers of the cocktail material. AES measurements made at GA indicate low oxygen content during deposition, as shown in Fig. 3-61 where < 4 at. % oxygen is measured in the bulk, which is typical of the multi-layered Au and DU materials that are being produced. The multi-layer characteristics can be easily observed in the AES plots, as well as the targeted atomic percentage of 75 at. % DU:25 at. % Au. Proton backscatter (PBS) measurements carried out with the Nuclear Microprobe in the Center for Accelerator Mass Spectrometry at LLNL [3-107, 3-108] confirm less than 5% oxygen in the bulk.

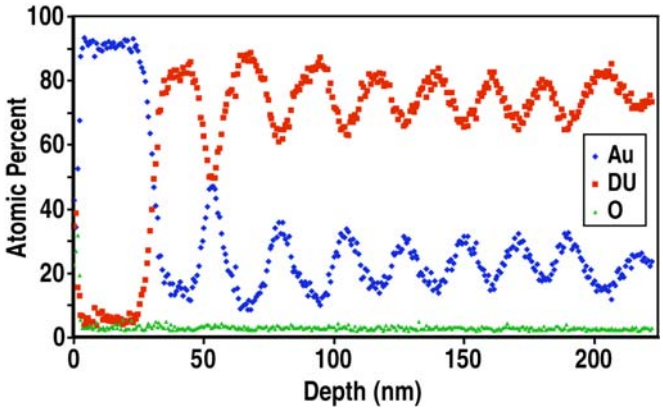

Fig. 3-61. Auger depth profile of a free-standing cocktail foil with targeted layer thicknesses of 50 nm Au/(30 nm U/8.2 nm Au) × 40/50 nm Au.

Conclusions and Future Work

Although still in the early development stage of the cocktail sputter system, free-standing cylinders and foils containing multi-layered DU and Au have been fabricated, and hohlraums of sufficiently high quality haven been used in experiments on OMEGA. In regards to the first GA cocktail cylinder shot at OMEGA, Ogden Jones of LLNL said "…this cocktail barrel is the highest Tr ever for a "cylinder only" cocktail hohlraum! It is only one data point, but this is extremely promising." The process will soon be extended to fabricating NIF-scale hohlraums, which are approximately 5 mm in diameter, so will require optimization of sputter coating parameters for that geometry. We look forward to future collaborative work with LLNL to characterize the quality of the multi-layered coatings with transmission electron microscopy.

3.16. DEVELOPMENT OF SPUTTER-COATED GLASS PERMEATION BARRIER

J.S. Jaquez, E.L. Alfonso, and A. Nikroo — General Atomics

3.16.1. Introduction

Room temperature NIF shots will require deuterium filled targets with room temperature half-lives of a few days while those for current shots at SNL's Z facility require half-lives of a few weeks. Polyvinylalchol (PVA) coating has been used in the past as a permeation barrier for CH against deuterium and other gases of interest for room temperature shots. One of the major drawbacks of PVA is the uniformity of the coating. Figure 3-62 shows the wall thickness variation for 60 μm thick CH shell coated with PVA. The plot shows the total wall varying by 4 to 5 μm (where the CH shell has a wall thickness variation of 0.5 μm). Another drawback for using PVA as a permeation barrier is the half-life is ~10 days or less which is not a sufficient amount of time needed for experiments on the Z-facility. The process of dip coating also is not a very reproducible technique and, therefore, an alternate permeation barrier material as well as fabrication process was sought.

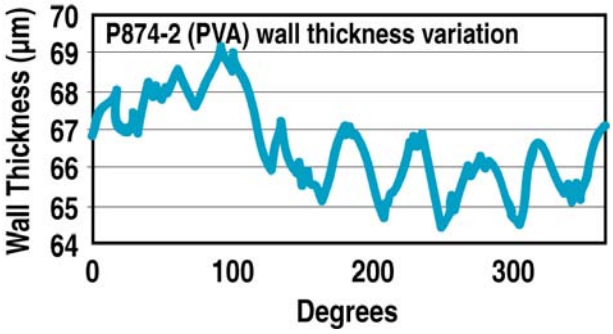

Fig. 3-62. Wall mapping of a typical PVA dip-coated CH shell shows major nonuniformities that contain higher frequency components than P1. The plot shows the total wall thickness for the PVA layer as well as the original ~ 60 ± 0.5 μm CH shell, indicating a wall nonuniformity of ~ 5 μm with frequency structure much higher than P1.

Because the half-life of deuterium through glass is very large, it was previously looked upon as an alternative permeation layer to PVA [3-109]. Most of the permeation data was collected using argon as an indicator due to the difficulties in measuring deuterium permeation. This previous work only yielded a few data points for deuterium permeation allowing only for bounds on the half-life. More recent work has allowed us to answer questions not answered by previous work with the aid of a newly adopted mass spectrometry technique (described in Section 3.1 of this report) that allows the measurement of long time constant shells. Also investigated in this study was the possibility of depositing thinner glass

layers on CH shells that are of particular importance for NIF targets. Current work has shown a half-life of ~2 to 4 weeks with a glass coating of 1.5 μm can be routinely obtained, and for the thinner glass coatings a half-life of ~1 week has been shown. In addition, we also determined that such coatings could be filled with relevant pressures (few tenths of atm) of argon needed as a diagnostic gas for implosions. Finally we investigated how to fill a shell in a reasonable amount of time in a manner that is reproducible.

3.16.2. Experimental

GDP mandrels ~2 mm in outer diameter and with a wall thickness of ~25 μm were used for this study. They were examined prior to coating for any gross defects and consistent quality from run to run. These CH shells are known to have a half-life of a few minutes. The glass layer was deposited on the CH mandrel via magnetron sputtering at coating pressures of 2, 5, and 10 mTorr. The chamber was pumped down to a base pressure of 10^{-6} range prior to coating. Coatings were performed with a MAC magnetron sputtering gun using 400 W of radio frequency (rf) power with a frequency of 13.5 Hz. The distance from the sputtering gun to shells on the pan was 8 cm.

Two agitation mechanisms were studied for randomly displacing the CH mandrels underneath the SiO_2 to see the effects on surface quality on the as-deposited SiO_2 layer. Typically three CH mandrels were coated at one time. Bouncing was initially considered due to its success in plasma polymer coatings. Bouncing was performed by attaching a metal pan to an electromagnetic shaker and finding the frequency that minimized the bounce height yet still retained a random agitation underneath the plasma source. The other agitation mechanism studied, rolling, was performed by attaching the same type of metal pan used for bounce coating to a DC motor and allowing the shell to roll along the surface of the pan. The pan was rotated counter-clockwise at 50 RPM. The rotation speed was varied to minimize the collision energy of the shells and still retain random agitation beneath the SiO_2 plasma source.

The CH mandrels pre-coating and post-coating were investigated for defects and cracks using optical microscopy. SEM images were taken for visualization at higher magnification. The surface roughness was determined by atomic force microscopy (AFM). The glass thickness was measured at a single point on the shell using interference microscopy and wall thickness variations were found using an adapted Filmetrics spectral inferometer that traced the layer thickness as a function of position along the equator of the shell (wall mapping).

3.16.3. Results and Discussion

Initially investigated was the pressure of argon in the chamber while coating. It is well known that the pressure affects the stress as well as the density of sputtered materials. SiO_2 coatings performed at 2 mTorr were cracked. The cracks are believed to stem from compressive stresses on the shell during coating. Raising the pressure to 5 mTorr reduced the compressive stress. The glass thickness uniformity was greatly improved compared to PVA. A wall mapper plot of a typical SiO_2 coated shell is seen in Fig. 3-63. This figure

shows only the wall thickness variation of the SiO_2 layer that was found to be only a few tenths of a micron.

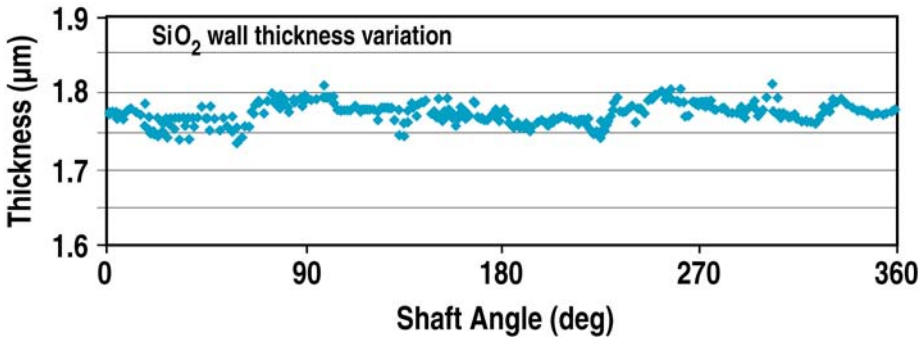

Fig. 3-63. The uniformity in SiO_2 coated shells was typically shown to be on the order of a few tenths of a micron.

The manner in which the shell is agitated plays a factor in surface quality of the SiO_2 coating. Images from optical microscopy reveal rolling to produce far few defects than bouncing. SEM images confirm what was seen from optical microscopy (Fig. 3-64). In addition, the surface finish of the shells made by rolling was much smoother than those of the bounce-coated shell. Comparisons of the AFM spheremapper traces show the rolled shells have a much smoother surface than bounced shells.

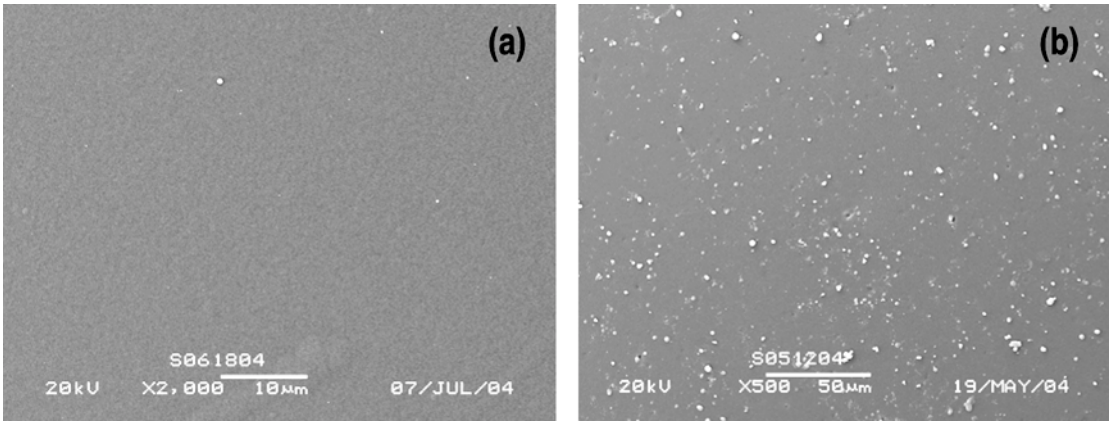

Fig. 3-64. SEM images of ~ 1.5 μm SiO_2 coatings on plasma polymer mandrels while, (a) roll coated, and (b) bounce coated. The small black dots seen in the optical images are small nodular structures embedded in the sputtered layer.

The half-life of the coatings was measured by mass spectrometry. In these measurements the shells were initially typically filled with 6.8 atm of deuterium to avoid cracking of the SiO_2 layer in the measurement process [3-110]. The manner in which the shells were agitated affected the half-life. While both agitation techniques produced SiO_2 layers with half-lives much longer than that of the bare CH mandrel, the roll-coated shells had lower permeation than those bounced. The roll-coated shells typically had half-lives on the order of 2 to 4

weeks greater than those bounced (Fig. 3-65). These time constants are appropriate for applications at the SNL's Z facility, which has a fill-to-shot time lag of around one week. In comparison, the bounced coated shells had half-lives of only a few days. The nodular structure of the SiO_2 layer for bounce-coated shells apparently allows faster permeation of deuterium compared to the more uniform structure of the roll-coated shells.

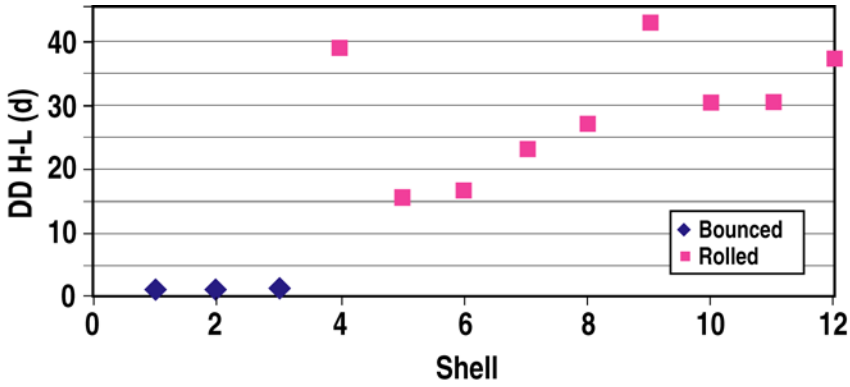

Fig. 3-65. A comparison of typical measured half-lives of roll-coated and bounce-coated shells. As can be seen the roll located shells have half-lives of greater than 2 weeks, while the bounce-coated shells only have half-lives of ~ 2 days. The half-life of the CH mandrel is only ~ 5 minutes by comparison.

The coatings were then tested at pressures as high as 20 atm. The time constant of coated shells were measured after the 20 atm fill to observe any possible degradation of half-lives due to possible micro-cracking or gross cracking of the coating at such high fill pressures. To expedite the fill process for these higher pressures, the time constant of the coatings was first determined at ~ 160°C where faster permeation is expected. These measurements along with associated destructive testing of a subset of the shells indicated that ~ 2 days fill was sufficient for complete filling of the shells. Subsequent half-life measurements at room temperature after these 20 atm fills verified that the permeation layer was not cracked as no reduction in half-life was observed.

Roll coating was also used to deposit thinner layers, ~ less than 1 μm. These thinner coatings were more difficult to measure by interferometry and had an error of ~ 0.4 μm. The coating thickness was then estimated based on the coating time and the known coating rate for the thicker coatings. While the time constant of the thinner layers decreased faster than that expected (ratio of thicknesses) the decrease was not catastrophically rapid. For example, for ~ 0.5 μm layers preliminary results show half-lives of about one week were found for some of the shells, which is sufficiently long enough for applications at NIF where the time between fill and shot is expected to be only one day.

Conclusion for Section 3.16

CH mandrels that have been successfully sputter coated with ≤ 2 μm of SiO_2 provide an attractive alternative to PVA as the deuterium permeation for ~ 2 mm diameter CH shells

used for current room temperature SNL Z-machine experiments and future NIF experiments. Results have shown agitation plays a major role in surface quality as well as permeation characteristics of the sputtered SiO_2 layer. We have shown that roll coating of shells with ~ 1.5 μm of SiO_2 produces half-lives of ~ 2 to 4 weeks for deuterium, while bounce-coated shells have half-lives of only a few days. While both are improvements over the bare CH mandrel, the roll-coated shells are highly preferred due to the increased half-life and superior surface. Coatings thinner than ~ 1 μm, appropriate for NIF applications, had shorter half-lives than expected but they were still long enough (~ 1 week) for processing of shots at NIF.

3.17. IMPROVING THE YIELD OF TARGET QUALITY OMEGA SIZE POLY-α-METHYLSTYRENE (PAMS) MANDRELS BY MODIFYING EMULSION COMPONENTS

R.R. Paguio, S.P. Paguio, C.A. Frederick, A. Nikroo, O. Acenas[1]

General Atomics
[1]California State University San Marcos, California

3.17.1. Introduction

ICF targets require shells with a high degree of spherical uniformity in order to obtain optimum implosion performance. One of the main processes in fabricating these spherical targets is the production of poly-α-methylstyrene (PAMS) mandrels. Details of the PAMS production process have been presented in previous publications [3-111 to 3-115]. These PAMS mandrels are then overcoated with Glow Discharge Polymer (GDP) to the specific thickness required by the individual experiments [3-111]. After overcoating, the PAMS mandrel is removed by pyrolysis and a hollow sphere (shell) of GDP remains [3-111 to 3-112]. Thus, the final shell target for a specific type of ICF experiment is produced.

Because the PAMS mandrel acts as a skeleton for the final shell, the PAMS mandrel must be very spherical with minimal surface roughness. If the PAMS mandrels do not meet these specifications, the final target will not meet the required specifications for implosion. The overcoat can only be as good and the mandrel. The two main specifications for these OMEGA size PAMS mandrels are the sphericity or out of round (OOR), defined as $\text{Diameter}_{\max} - \text{Diameter}_{\min}/2$ and the wall uniformity or nonconcentricity

$$\left[NC = \frac{\text{Offset of the Outer and Inner Wall}}{2(\text{Avg. Wall Thickness})} \right] .$$

For OMEGA size shells the OOR needs to be less than 1 μm and the NC ≤ 5%.

While these present the minimum requirements for the quality of PAMS shells, the more stringent requirement is meeting the surface finish specification at all length scales beyond the OOR. The surface roughness of the shells at all length scales is measured by spheremapping the shells using an atomic force microscope (AFM) [3-116]. The AFM measures the power spectra of the shell at various modes. The power spectrum from the shell is compared to the National Ignition Facility (NIF) standard. The NIF standard is the amount of allowable power or surface roughness that is tolerable at various modes around the shell. The power spectra for the targets must be below the NIF standard to meet the target's surface roughness specification. Factors that can affect the surface quality of the PAMS mandrels are the presence of vacuoles on the shell and residue left on the surface of the shells. This must be minimized in order to produce PAMS mandrels that meet the surface specifications. The traditional production process for making OMEGA size (~800 to 1000 μm) PAMS shells was developed previously, but has had a low yield of only 18% for the number of target

quality batches based simply on the o.d. and NC specifications. However, the quality of shells within a batch, usually containing about a thousand shells, is comparable and there is little variation in shell quality within a given batch. Therefore, tens of high quality batches produced from ~ 100 production runs could normally supply the shells needed for producing the final GDP shells for ICF experiments. However, a problem arises if a batch of a specific unavailable diameter is urgently needed for a newly designed experiment. Then a higher yield of target quality batches is extremely crucial for successful fielding of the experiment. Because of this possibility, we began investigating possible improvements to the OMEGA size PAMS mandrel production with the hope of removing the apparent inherent instability of the process from run to run.

The standard OMEGA PAMS mandrel process developed previously uses 0.30 wt% poly vinyl alcohol (PVA) in the outer water solution [3-111, 3-113, 3-115]. A salt solution containing ammonium chloride is also added to the W2 in the collection beaker after the beaker is placed into the curing bath [3-115]. The addition of the salt solution helps reduce the number of vacuoles, which can cause low mode surface roughness. The yield of shells that meet the spherical specifications of OOR and NC is ~18% (Fig. 3-66). We will discuss the modifications that improved the yield of batches that met the specifications from 18% to 87%.

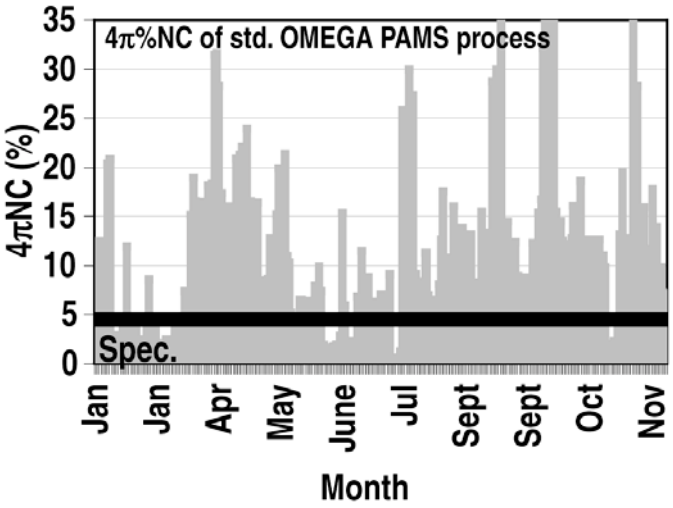

Fig. 3-66. The NC of the shells fabricated using the standard OMEGA PAMS process. The yield of PAMS batches that meet the NC Specifications is low. OOR plot is similar to this. The solid horizontal bar denotes the required specification. R is similar.

3.17.2. Results and Discussions

We pursued several different modifications to the baseline process. The first modification of the OMEGA PAMS process was to fabricate shells using our standard NIF PAMS mandrel (Diameter > 2000 μm) process. This process uses 0.05 wt% PAA in the W2 solution

instead of the standard 0.30 wt% (PVA) solution [3-114]. The reason for using the PAA is that it appears to have a greater interfacial surface tension than the PVA [3-114]. This increased surface tension would naturally lead to better OOR and in practice has led to better NC, although the exact reason for this has not been determined. This modification was a key factor in producing NIF size PAMS shells that met the spherical specifications. OMEGA PAMS mandrels fabricated by using this method met the NC and OOR specifications. However, many vacuoles were observed on the shell**,** which affected the surface finish of shells adversely. In addition, this fabrication process is much longer (~ week) compared to the traditional PVA process (1 day). Given the frequency of OMEGA target shots, the shorter process is preferred in production mode.

The second modification that was attempted was the addition of PAA to our standard OMEGA PAMS production procedure without increasing the surface roughness. A small addition of PAA could increase the interfacial tension in our PAMS emulsion, which could possibly lead to shells with better OOR and NC. The incorporation of PAA involved adding a small amount (10% of volume) of 0.10 wt% PAA to the W2 solution in the collection beaker. This is similar to addition of a salt solution to the W2 in the standard OMEGA PAMS production process [3-115]. PAA is incompatible with the salt solution that is added in the W2 solution causing the salt to precipitate out of solution. Because of its incompatibility with PAA, the ammonium chloride was removed from this modification. Removing the ammonium chloride from the process increases the possibility of producing shells with vacuoles. Nonetheless, OMEGA size PAMS mandrels were produced with this procedure and it was found that the yield of shells based on OOR and NC criteria was greatly increased from 18% to 50%.

While this increase in yield was indeed encouraging, we examined a third modification in hope of an even larger yield. An extension of the previous experiment was to increase the PVA concentration in the W2 solution from 0.30 to 1.0 wt%. This modification was aimed at further increasing the interfacial tension of the W2 than in the second modification, in the hope of further improving the quality of batches with respect to OOR and NC. The PAA addition to the W2 was still implemented as in the previous experiment. This last procedure did indeed result in a substantial increase in the yield of target quality batches from 18% to 87% based on simple OOR and NC requirements (Fig. 3-67). We did not investigate increasing the PVA content further; however, we hope to be able to extend this work to higher PVA concentrations in the future.

One other concern with adding PAA to the W2 or increasing the concentration of PVA even at the 1% level was that it would increase the high mode outer surface roughness of the shell. This has been observed in fabrication of NIF size PAMS and has been attributed to the residual PAA on the shell surface after fabrication. However, we found that the vacuole content and the surface finish of shells (Fig. 3-68) made with this W2 modification were not adversely affected.

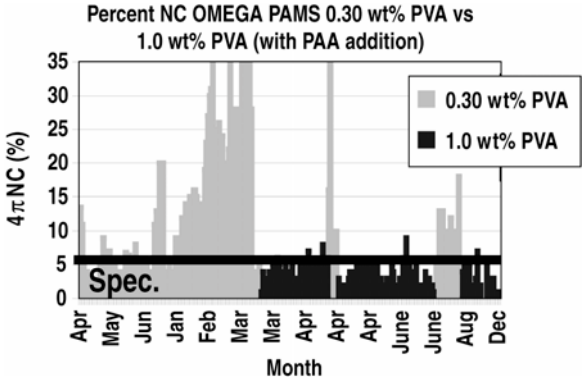

Fig. 3-67. NC of OMEGA size PAMS shells made with the modifications to the W2. The OOR plot is similar to this. The solid horizontal bar denotes the required specification.

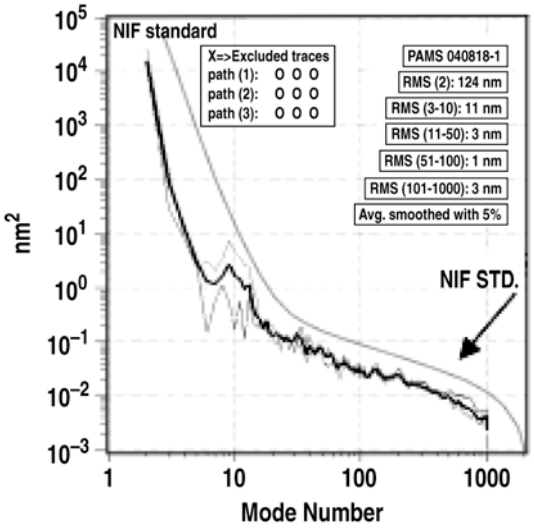

Fig. 3-68. The power spectrum of a PAMS mandrel fabricated with the third set of modifications to the W2 is still below the NIF standard showing that the mandrels still meet the surface roughness specification

Conclusion for Section 3.17

An improvement to the yield of target quality PAMS mandrel batches was achieved by increasing the PVA concentration from 0.30 to 1.0 wt% and the addition of 0.10 wt% PAA to the W2 solution (Fig. 3-69). This increased the yield of batches of shells that met the requirements for OOR and NC from 18% to 87% with no increase in surface roughness when compared to the PAMS shells made with the traditional OMEGA PAMS production process. The vacuole content and the outer surface finish of shells were not adversely affected by these modifications. As a result of these experiments, this modification has been implemented into the standard production process of fabricating OMEGA size PAMS mandrels.

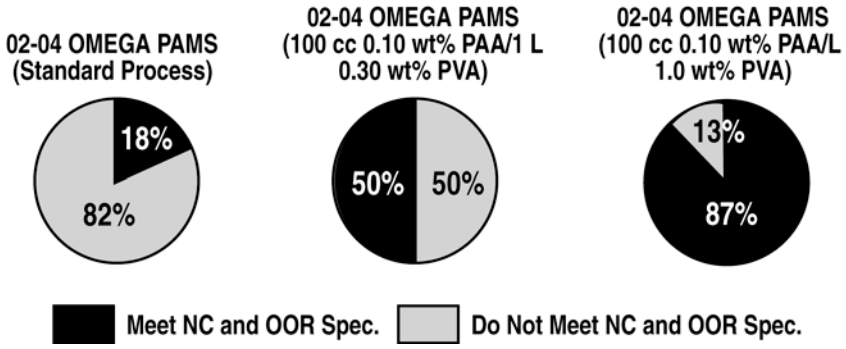

Fig. 3-69. The improvements made to the OMEGA PAMS shells that meet the NC and OOR specification by modifying the W2 solution.

3.18. VAPOR-DEPOSITED POLYIMIDE COATINGS WITH IMPROVED SURFACE SMOOTHNESS

K.-C. Chen and A. Nikroo — General Atomics

3.18.1. Introduction

Vapor-deposited polyimide shells have been developed for direct-drive-implosion experiments because of their superior mechanical and thermal properties and ability to retain these properties in a radiation environment. To date, the surface roughness of polyimide shells, produced by chemical vapor deposition of pyromellitic dianhydride (PMDA) and 4, 4'-oxydianiline (ODA), is greater than is desirable [3-117 to 3-124]. Numerous efforts have been made to improve the smoothness of as-deposited polyamic acid (PAA) coating, or post-processing to smooth the rough PAA surface before converting them into polyimide shell [3-121].

Roughness was mainly attributed to off-stoichiometric composition and abraded damages due to mechanical agitation. We observed, at near-stoichiometry deposition condition, the coating surface between two stuck shells is very smooth, while the portions of the shell surface that contact other shells or pan are rough. This confirmed that the surface roughness is mainly caused by shell-shell and shell-pan abrasion damages, as described by Roberts et al. [3-121]. We tried a few gentler agitation methods, such as tapping, shaking and rolling, but have not succeeded in eliminating mechanical damage to the shells. This damage is due to appreciable agitation force which is required to loosen the strong static-charged shells from the pan followed by continually rotating the shell for uniform coating thickness. A few small stainless steel balls were added to free up the stuck shells but the results show the heavier balls actually created rougher coating.

3.18.2. Wire Net Approach to Eliminate Surface Mechanical Damages

We confirmed the stoichiometry in the deposited film by monitoring and matching the deposition rates of PMDA and ODA with glass slides. Two evaporators containing PMDA and ODA were set at 140°C and 167°C and their fluxes over the pan area were determined to be 1.26×10^{-5} mole/h·cm^2 and 1.1×10^{-5} mole/h·cm^2, respectively. Therefore, the flux was only slightly PMDA rich during the coating. Infrared spectroscopy confirmed no large excess of either monomer. During coating, chamber pressure was maintained at 5×10^{-6} Torr and a filament was used to provide thermal electron to remove static charge.

To minimize shell-shell and shell-pan contacts, we used a plastic wire-net made of twist-weave filament as a holder (Fig. 3-70). A plastic wire-mesh was preferred over metal wire net since the melt-spun plastic filaments are smoother. The dimension of the twist-weave and opening was selected so that the opening acts as a shallow well. The width of twist-weave prevents shells from contacting each other but allows shells to roll into adjacent openings by a small tapping force using a leverage motion. The net opening is ~0.6 mm and the width of

filament tow ~0.2 to 0.3 mm for a 1 mm-size shell. The size of wire-net should scale with the size of the shell, e.g., wire-net we used for 1 mm size shells did not work well for 2 mm shells.

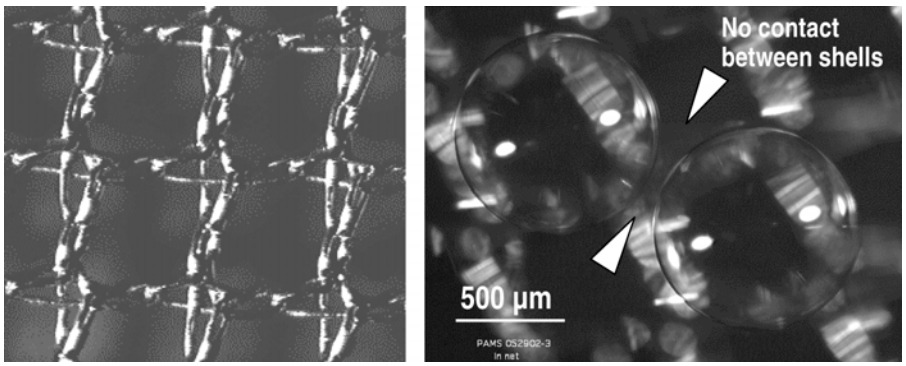

Fig. 3-70. (a) The plastic twist wire-net used for holding the shells during coating and (b) no contact between shells when shells sit in the wire-net.

The wire net was stretched between a metal ring which tightly fits to a cylindrical block to provide tension, then on the shaft of a tilted motor via a center-drilled hole. The pan was tilted 25 deg to constrain the shells' motion to a small region. Finally, another wire-net was used over the shell to prevent shell loss during tapping. The wire-net mandrel holder was rotated at ~10 rpm and was tapped at 15 times per minutes (0.07 Hz).

3.18.3. Surface Quality of As-Coated Polyamic Acid Shells

The surface smoothness of the as-deposited PAA coating becomes much smoother and meets the NIF standard using the wire-net holder, as shown by the AFM traces and power spectra (Figs. 3-71 and 3-72). The shell has root-mean-square background roughness of 6 nm for modes 100 to 1000.

As compared to the solid pan, the wire-net reduces the shell-shell and shell-pan contacts. In a solid pan, a closest-packed shell has seven contact points, while a shell in the wire-net has 3 or 4 contact points at rest. When the solid pan rotates, new contact points continuously form between the shells and the solid pan. In contrast, the shells in the wire-net flipped to adjacent openings upon tapping by a cantilever mechanism thus only a few new contact points are created. Also, shells and wire-net contacts are located below the equators of the shells and are shadowed by the shells themselves thus minimizing possible build-up at these contacts during coating.

The tension of the stretched wire-net helps to reduce the tapping force required to flip the shells. The cantilever motion of the shell also reduces the impact force. Initially, using the wire-net holder, some isolated surface damages were still observed. Their occurrences were later correlated with the excess travel distance of the shells in the net. A cylindrical ring made of the same wire-net (i.e., a small fence) was added to limit the shells' movement by a few quantized cantilever movements and succeeded in eliminating these large defects. From

these results, we concluded that there is a small damage threshold for PAA coating during impact since a shell weighs only 39 μg. The damage threshold might also be affected by whether impacts are in normal or shear direction.

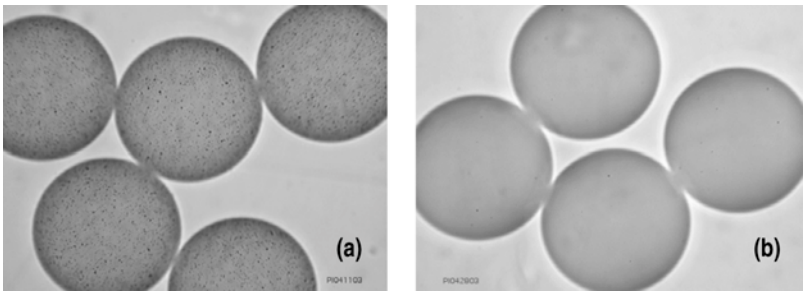

Fig. 3-71. (a) Shells prepared with gentle rolling and tapping in solid pan. Stainless steel balls were added to prevent static-charged shells from adhering to pan. (b) Shells prepared from the wire-net type holder with synchronized tapping.

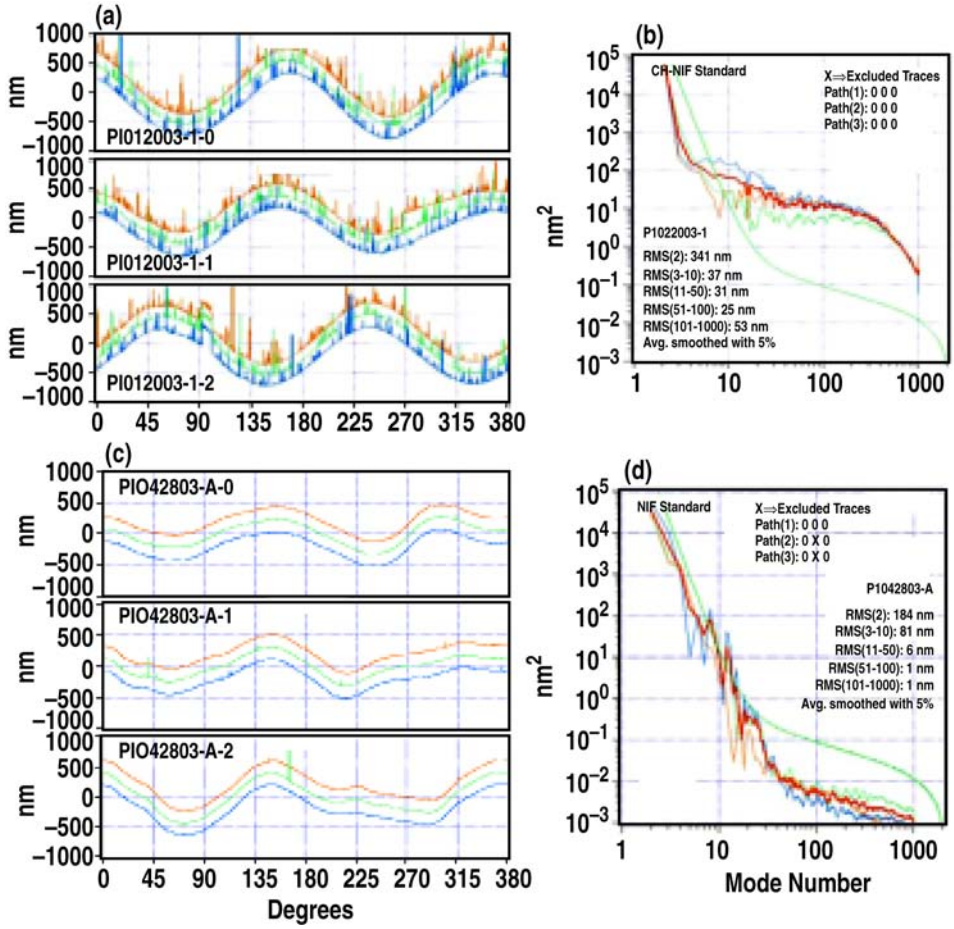

Fig. 3-72. (a)(b) AFM traces and power spectrum of a shell made with gentle tapping and stainless steel balls addition in a rotating solid pan. (c)(d) AFM traces and power spectrum of shell made with wire-net type container.

To prevent ineffective tapping, we adjusted the frequency of tapping with rotation so that the tapping occurs when the shells are at the highest position in the holder. This allows shells to cascade down in a more or less parallel fashion thus avoiding hard impacts between the shells. Timing and frequency of tapping are important to achieve uniform coating.

3.18.4. Surface Quality and Integrity of the Polyimide Shells

Matching pressure and heat treatment profiles to 300°C are used to prevent shells from bucking or fracturing during the simultaneous decomposition of mandrel and conversion of PAA to polyimide. We prepared polyimide shells that have wall thicknesses ranging from 3.8 to 7.6 μm. After pyrolysis, the walls shrunk to 76 ± 6% of PAA thickness. The shell diameter expanded 4.6 ± 3%. This spread of the wall shrinkage and diameter expansion is attributed to the variation of PAA and mandrel thickness.

When too many shells were processed together, the surface of the polyimide shells became rough, although the as-deposited coating was smooth. It may be due to saturation of PAMS vapor inside the small furnace and re-condensation as small particulate. Figure 3-73 shows the AFM traces and power spectrum of a successfully processed polyimide shell. The power spectrum is near the NIF standard. The interferometer (WYKO) measurements show the surface roughness rms is 3 nm. The AFM patch scan shows the surface rms roughness to be 23 nm.

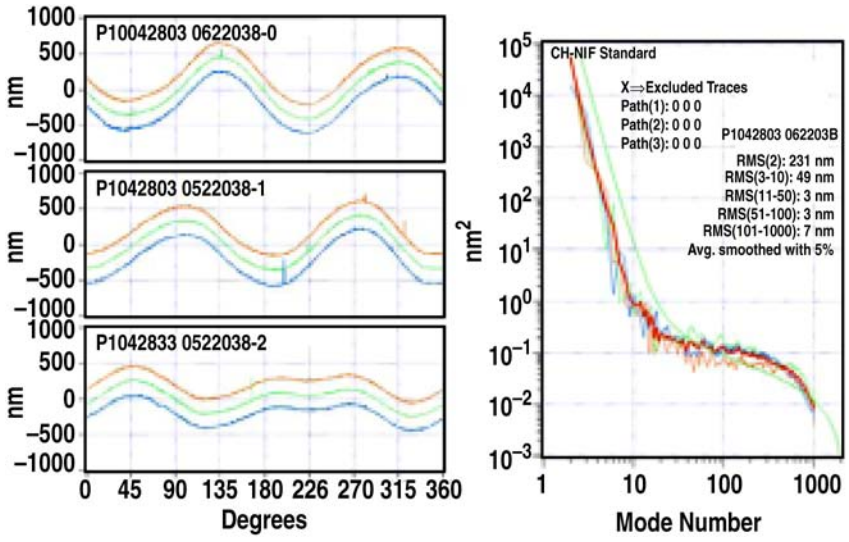

Fig. 3-73. AFM traces of polyimide shell and power spectrum of polyimide shells. The final surface smoothness of polyimide depends on heat treatment and pressure profiles.

We tested the integrity of the polyimide shells by determining the shell's argon permeation using XRF. The results show the half-life of the argon permeation is 1167 minutes. Additional permeation tests were performed in MS using He gas at 24°C, 100°C,

150°C and 200°C. The half lives for helium at these temperatures are 3.6 ± 0.5, 1.3 ± 0.2, 0.8 ± 0.1, and 0.4 ± 0.02 min, respectively.

Summary for Section 3.18

We have successfully improved the surface roughness of the polyimide shells by using a wire-net shell holder, which reduces the shell-shell and shell-pan contacts and impact force. The surface roughness of polyimide shells meets the NIF standard and has root-mean-square roughness ranging from 3 to 23 nm. The polyimide shells hold argon and helium indicates the wall is free of pin-holes.

3.19. FABRICATION OF GRADED GERMANIUM-DOPED CH SHELLS

K.-C. Chen, H. Huang, A. Nikroo, S.A. Letts,[1] and R.C. Cook[1]

General Atomics
[1]Lawrence Livermore National Laboratory, Livermore, California

3.19.1. Introduction

A graded germanium-doped CH shell is the current backup design for the NIF ignition campaign. The graded germanium shell design has four layers — with two Ge doping middle layers at 0.75 at. % and 0.38 at. % [Fig. 3-74(a)] [3-125, 3-126]. The shell is ~2 mm in diameter and has a total wall thickness of 160 μm. This graded Ge-doped design tolerates rougher surface finish than the undoped shells and has a less stringent surface smoothness standard. The new surface smoothness standard allows six-fold increases in power over the original standard for the modes greater than 23 [3-127]. The NIF specifications call for Ge concentrations to be within ± 10%, layer thickness within ±0.5 μm of the design values. The surface smoothness of the shell needs to meet NIF surface smoothness standard.

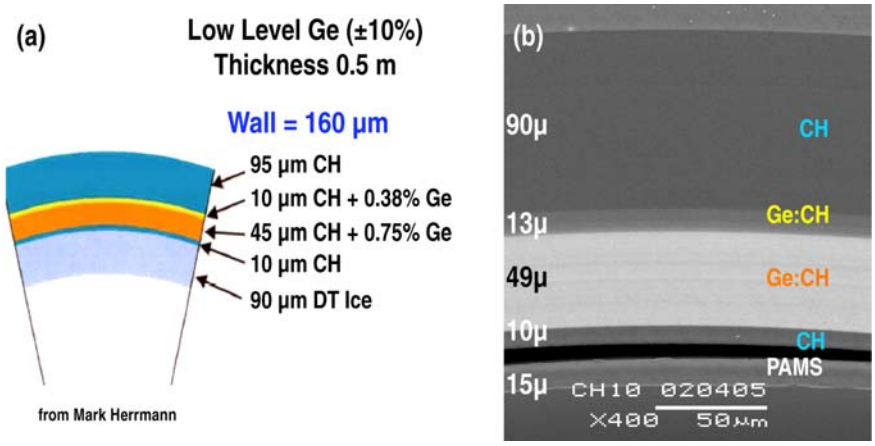

Fig. 3-74. (a) The graded Ge-doped CH shell design for NIF ignition. (b) The back-scattered SEM image through the graded Ge shell's equator. Two lighter-colored layers have Ge doping. The brightest layer contains higher germanium. The PAMS mandrel detached from the wall due to polishing.

3.19.2. Control of Germanium Dopant Concentrations and Layer Thickness

We fabricated the graded Ge-doped GDP shell with usual hydrogen flow at 10 sccm and trans-2-butene is at 0.17 sccm. Details of GDP coating have been described elsewhere [3-128 to 3-133]. Incorporation of Ge dopant is achieved by adding the vapor of $(CH_3)_4Ge$, which is controlled by a special low-flow differential pressure transducer (MKS 698A01TRB) capable of maintaining stable flow rate less than 0.05 sccm [3-130].

The stability and reproducibility of the flow control is the main concern for Ge doping levels less than 1 at. %. The desired Ge flow controller settings were found by successively extrapolating and confirming with XRF analyses on tryout runs. By repeating the tryout runs, we reduced the deviation of Ge concentration to around 10% for the same controller setting by using zero-corrected controller settings. The fluctuation increases to ~17% below 0.3 at. % Ge doping, where fluctuation and drifting of controller zero become significant. Germanium concentrations determined from XRF were compared with those determined from quantitative contact radiograph calculations. Within the experimental errors, Ge concentrations from both methods are identical (values differ by 3%, but both methods have an estimated ~10% uncertainty).

The coating rate is a function of Ge concentration. Using the tryout runs, we determined the coating rates for 0.75 at. % and for 0.38 at. % Ge to be 0.51 and 0.46 μ/h, respectively. Standard deviation of coating rates is ~0.03 μm/h, which contributes thickness variations of ~10%. For the 45 and 90 μm layers, the variation can be as large as 4.5 and 9 μm, which is higher than the tolerance of NIF specifications. Therefore, the coating run needs to be stopped for "break-point" measurements in order to have better thickness accuracy.

3.19.3. Characterization of Graded Germanium-Doped Shells

We made the first batch of graded Ge-doped shells using the determined Ge flow controller settings and coating rates. The back-scattered scanning electron micrograph of the shell's cross section clearly shows distinct layers due to atomic number contrast [Fig. 3-74(b)]. Two Ge-containing layers are brighter than the two undoped layers. The cross-section image matches the NIF design.

The Ge concentrations and precise layer thickness were determined by nondestructive quantitative contact radiography [3-134]. The Ge atomic percent was determined by fitting the measured transmission profile with a model so that the calculated profile matches the measured profile. Figure 3-75(a) shows the x-ray contact radiograph image. The measured normalized transmission intensity profile versus shell radius of the graded Ge shell, obtained by averaging line-outs of radiograph image, such as X-X´, is shown in Fig. 3-75(b). The zero transmission area, where full-exposure occurs, is outside the shell. The transmission curve shows a few discontinuities which delineate the layer boundaries. The layer thickness was precisely determined by using the second derivative of the transmission curve to ± 0.2 μm when layer boundary is distinct. However, the boundary between the mandrel and the first layer of freshly deposited undoped CH is not clear due to their similar density measurements (mandrel density 1.09 and CH density 1.08-1.1). Because of this, the thickness error for the first CH layer is higher at ± 0.5 μm. Fortunately, we can verify the first layer thickness using white light interferometer measurement by stopping the coating run and performing a "break point" measurement.

The concentration model is based on the undoped CH layer which consists of one carbon plus 1.4 hydrogen. This elemental composition is based on previous analyses of carbon and hydrogen on undoped CH. The density used for CH is 1.08 to 1.10. These values give a

very good match of the calculated curve with normalized transmission curve for the outer CH layer. The Ge atom percent was determined by incorporating Ge into undoped CH so that the calculated curve match the measured normalized transmission profile. The densities of the Ge-doped layers, which were verified on single layer tryout runs, are 1.12 g/cc for low Ge layer and 1.18 for high Ge concentration layers.

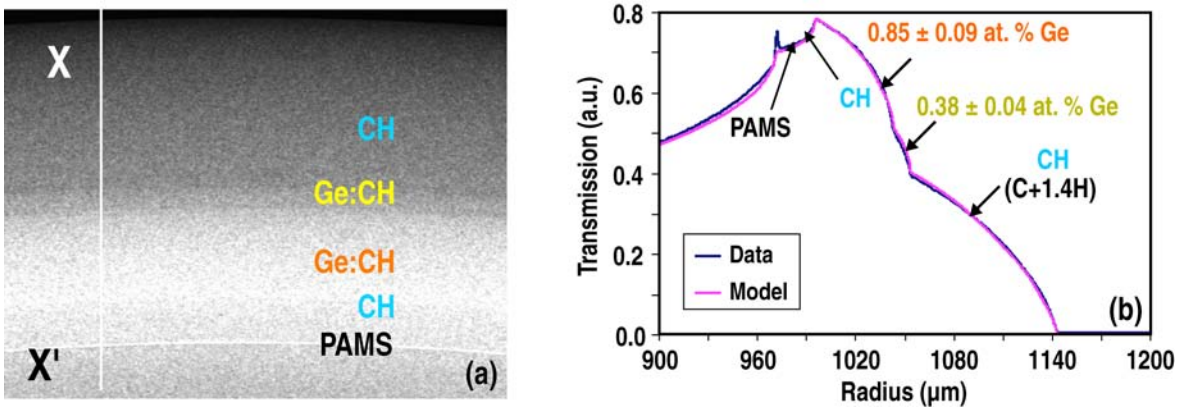

Fig. 3-75. (a) The contact radiograph image of graded Ge-doped shell. The boundary between PAMS mandrel and the undoped CH is not distinct due to similar density results. The transmission versus shell radius plot is obtained by averaging thousands of radial line outs, like X-X´ line shown here, to obtain the transmission plot versus radius shown to the right. (b)This graph is obtained by digitizing, normalizing and averaging the transmission intensities along the radial X-X´ sections. The zero transmission (full exposure) to the right is outside the shell. Each curvature presents a layer in the shell wall.

The quantitative radiograph result shows we have successfully produced a four-layered graded-Ge CH shells. The shells have an inner 9.5 ± 1.1 μm undoped GDP layer, followed by a 47.8 ± 0.5 μm 0.83 ± 0.09 at. % Ge-doped CH, and 10.2 ± 0.4 μm thick 0.38 ± 0.04 at. % Ge-doped CH and then 89.6 ± 0.5 μm of undoped CH. Except for the thickness of the top layer which is slightly less than the design specification, the three other layers are coated slightly thicker than the design specification to account for the expected shrinkage after mandrel removal.

The AFM power spectra of the shells are compared to the new NIF standard provided by Mark Herrmann. The power spectrum of the shell is below the new NIF standard (Fig. 3-76).

3.19.4. Removal of Mandrel by Pyrolysis

The mandrel was removed at 305°C for 10 to 20 h in flowing nitrogen. The diameter, wall shrinkage and germanium concentrations of the pyrolyzed shells were again determined by quantitative contact radiography. Figure 3-77 shows the mandrel was removed from the thick-walled shell and the distinctive layered structure remains intact. The shell has layer thicknesses of 10.3, 45.9, 9.4, and 83 μm (±0.2 μm). The analysis of the shell before and after 305°C, 10 h heat treatment shows there is 0.4% diameter shrinkage and 5.7% wall shrinkage. The Ge concentrations, within the measurement error bar, did not change. We used an automated white light interferometer (WYKO) to examine the smoothness of the

inner surface on fractured pieces of a shell that had been pyrolyzed at 305°C for 20 h. The root-mean-square surface roughness of these shells ranges from 1.1 to 6.5 nm.

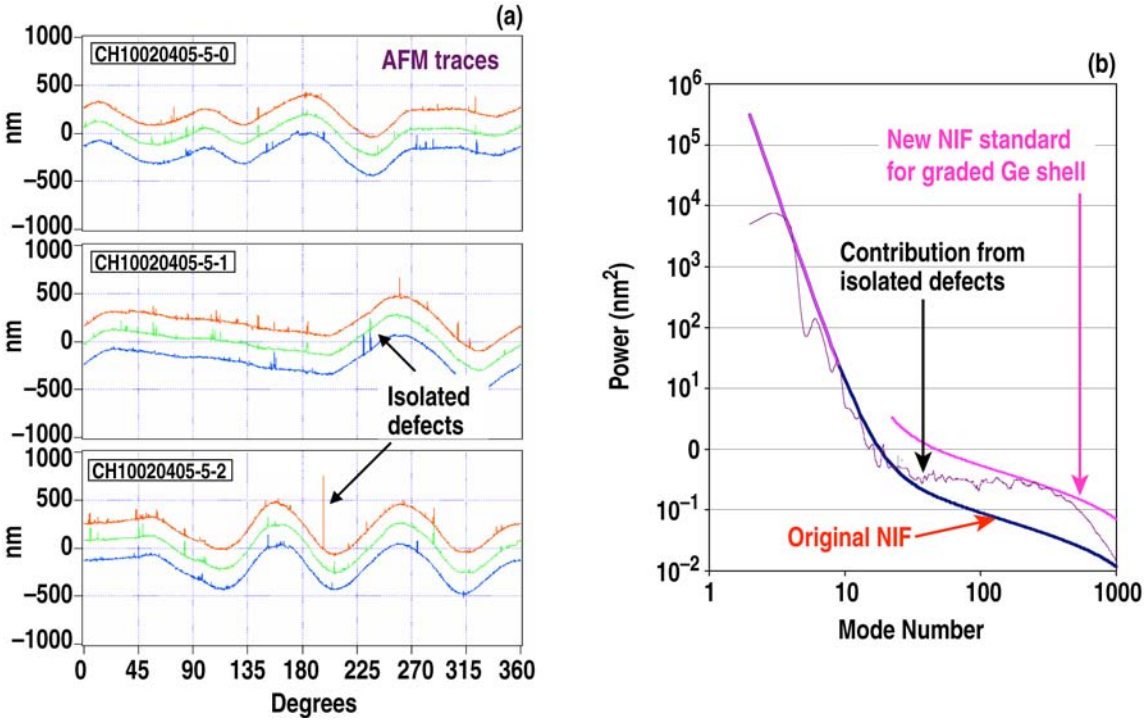

Fig. 3-76. (a) The AFM traces of graded shell show good surface finish at 150 μm thickness and (b) the power spectrum of the graded Ge shell meets the new NIF surface standard.

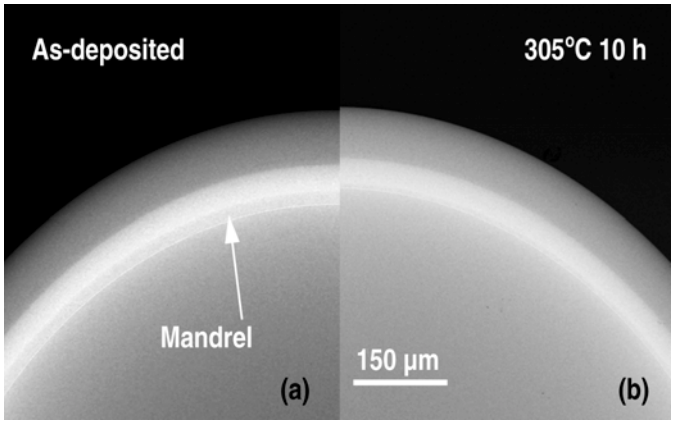

Fig. 3-77. Contact radiograph images show the mandrel has been removed at 305°C for 10 h.

Summary for Section 3.19

We have fabricated the graded Ge-doped CH shells. The shells have been characterized by a newly developed quantitative contact radiography technique, which allows us to measure precise thickness and Ge dopant concentrations nondestructively.

The graded shell meets nearly all the NIF design thickness and Ge concentration requirements and consists of four layers: an inner 10 μm, undoped GDP layer; a 48 μm, 0.83 at. % Ge-doped CH layer; a 10 μm, 0.38 at. % Ge-doped CH layer; and, finally, an outermost 90 μm layer of undoped CH. The mandrel has been successfully removed by pyrolysis. The power spectrum of the outer surface of the shell meets the new NIF surface standard. The smoothness of the inner surface was characterized by interferometry on pieces of fractured shells. The root-mean-square surface roughness sampling over two 60 by 46 μm areas range from 1.1 to 6.5 nm (305°C, 20 h). The remaining issues are elimination of isolated defects and better in situ layer thickness control to minimize shell handling.

DEVELOPMENT AT SCHAFER

3.20. OVERVIEW OF SHAFER TARGET FABRICATION IN SUPPORT OF SANDIA NATIONAL LABORATORIES

D. Shroen — Schafer

The Target Fabrication group at Sandia is composed of Schafer employees working on site and Sandia National Laboratories. The DOE ICF contract funds the labor, Sandia funds the on-site equipment, materials, facility charges and other costs associated with being on-site. In FY05 Sandia also transferred funding to the task ($350k) to fund additional effort. The responsibilities of Target Fabrication group include characterization of incoming parts, specifying capsules and micromachined components from GA, producing low density foams, prototyping target assemblies, and final target assembly, characterization and documentation.

Target Fabrication support four main target types on Z (Fig. 3-78):

1. Double Pinch Hohlraum, this is composed of upper and lower wire arrays with a capsule suspended in a center secondary holhraum.
2. Equation of State (EOS), this is not a wire array at all but rather panels that can launch shock waves or flyer plates.
3. Fast Ignitor, this is a wire array that can study the ability z-pinch to compress a hemisphere containing deuterium.
4. Dynamic Hohlraum, also a wire array, with a foam containing a deuterium filled capsule in the center.

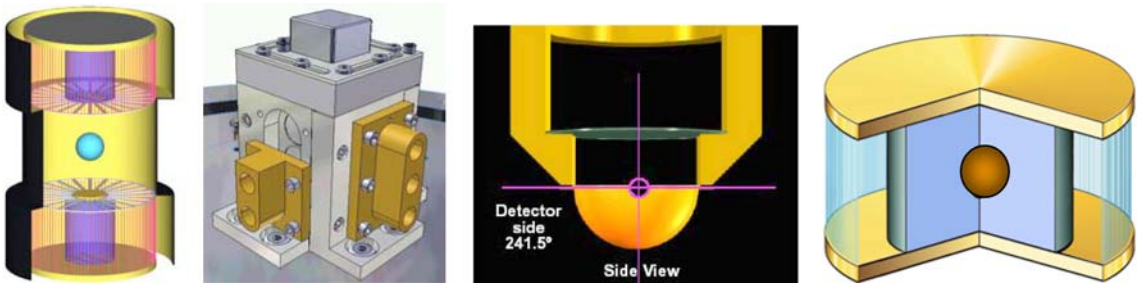

Fig. 3-78. These are graphic representations of the four target types. From left to right they are Double Pinch Hohlraum, EOS, Fast Ignitor, and Dynamic Hohlraum. Each target type has its own challenges, characterization and documentation.

Target Fabrication is expected to build targets in support of the Sandia Z machine at the rate of approximately one target a day. The typical schedule for fielding a target is as follows:

- At 14 weeks before the shot there is a shot kick-off meeting during which the experimenter outlines the design of the target and the machine parameters.
- At 10 weeks the mechanical drawings are released into fabrication.

- Target Fabrication receives assembly and characterization documentation through that time period and even up to the time of the shot. In fact, 34% of the information is given to Target Fab within 10 days before the shot.

The manner in which Target Fabrication receives its information is not clearly specified and typically varies with the personal style of the experimenter. We receive 34% of the required information within 10 days of the shot date. To track this information we have established a server based work order system. It allows all members of the workforce to review the current information from wherever they may be working.

The server based work order system is a key component of our ISO 9001 system. Our business system was certified ISO compliant in January of 2003. We chose to become ISO compliant for a very specific reason; the outstanding experimental results on Z needed target quality and documentation to dramatically improve. This improvement required a culture change and instituting a strict standard like ISO clearly signaled that change. There was one key concept that we especially liked — the need to demonstrate continual change. Of all the benefits of ISO, we saw the major benefit to be the workers' focus on ways of continually improving how they do their job.

Along with the other changes ISO brought to the workplace, we used it to standardize characterization and documentation. For a given experiment type, the characterization and documentation will be consistent. This makes comparison between experiments more direct and less confusing.

Each of the four types of targets continues to evolve. The Double Pinch Hohlraum has seen the size of the capsule grow and the use of specialized coated capsules. For example in 2003 the capsule was 3 mm in diameter and was held suspended in the secondary hohlraum by two submicron Formvar films glued to a single metal frame (Fig. 3-79). These initial experiments varied the length of the secondary to study the P2 defect of the capsule as it was compressed. By 2005 the capsules have grown to 5 mm (Fig. 3-79). This larger capsule caused significant wrinkling of the Formvar film when a single frame was used so we have gone to a two frame system. With the P2 defect better characterized the focus has sifted to the P4 defect. The capsules are coated in a precise manner that places the heaviest coating at the 45 deg latitude of the capsule. The experiment requires that the capsule placement and alignment are very exact to put this coating shim at exactly the point of the P4 defect.

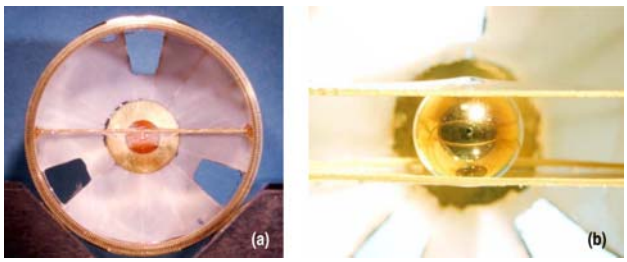

Fig. 3-79. (a) Double pinch targets from 2003 and (b) 2005. Note the small black dot indicating the north pole of a shimmed capsule.

An example of the Double Pinch QA report is shown in Fig. 3-80.

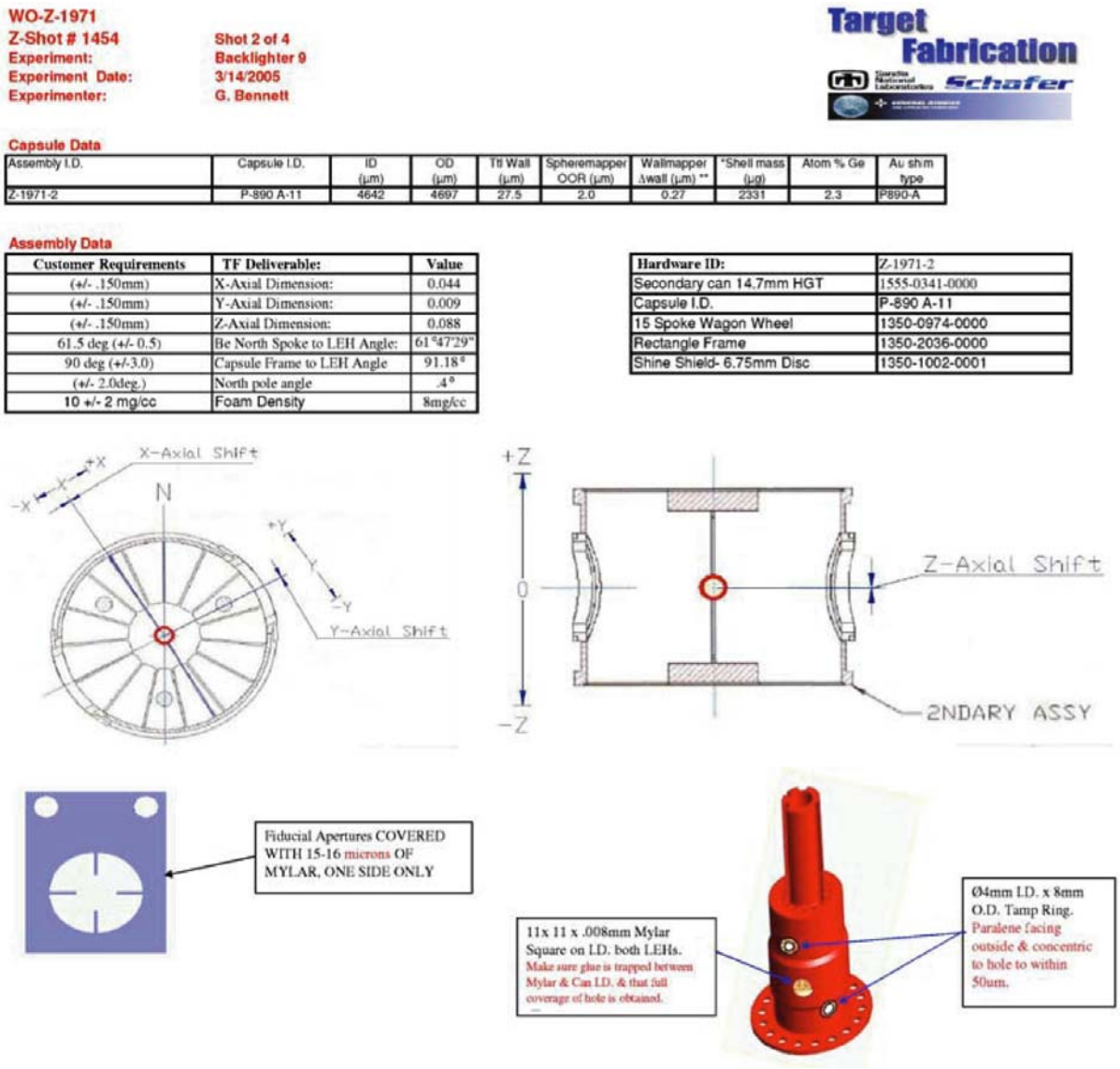

Fig. 3-80. First page of a QA report showing an overview of characterizations, tolerances and "as assembled" notes.

EOS targets can vary dramatically. Figure 3-81 shows two specific types of EOS experiments fielded on Z. They are designed to drive flyer plates or shockwaves into samples of known thickness. The samples can consist of metals, foams, hazardous samples (such as depleted uranium), and liquids. These samples can be either cryogenically cooled or preheated by localized heater assemblies. In these experiments Target Fabrication is responsible for characterizing the components of thickness and flatness, assembly of the target and characterizing the competed target. The documentation package of these experiments is very detailed and precise. An example is shown in Fig. 3-82.

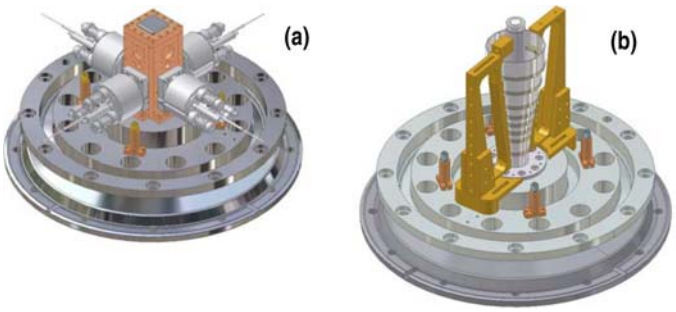

Fig. 3-81. Representations of two EOS experiments fielded on Z in 2005. The first has four heater assemblies; one on each of the four panels. The second was to study a conical shock.

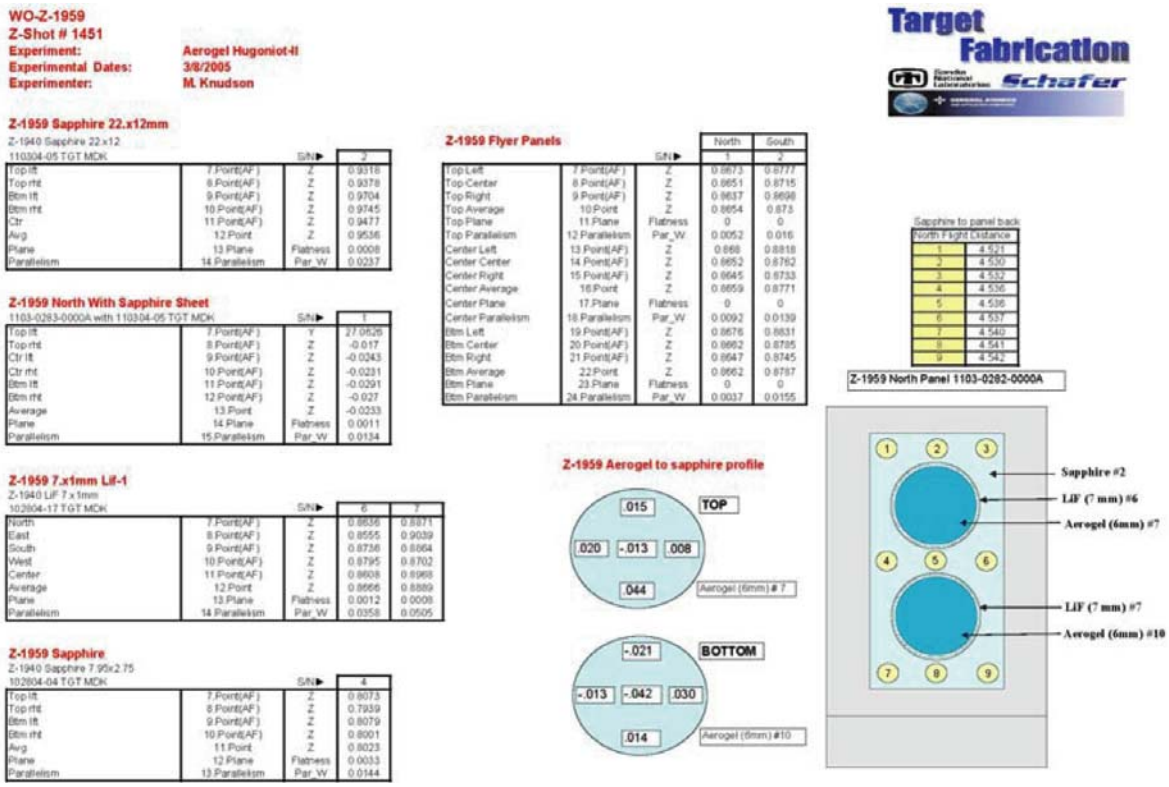

Fig. 3-82. First page of a QA report illustrating an overview of characterizations, tolerances and "as assembled" notes.

For fast ignitor targets, we attempted to build a very difficult double hemispherical design (Fig. 3-83). This design has an outer 2.7 mm o.d. hemisphere with a 2.4 mm o.d. inner hemisphere. The inner hemis os on 4.5 μm thick. Many hemispheres were made at General Atomics, leached by Target Fab and assembly attempted. None were successful so a backup target composed of just the ablator hemisphere was fielded.

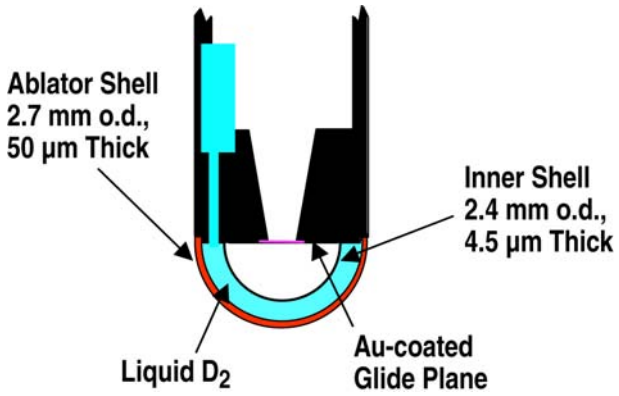

Fig. 3-83. A representation of the desired fast ignitor target which we are still attempting to make.

The Dynamic Hohlraum target is composed of the double wire array and a target foam containing a capsule (Fig. 3-84). In 2003 the foam was a simple cylinder and the capsule was a 1.7 mm o.d. with a 50 μm CH wall. In 2005 the foam could be shaped and the capsule could be a composite beryllium-polymer capsule.

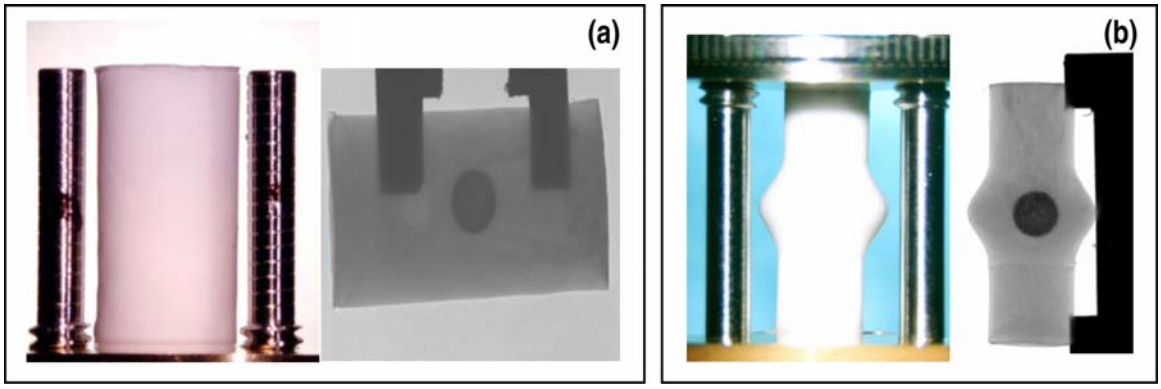

Fig. 3-84. (a) The foam and the radiograph are representative of the target type fielded in 2003. (b) The shaped foam and radiograph are from a target fielded in 2005.

The QA report for a Dynamic Hohlraum series focuses upon the capsule, its placement within the foam, the environmental exposure it has seen since removal from the pressure vessel and a MS characterization of the gas fill (Fig. 3-85).

Up to this point the targets shown have been made for Z, but target fabrication also makes targets for other drivers — most notably OMEGA. Examples of two OMEGA targets are shown in Fig. 3-86.

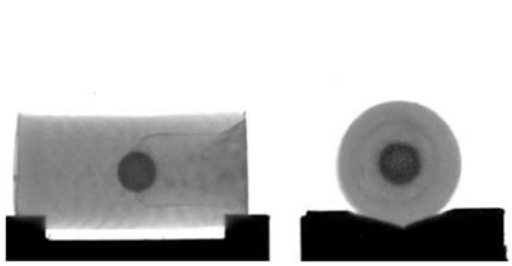

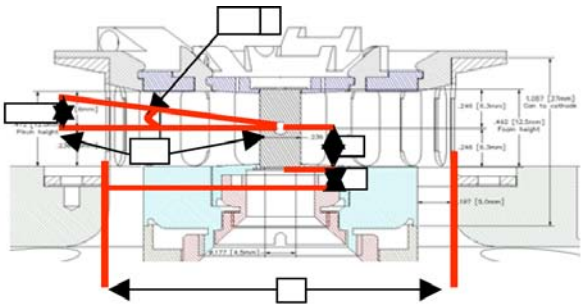

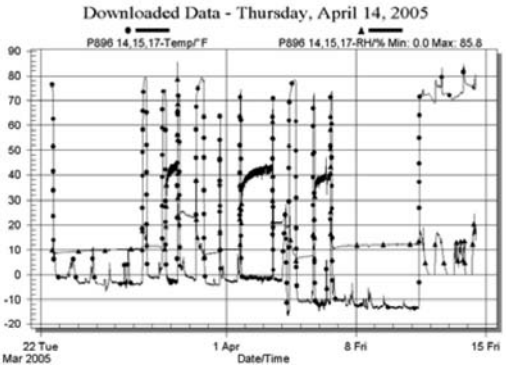

Table 2, Internal Gas Analysis of the ICF Capsules

Serial #	Units	HD	D_2 + HD	CO	N_2	Ar	CO_2	Xe	Total	Closure
P760-6	atm	0.093	21.2	--	--	0.068	--	--	21.59	98.7
	mol 10^{-7}	0.30	68.0	--	--	0.22	--	--		
P761-01R	atm	0.173	26.51	0.004	0.013	0.067	0.002	0	26.74	99.8
	mol 10^{-7}	0.264	40.42	0.006	0.020	0.10	0.003	0		
P761-10	atm	0.160	24.72	0.004	0.017	0.073	0.049	0	24.79	100.6
	mol 10^{-7}	0.240	37.11	0.006	0.026	0.11	0.074	0		

Fig. 3-85. A portion of a QA report for a dynamic hohlraum series. It shows radiographs of the capsule that were used to determine the exact capsule placement, the diagnostic markings on the can to allow precise alignments, the output showing the temperature and relative humidity the capsule experienced and the gas analysis of a witness capsule.

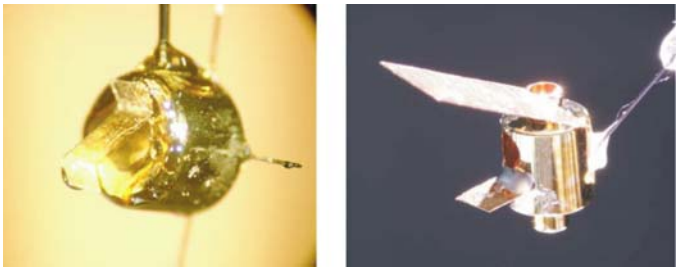

Fig. 3-86. OMEGA targets.

A key specification of an OMEGA target is the angles. To allow us to simultaneously build and characterize we have engineered a dual theta target assembly station (Fig. 3-87). The station has two digital cameras that are fixed in relationship to each other to create a defined three-dimensional space. It also has two stages that allow for rotational as well as linear motion. Furthermore, it has programmable controllers that allow for sample rotation to the desired orientation or chamber view. Furthermore the system has the ability to compare a CAD drawing to the "as built" condition for QA documentation.

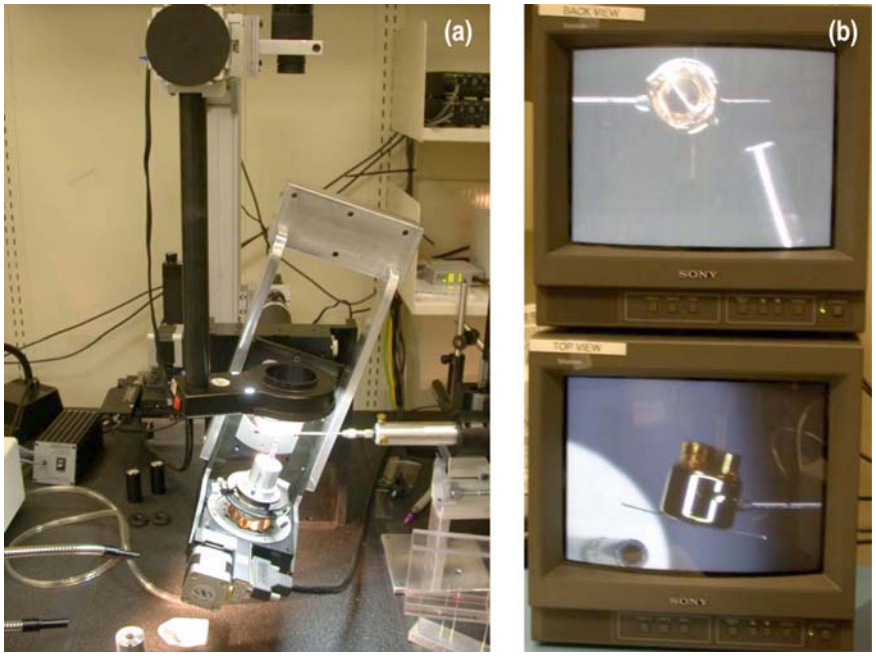

Fig. 3-87. (a) The stage portion of the dual theta assembly station. (b) Output from the two orthogonal cameras.

3.21. PLANAR TARGETS FOR NRL NIKE LASER

Keith Shillito — Schafer

The Nike Laser at the NRL is designed only for experiments using planar targets, which are ideal for exploring material properties, hydrodynamic instabilities, and laser-target material interactions. The laser's beam is very uniform and well characterized so experimenters can explore the effects of depositing a large amount of energy in a material without perturbations from anomalies in the laser beam. For experiments to have meaningful results, the quality of the targets must at least equal the uniformity of the beam and exceed the limits of the diagnostic equipment. Over the years, as diagnostic equipment and prediction codes have improved, the requirements for target surface finish, uniformity, flatness, and purity have increased. Additionally, the complexity of target designs has the foil on a patterned substrate. Machining works well for patterns with PV greater than 1 μm. For patterns with increased by the addition of material layers, dopants, intentional surface and mass perturbations, and foams. NRL has also developed a cryogenic capability requiring targets that are designed to work in the wall of a cryogenic Dewar.

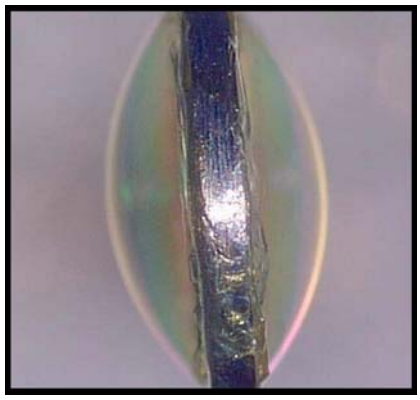

Fig. 3-88. Polyimide gas bag target.

We had the opportunity to develop a gas bag target during mid-year as this was a new request from NRL. There was only one previous fabricator of this type target in the USA, that being Luxel, Inc. Through a quick and intense effort Schafer was able to essentially reproduce the "Luxel type" gas bag target used often at LLNL and LLE.

We developed and delivered several polyimide film gas bag targets with 0.3 μm window thickness on both sides of an aluminum washer that was capable of holding 20 psi gas pressure (Fig. 3-88).

Fig. 3-89. Polyimide/gold sandwich films.

We also delivered some polyimide with gold coatings sandwich films as depicted in Fig. 3-89. These are made of alternating layers of polyimide film and sputtered gold (ten layers of each, total thickness of film is 1.5 μm. Film is being stretched over a CTM.)

The number of EOS targets decreased during 2005, while there was an increased emphasis on foam, coated targets, and patterned targets.

A large portion of the films we delivered had a sine wave pattern on one surface. These films are made by machining the pattern directly into the foil or by casting PV less than 1

μm, casting on an etched or machined mold usually gives better results. We have added a new technique to our characterization suite. By measuring the surface of the casting or mold with our Ambios stylus profilometer, we can analyze the pattern and tell if it is a pure sine wave or if it contains overtones. We started using this type of analysis because some of our Gentec molds deviated significantly from a true sine. We calculated the effect of stylus radius on the sine wave analysis and found it to be negligible for the 25 μm stylus we normally use. We have attempted to clean Gentec molds using the semiconductor industry standard RCA Cleaning Method with mixed results and have searched for better means of producing casting substrates. This has led to the determination via demonstrations that a state of the art Precitech diamond turning lathe is capable of producing the desired casting substrates with the requisite sine wave patterns.

Foam target components have become a high interest target at NRL and we responded by emphasizing attention to RF and DVB foam systems. The primary ICF target design for NRL includes low-density foam. Additionally we have the capability to make CRF, TPX, polystyrene foam, and other foam systems in Livermore. Different foam systems range in densities from 3 to 850 mg/cc and pore sizes from nanometers to 15 μm. During the past year we have continued to produce composite RF foam/polystyrene targets with a machined sine wave at the interface between the two materials. We have also produced doped foams using various doping techniques. Dopants have been added as physical dispersions by mixing small amounts of nanopowders uniformly throughout the foam. We have also doped foam systems using chemical modifications. Chemically doped monomers, polymers modified by chemical vapor deposition, or dissolved organometallics in the solvent system are all examples of doping by chemical modification. Foams with graded dopant concentrations have been produced by building the foam layer by layer with changing dopant concentrations in each layer. Work must still be done to learn how to properly characterize foam density uniformity, cell size uniformity, surface finish, and dopant concentration and profile. We actually were able to fabricate a resorcinol formaldehyde (RF) foam with a sinewave machined in the surface (Fig. 3-90) with a thickness of 285 μm and density of 313 mg/cc.

Fig. 3-90. RF foam with machined sinewave.

Precise target specifications are critical to the success of ICF experiments just as characterizing the targets precisely is critical to our fabrication success. In 2004 we assesed our characterization equipment to our capabilities and implemented use of the Filmmetrics film mapper (Fig. 3-91), a Nikon NexIV automated measure scope (Fig. 3-92), and an Ambios stylus profiler (Fig. 3-93). These instruments have greatly improved our characterization accuracy and speed during 2005. A new assembly station/characterization station, the Dual Theta, copied from the one at SNL was purchased for deliverey in fall 2005 and will be deployed during GFY06 (Fig. 3-94).

Fig. 3-91. Filmetric film mapper.

Fig. 3-92. NexIV automated measure scope.

Fig. 3-93. Ambios stylus surface profiler.

Fig. 3-94. Dual theta assembly/characterization station.

REFERENCES FOR SECTION 3

[3-1] M.A. Salazar, P. Gobby, and R. Watt, "Pressure Testing of Micro Balloons by Bursting," Fusion Technol. **38**, 136 (2000).

[3-2] R. Gram, UR/LLE measurements.

[3-3] R. Cook, "Production of Hollow Microspheres for Inertial Confinement Fusion Experiments," Proc. Symp. Materials Research Society **372**, 101 (1995).

[3-4] A. Nikroo and D.A. Steinman, "Thin Sputtered Glass as a Permeation Barrier for Plasma Polymer Shells," Fusion Technol. **35**, 212 (1999).

[3-5] J.S. Jaquez, E.L. Alfonso, and A. Nikroo, "Development of Sputtered Coated Glass Permeation Barrier," 16th Target Fabrication Specialists Meeting, May 1-5, 2005, Scottsdale, Arizona, to be published in Fusion Sci. Technol. (2005).

[3-6] A. Nikroo and D. Woodhouse, "Bounce Coating Induced Domes on Glow Discharge Polymer Coated Shells," Fusion Technol. **35**, 202 (1999).

[3-7] R.C. Cook, R. McEachern, R.B. Stephens, "Representative Surface Profile Power Spectra from Capsules Used in Nova and Omega Implosion Experiments," Fusion Technol. **35**, 224 (1999).

[3-8] R.B. Stephens, S.W. Hann, D.C. Wilson, "Characterization Specifications for Baseline Indirect Drive NIF Targets," General Atomics Report GA-A23749, April 2002.

[3-9] S.W. Haan, P.A. Amendt, T.R. Dittrich, S.P. Hatchett, M.C. Herrmann, O.A. Hurricane, M.M. Marinak, D. Munro, S.M. Pollaine, G.A. Strobel, L.J. Suter, "Update on NIF Indirect Drive Ignition Target Fabrication Specifications," Fusion Sci. Technol. **45**, 69-73 (2004).

[3-10] R.B. Stephens, D. Olson, H. Huang, J.B. Gibson, "Complete Surface Mapping of ICF Shells," Fusion Sci. Technol. **45**, 210-213 (2004).

[3-11] P. Subramanian, A. Zebib, B. McQuillan, "Solutocapillary Convection in Spherical Shells," Phys. Fluids **17**, 017103 (2005).

[3-12] B.W. McQuillan, M. Takagi, "Removal of Mode 10 Surface Ripples in ICF PAMS Shells," Fusion Sci. Technol. **41**, 209-213 (2002).

[3-13] R.B. Stephens, "Precision Shell Characterization Using Radial Averaging of X-Ray Images," J. Vac. Sci. Technol. A **13**(3), 979-982 (1995).

[3-14] D. Bernat, R.B. Stephens, "Algorithm for Better X-radiography Analysis," Fusion Technol. **31**, 473-476 (1997).

[3-15] PD-1000 Non-contact Micrometer, with an accuracy of 10 nm over 4 mm working range from Precision-Dynamics Inc., 1155 Appleby Line, Unit E8, Burlington, Ontario Canada L7L 5H9, www.predynamics.com.

[3-16] MM-11 measurescope platform with a 5 times Michelson interference objective.

[3-17] T.M. Henderson et al., "Microradiographic Characterization of Laser Fusion Pellets," Rev. Sci. Instrum. **48**, 835-840 (1977).

[3-18] T.G. Cunningham et al., "The Application of X-ray Microscopy in Materials Science," J. Microscopy **144**, 261 (1986).

[3-19] H.-G. Kim et al., "X-ray Microscopy of Inertial Fusion Targets Using a Laser-Produced Plasma as an X-ray Source," J. Vac. Sci. Technol. A **5**, 2781 (1987).

[3-20] R.B. Stephens, "Precision Shell Characterization Using Radial Averaging of X-ray Images – Part II," in Hollow and Solid Spheres and Microspheres: Science and Technology Associated with their Fabrication and Application, Proc. Symposium Materials Research Society, Vol. 372 (MRS, Boston, 1995), p. 203.

[3-21] R.B. Stephens, "Precision Shell Characterization Using Radial Averaging of X-ray Images," J. Vac. Sci. Technol. A **13**, 979 (1995).

[3-22] R.B. Stephens and D. Bernat, "Algorithm for Better X-radiography Analyses," Fusion Technol. **31**, 473-476 (1997).

[3-23] R.R. Stone, D.W. Gregg, and P.C. Souers, "Nondestructive Inspection of Transparent Microtargets for Laser Fusion," J. Appl. Phys. **46**, 2693 (1975).

[3-24] B.W. Weinstein, "White-Light Interferometric Measurement of the Wall Thickness of Hollow Glass Microspheres," J. Appl. Phys. **46**, 5305 (1975).

[3-25] B.W. Weinstein and C.D. Hendricks, "Interferometric Measurement of Laser Fusion Targets," Appl. Opt. **17**, 3641 (1978).

[3-26] T.F. Powers, "Improved Nonconcentricity Characterization of Transparent Laser Fusion Targets by Interferometry," J. Vac. Sci. Technol. **20**, 1355 (1982).

[3-27] H.-J. Kong, M.D. Wittman, H.-G. Kim, "New Shearing Interferometer for Real-Time Characterization of Cryogenic Laser Fusion Targets," Appl. Phys. Lett. **55**, 2274-2276 (1989).

[3-28] C.K. Immesoete et al., "Computer Assisted Microballoon Selection for Inertial Confinement Fusion Targets," J. Vac. Sci. Technol. A **8**, 3324 (1990).

[3-29] PD-1000 Non-contact Micrometer, with an accuracy of 10 nm over 4 mm working range from Precision-Dynamics Inc., 1155 Appleby Line, Unit E8, Burlington, Ontario Canada L7L 5H9, www.predynamics.com.

[3-30] Nikon MM-11 measurescope platform with a 5 times Michaelson interference objective.

[3-31] P. Pavliçek and J. Soubusta, "Measurement of the Influence of Dispersion on White-Light Interferometry," Appl. Opt. **43**, 766 (2004).

[3-32] E. Ingelstam and L.P. Johansson, "Correction Due to Aperture in Transmission Interference Microscopes, J. Sci. Inst. **35**, 15 (1958).

[3-33] R.B. Stephens and M. Wittman, "Laser Fusion Target Shell Wall Thickness from Interference Fringe Shape Analysis," J. Vac. Sci. Technol. A **12**, 1302 (1994).

[3-34] R.B. Stephens, T. Mroczskowski, and J. Gibson, "Seeing Shell Wall Fluctuations," Fusion Technol. **38**, 132-135 (2000).

[3-35] S. Skupsky, R. Betti, T.J.B. Collins, V.N. Goncharov, J.A. Marozas, P.W. McKenty, P.B. Radha, T.R. Boehly, J.P. Knauer, F.J. Marshall, D.R. Harding, J.D. Kilkenny, D.D. Meyerhofer, T.C. Sangster, R.L. McCrory, "Advance Direct-Drive Target Designs for NIF," 3rd Int. Conf. on Inertial Fusion Sciences and Applications, September 7–12, 2003, Monterey, California, in Inertial Fusion Sciences and Applications 2003, eds. B.A. Hammel, D.D. Meyerhofer, J. Meyer-ter-Vehn, and H. Azechi (American Nuclear Society, 2004) pp. 61-64.

[3-36] S.M. Lambert, G.E. Overturf, III, G. Wilemski, S.A. Letts, D. Schroen-Carey, R.C. Cook, "Fabrication of Low-Density Foam Shells from Resorcinol-Formaldehyde Aerogel," J. Appl. Polymer Sci. **65**, 211 (1997).

[3-37] A. Nikroo, D. Czechowicz, R. Paguio, A.L. Greenwood, M. Takagi, "Fabrication and Properties of Overcoated Resorcinol-Formaldehyde Shells for OMEGA Experiments." Fusion Sci. Technol. **45**, 84 (2004).

[3-38] D.D. Meyerhofer et al., "Inovative Target Designs for Direct-Drive Ignition," 16th Target Fabrication Specialists Meeting, May 1-5, 2005, Scottsdale, Arizona, to be published in Fusion Sci. Technol. (2005).

[3-39] D.R. Harding, M.D. Wittman, L.M. Elasky, S. Verbridge, L.D. Lund, D. Jacobs-Perkins, W. Seka, D.H. Edgell, D.D. Meyerhofer, "OMEGA Direct-Drive Cryogenic Deuterium Targets," presented at the 46th Annual Meeting of the Division of Plasma Physics of the American Physical Society, Mini-Conference on ICF and HEDP Target Fabrication, November 15-16, 2004, Savannah, Georgia.

[3-40] S.W. Haan et al., "Design and Modeling of Ignition Targets for the National Ignition Facility," Phys. Plasmas **2**, 2480 (1995).

[3-41] R.A. Sacks and D.H. Darling, "Direct Drive Cryogenic ICF Capsules Employing D-T Wetted Foam," Nucl. Fusion **27**, 447 (1987).

[3-42] A. Nikroo et al., "Fabrication and Properties of Overcoated Resorcinol-Formaldehyde Shells for OMEGA Experiments," Fusion Sci. Technol. **45**, 84 (2004).

[3-43] D.W. Schafer et al., "Origin of Porosity in Resorcinol-Formaldehyde Aerogels," J. Non-Cryst. Solids **186**, 159 (1995).

[3-44] L.M. Hair et al., "Low-Density Resorcinol-Formaldehyde Aerogels for Direct-Drive Laser Inertial Confinement Fusion Targets," J. Vac. Sci. Technol. A **6** (4) (1988).

[3-45] M. Takagi et al., "Development of Deuterated Polystyrene Shell for Laser by Means of a Matched Emulsion Method," The Soc. of Polymer Sci., Japan, J. Polymer **48**, 41-45 (1991).

[3-46] S.M. Lambert et al., "Fabrication of Low-Density Foam Shells from Resorcinol-Formaldehyde Aerogel." J. Appl. Polm. Sci. **65**, 2111-2122 (1997).

[3-47] S. Skupsky, R. Betti, T.J.B. Collins, V.N. Goncharov, J.A. Marozas, P.W. McKenty, P.B. Radha, T.R. Boehly, J.P. Knauer, F.J. Marshall, D.R. Harding, J.D. Kilkenny, D.D. Meyerhofer, T.C. Sangster, R.L. McCrory, "Advance Direct-Drive Target Designs for NIF," 3rd Int. Conf. on Inertial Fusion Sciences and Applications, September 7–12, 2003, Monterey, California, in Inertial Fusion Sciences and Applications 2003, eds. B.A. Hammel, D.D. Meyerhofer, J. Meyer-ter-Vehn, and H. Azechi (American Nuclear Society, 2004) pp. 61-64.

[3-48] A. Nikroo, D. Czechowicz, R. Paguio, A.L. Greenwood, M. Takagi, "Fabrication and Properties of Overcoated Resorcinol-Formaldehyde Shells for OMEGA Experiments," Fusion Sci. Technol. **45**, 84 (2004).

[3-49] D.D. Meyerhofer et al., "Inovative Target Designs for Direct-Drive Ignition," 16th Target Fabrication Specialists Meeting, May 1-5, 2005, Scottsdale, Arizona, to be published in Fusion Sci. Technol. (2005).

[3-50] D.R. Harding, M.D. Wittman, L.M. Elasky, S. Verbridge, L.D. Lund, D. Jacobs-Perkins, W. Seka, D.H. Edgell, D.D. Meyerhofer, "OMEGA Direct-Drive Cryogenic Deuterium Targets," presented at the 46th Annual Meeting of the Division of Plasma Physics of the American Physical Society, Mini-Conference on ICF and HEDP Target Fabrication, November 15-16, 2004, Savannah, Georgia.

[3-51] J. Streit, D. Schroen, "Development of Divinylbenzene Foam Shells for Use as Inertial Fusion Energy Reactor Targets," Fusion Sci. Technol. **43**, 321 (2003).

[3-52] M. Takagi, R. Cook, B.W. McQuillan, F.H. Elsner, R.B. Stephens, A. Nikroo, J. Gibson, S. Paguio, "Development of High Quality Poly(α-Methylstyrene) Mandrel for NIF," Fusion Sci. Technol. **41**, 278 (2002).

[3-53] B.W. McQuillan, A. Nikroo, D.A. Steinman, F.H. Elsner, D.G. Czechowicz, M.L. Hoppe, M. Sixtus, W.J. Miller, "The PAMS/GDP Process for Production of ICF Target Mandrels," Fusion Sci. Technol. **31**, 281 (1997).

[3-54] S.M. Lambert, G.E. Overturf, III, G. Wilemski, S.A. Letts, D. Schroen-Carey, R.C. Cook, "Fabrication of Low-Density Foam Shells from Resorcinol-Formaldehyde Aerogel," J. Appl. Polymer Sci. **65**, 211 (1997).

[3-55] G.E. Overturf, III, R. Cook, S.A. Letts, S.R. Buckley, M.R. McClellan, D. Schroen-Carey, "Resorcinol/Formaldehyde Foam Shell Targets for ICF," Fusion Technol. **28**, 1803 (1995).

[3-56] D. Schroen-Carey, G.E. Overturf, III, R. Reibold, S.R. Buckley, S.A. Letts, R. Cook, "Hollow Foam Microshells for Liquid-Layered Cryogenic Inertial Confinement Fusion Targets," J. Vac. Sci. Technol. A **13**, 2564 (1995).

[3-57] "Foam Shell Development and Production: Overcoating Process," Final Report, Task 95-068.

[3-58] J.E. Streit, Schafer Corporation, SNL, Albuquerque, New Mexico, private communication, 2004.

[3-59] A. Nikroo, J.M. Pontelandolfo, "Fabrication of Thin Walled Glow Discharge Polymer Shells," Fusion Technol. **38**, 58 (2000).

[3-60] M. Takagi, M. Ishihara, T. Norimatsu, T. Yamanaka, Y. Izawa, S. Nakai, "Development of Foam Shell with Plastic Ablator for Cryogenic Laser Fusion Target," J. Vac. Sci. Technol. A **11**, 2837 (1993).

[3-61] K.B. Fournier, C. Constantin, J. Poco, M.C. Miller, C.A. Back, L.J. Suter, J. Satcher, J. Davis, and J. Grun, "Efficient Multi-keV X-Ray Sources from Ti-Doped Aerogel Targets," Phys. Rev. Lett. **92**, 165005 (2004).

[3-62] A. Nikroo, D. Czechowicz, R.R. Paguio, A.L. Greenwood, and M. Takagi, "Fabrication and Properties of Overcoated Resorcinol-Formaldehyde Shells for OMEGA Experiments," Fusion Sci. Technol. **45**, 84 (2004).

[3-63] C.A. Back, J.D. Bauer, J.H. Hammer, B.F. Lasinski, R.E. Turner, P.W. Rambo, O.L. Landen, L.J. Suter, M.D. Rosen, and W.W. Hsing, "Diffusive, Supersonic X-Ray Transport in Radiatively Heated Foam Cylinders," Phys. Plasmas **7**, 2126 (2000).

[3-64] Q. Gu, K. Nagai, T. Norimatsu, S. Fujioka, H. Nishimura, K. Nishihara, N. Miyanaga, and Y. Izawa "Preparation of Low-Density Macrocellular Tin Dioxide Foam with Variable Window Size," Chem. Mater. **17**, 1115 (2005).

[3-65] C.J. Brinker and G.W. Scherer, Sol-Gel Science (Academic Press, San Diego, 1990) p. 116.

[3-66] N.K. Kim, K. Kim, D.A. Payne, and R.S. Upadhye, "Fabrication of Hollow Silica Spheres by a Droplet Generation Method and Sol-Gel Processing," J. Vac. Sci. Technol. A **7**, 1181 (1989).

[3-67] S.M. Lambert, G.E. Overturf, III, G. Wilemski, S.A. Letts, D. Schroen-Carey, and R.C. Cook, "Fabrication of Low-Density Foam Shells from Resorcinol-Formaldehyde Aerogel," J. Appl. Polym. Sci. **65**, 2111 (1997).

[3-68] M.W. Droege, P.R. Coronado, and L.M. Hair, "Method for Making Monolithic Metal Oxide Aerogels," US Patent 5,395,805 (1995).

[3-69] S. Wang and N. Wu, "Tin Oxide Gel Shrinkage During CO_2 Supercritical Drying" J. Non-Cryst. Solids **224**, 259 (1998).

[3-70] J.F. Poco, P.R. Coronado, R.W. Pekala, and L.W. Hrubesh, "A Rapid Supercritical Extraction Process for the Production of Silica Aerogels," Proc. Symp. Materials Research Society, Vol. 431 (MRS, Boston, 1996), p. 297.

[3-71] J.F. Hund, M.F. Bertino, G. Zhang, C. Sotiriou-Leventis, N. Leventis, A.T. Tokuhiro, and J. Farmer, "Formation and Entrapment of Noble Metal Clusters in Silica Aerogel Monoliths by γ-Radiolysis," J. Phys. Chem. B **107**, 465 (2003).

[3-72] J.F. Hund, M.F. Bertino, G. Zhang, C. Sotiriou-Leventis, and N. Leventis, "Synthesis of Homogeneous Alloy Metal Clusters In Silica Aerogels," J. Non-cryst. Solids **350**, 9 (2004).

[3-73] C.A. Morris, M.L. Anderson, R.M. Stroud, C.I. Merzbacher, and D.R. Rolison, "Silica SOL as a Nanoglue: Flexible Synthesis of Composite Aerogels," Science **284**, 622 (1999).

[3-74] M.S. Tillack, private communication.

[3-75] J.F. Ziegler and J.P. Biersack, "SRIM-2003: The Stopping and Range of Ions in Solids," version 2003.26.

[3-76] Y. Aglitskiy, A.L. Velikovich, M. Karasik, V. Serlin, C.J. Pawley, A.J. Schmitt, S.P. Obenschain, A.N. Mostovych, J.H. Gardner, N. Metzler, "Direct Observation of Mass Oscillations Due to Ablative Richtmyer-Meshkov Instability in Plastic Targets," Phys. Rev. Lett. **87**, 265002, (2001).

[3-77] Y. Aglitskiy, A.L. Velikovich, M. Karasik, V. Serlin, C.J. Pawley, A.J. Schmitt, S.P. Obenschain, A.N. Mostovych, J.H. Gardner, N. Metzler, "Direct Observation of Mass Oscillations Due to Ablative Richtmyer-Meshkov Instability and Feedout in Planar Plastic Targets," Phys. Plasmas **9**, 2264 (2002).

[3-78] S.P. Obenschain, D.G. Colombant, M. Karasik, C.J. Pawley, V. Serlin, A.J. Schmitt, J.L. Weaver, J.H. Gardner, L. Phillips, Y. Aglitskiy, Y. Chan, J.P. Dahlburg, M. Klapisch, "Effects of Thin High-Z Layers on the Hydrodynamics of Laser-Accerlerated Plastic Targets," Phys. Plasmas **9**, 2234 (2002).

[3-79] N. Metzler, A.L. Velikovich, A.J. Schmitt, M. Karasik, V. Serlin, A.N. Mostovych, S.P. Obenschain, J.H. Gardner, Y. Aglitskiy, "Laser Imprint Reduction with a Shaping Pulse, Oscillatory Richtmyer-Meshkov to Rayleigh-Taylor Transition and Other Coherent Effects in Plastic-Foam Targets," Phys. Plasmas **10**, 1897 (2003).

[3-80] T. Walsh, Schafer Corp., Livermore, California, private communication, 2005.

[3-81] A. Nikroo, D. Czechowicz, R. Paguio, A.L. Greenwood, M. Takagi, "Fabrication and Properties of Overcoated Resorcinol-Formaldehyde Shells for OMEGA Experiments," Fusion Sci. Technol. **45**, 84 (2004).

[3-82] D.C. Wilson, P.A. Bradley, N.M. Hoffman, F.J. Swenson, D.P. Smitherman, R.E. Chrien, R.W. Margevicius, D.J. Thoma, L.R. Roreman, J.K. Hoffer, S.R. Goldman, S.E. Caldwell, T.R. Dittrich, S.W. Haan, M.M. Marinak, S.M. Pollaine, and J.J. Sanchez, "The Development and Advantages of Beryllium Capsules for the National Ignition Facility," Phys. Plasmas **5**, 1953 (1998).

[3-83] R.J. Burt, S.F. Meyer, and E.J. Hsieh, "Radio Frequency Magnetron Sputtering of Thick Film Amorphous Beryllium," J. Vac. Sci. Technol. **17**, 407 (1980).

[3-84] E.J. Hsieh, C.W. Price, E.L. Pierce, and R.G. Wirtenson, J. Vac. Sci. Technol. A **8**, 2165 (1990).

[3-85] R. McEachern, C. Alford, R. Cook, D. Makowcki, and R. Wallace, "Sputter-Deposited Be Ablators for NIF Target Capsules," Fusion Technol. **31**, 435 (1997).

[3-86] R. McEachern and C. Alford, "Evaluation of Boron-Doped Beryllium as an Ablator for NIF Target Capsules," Fusion Technol. **35**, 115 (1999).

[3-87] J.A. Thornton, "The Microstructure of Sputter-Deposited Coatings," J. Vac. Sci. Technol. A **4**, 3059 (1986).

[3-88] A.E. Lita and J.E. Sanchez, Jr., "Characterization of Surface Structure in Sputtered Al Films: Correlation to Microstructure Evolution," J. Applied Phys. **85**, 876 (1999).

[3-89] P. Meakin, "Ballistic Deposition onto Inclined Surfaces," Phys. Rev. A **38**, 994 (1988).

[3-90] J. Yu and J.G. Amar, "Dynamical Scaling Behavior in Two Dimensional Ballistic Deposition with Shadowing," Phys. Rev. E **66**, 21603 (2002).

[3-91] S.W. Haan et al., "Design and Simulations of Indirect Drive Ignition Targets for NIF," Nucl. Fusion **44**, S171 (2004).

[3-92] S.W. Haan, LLNL, private communication.

[3-93] A.A. Tseng, J. Microcech. Microeng. **14**, R15 (2004).

[3-94] L.A. Giannuzzi and F.A. Stevie, "A Review of Focused Ion Beam Milling Techniques for TEM Specimen Preparation," Micron **30**, 197 (1999).

[3-95] S.T. Picraux, "Ion Implantation in Metals," Ann. Rev. Mater. Sci. **14**, 335 (1984).

[3-96] J. Taniguchi, N. Ohno, S. Takeda, I. Miyamoto, and M. Komuro, "Focused-Ion-Beam Assisted Etching of Diamond in X_eF_2," J. Vac. Sci. Technol. B **16**, 2506 (1998).

[3-97] D.M. Thaus, T.J. Stark, D.P. Griffis, and P.E. Russell, "Developed of Focused In-Beam Machining Techniques for Permalloy Structures," J. Vac. Sci. Technol. B **14**, 3928 (1996).

[3-98] J.C. Gonzalez, D.P. Griffis, T.T. Miau, and P.E. Russell, "Chemically Enhanced Focused Ion Beam Micromachining of Copper," J. Vac. Sci. Technol. B **19**, 2539 (2001).

[3-99] D.W. Hill, E. Castillo, K.C. Chen, S.E. Grant, A.L. Greenwood, J.L. Kaae, A. Nikroo, S.P. Paguio, C. Shearer, J.N. Smith, Jr., D.A. Stephens, D.A. Steinman, J. Wall, "Fabrication and Characterization of Fast Ignition Targets," Fusion Sci. Technol. **45**, 113 (2004).

[3-100] A. Nikroo, F.H. Elsner, D.G. Czechowicz, S.E. Grant, A.L. Greenwood, M.L. Hoppe, B.W. McQuillan, W.J. Miller, D.A. Pontelandolfo, D.A. Steinman, R.B. Stephens, K.R. Schultz, M. Takagi, "Capsule Production and Development for ICF Experiments," Proc. 1st Intl. Conf. on Inertial Fusion Sciences and Applications, September 12–17, 1999, Bordeaux, France (Elsevier, 2001).

[3-101] Modern Electroplating, edited by Frederick A. Lowenheim (John Wiley & Sons, New York, 1963).

[3-102] T.J. Orzechowski, M.D. Rosen, H.N. Kornblum, L.J. Suter, A.R. Thiessen, R.J. Wallace, and L.J. Porter, Phys. Rev. Lett. **77**, 3545 (1996).

[3-103] Mordy Rosen, LLNL, private communication.

[3-104] M. Ohring, The Materials Science of Thin Films (Academic Press: San Diego, 1992).

[3-105] D.W. Hoffman and J.A. Thornton, Thin Solid Films **40**, 355 (1977).

[3-106] T.J. Orzechowski, M.D. Rosen, H.N. Kornblum, L.J. Suter, A.R. Thiessen, R.J. Wallace, and L.J. Porter, Phys. Rev. Lett. **77**, 3545 (1996).

[3-107] M.L. Roberts, P.G. Grant, G.S. Bench, T.A. Brown, B.R. Frantz, D.H. Morse, and A.J. Antolak, Nucl. Instrum. Methods B **158**, 24 (1999).

[3-108] G.A. Graham, P.G. Grant, R.J. Chater, A.J. Westphal, A.T. Kearsley, C. Snead, G. Domínguez, A.L. Butterworth, D.S. McPhail, G. Bench, and J.P. Bradley, Meteoritics & Planetary Science **39**, 1461 (2004).

[3-109] A. Nikroo and D. A. Steinman, "Thin Sputtered Glass as a Permeation Barrier for Plasma Polymer Shells," Fusion Technol. **35**, 212 (1999).

[3-110] E.L. Alfonso, J.S. Jaquez, and A. Nikroo, "Using Mass Spectrometry to Characterize Permeation Half-Life of ICF Targets," see Section 3.1 (this report).

[3-111] B.W. McQuillan, A. Nikroo, D.A. Steinman, F.H. Elsner, D.G. Czechowicz, M.L. Hoppe, M. Sixtus, W.J. Miller, "The PAMS/GDP Process for Production of ICF Target Mandrels," Fusion Technol. **31**, 381 (1997).

[3-112] S.A. Letts, E.M. Fearon, S.R. Buckley, M.D. Saculla, L.M. Allison, R. Cook, "Fabrication of Polymer Shells Using a Depolymerizable Mandrel," Fusion Technol. **28**, 1797 (1995).

[3-113] B.W. McQuillan, A. Greenwood, "Microencapsulation Process Factors which Influence the Sphericity of 1 mm o.d. Poly(α-Methylsyrene) Shells for ICF," Fusion Technol. **35**, 194 (1999).

[3-114] M. Takagi, R. Cook, R. Stephens, J. Gibson, S. Paguio, "Decreasing Out-of-Round in Poly(α-Methylstyrene) Mandrels by Increasing Interfacial Tension," Fusion Technol. **38**, 46 (2001).

[3-115] B.W. McQuillan, F.H. Elsner, R.B. Stephens, L.C. Brown, "The Use of $CaCl_2$ and Other Salts to Improve Surface Finish and Eliminate Vacuoles in ICF Microencapsulated Shells," Fusion Technol. **35**, 198 (1999).

[3-116] R.L. McEachern, C.E. Moore, R.J. Wallace, "The Design, Performance, and Application of an Atomic Force Microscope-Based Profilometer," J. Vac. Sci. Technol. A **13**, 983 (1995).

[3-117] A.K. Knight, F.-Y Tsai, M.J. Bonino, and D.R. Harding, "Stability of Different Polyimide Capsule Materials for Use As ICF Targets," Fusion Sci. Technol. **45** (3) 187 (2004).

[3-118] F.-Y. Tsai, D.R. Harding, S.H. Chen, T.N. Blanton and E. L. Alfonso, "Effects of Process Conditions on the Quality and Properties of Vapor Deposited Polyimide Shells," Fusion Sci. Technol. **41** (3) 178 (2002).

[3-119] F.-Y. Tsai, "Engineering Vapor-Deposited Polyimides," Ph.D. thesis, University of Rochester, 2002.

[3-120] F.-Y. Tsai, E.L. Alfonso, S.-H. Chen, and D.R. Harding, "Mechanical Properties and Gas Permeability of Polyimide Shells Fabricated by the Vapor Deposition Method," Fusion. Technol. **38**, 83 (2000).

[3-121] C.C. Roberts, R.J. Orthion, A.E. Hassel, B.K. Parrish, S.R. Buckley, E. Fearon, S.A. Letts, and R.C. Cook, "Development of Polyimide Ablators for NIF: Analysis of Defects on Shells, A Nobel Smoothing Technique and Upilex Coatings," Fusion Technol. **38**, 94 (2000).

[3-122] E.L. Alfonso, F.-Y. Tsai, S.-H. Chen, R.Q. Gram, and D.R. Harding, "Fabrication of Polyimide Shells by Vapor Phase Deposition for Use as ICF Targets," Fusion Technol. **35**, 131 (1999).

[3-123] E.L. Alfonso, S.-H. Chen, R.Q. Gram, and D.R. Harding, "Properties of Polyimide Shells Made Using by Vapor Phase Deposition," J. Mater. Res. **13**, 2988 (1998).

[3-124] C.C. Roberts, S.A. Letts, M.D. Saculla, E.J. Hsieh, and R.C. Cook, "Polyimide Films from Vapor Deposition: Toward High Strength NIF Capsules," Fusion Technol. **35**, 138 (1999).

[3-125] S. Hann et al., "Increasing Robustness of Indirect Drive Capsule Designs Against Short Wavelength Hydrodynamic Instabilities," Phys. Plasma **12**, 056316 (2005) and M. Hermann, A. Fetterman, S. Haan, and J. Salmonson, "Optimization of Indirect Drive Capsules of the National Ignition Facility," presented at General Atomics, Oct. 26, 2004.

[3-126] S. Haan, "Update on Specifications for NIF Ignition Targets, and their Rollup into an Error Budget," 16th Target Fabrication Specialists Meeting, May 1-5, 2005, Scottsdale, Arizona, to be published in Fusion Sci. Technol. (2005).

[3-127] M. Herrmann, private communication on Graded Ge new power spectrum standard.

[3-128] S.A. Letts et al., "Fabrication of Polymer Shells Using a Depolymerizable Mandrel," Fusion Technol. **28**, 17977 (1995).

[3-129] A. Nikroo, J. Bousquet, R. Cook, B.W. McQuillan, R. Paguio, M. Takagi, "Progress in 2 mm Glow Discharge Polymer Mandrel Development for NIF," Fusion Sci. Technol. **45**, 165 (2004).

[3-130] R. Brusasco, M. Saculla, and R. Cook, "Preparation of Germanium Doped Plasma Polymerized Coatings as Inertial Confinement Fusion Target Ablators," J. Vac Sci. Technol. A **13**, 948 (1995).

[3-131] A. Nikroo and D. Woodhouse, "Bounce Coating Induced Domes on Glow Discharge Polymer Coated Shells," Fusion Technol. **35**, 202 (1999).

[3-132] A. Nikroo, J. Pontelandolfo, and E. Castillo, "Coating and Mandrel Effects on Fabrication of Glow Discharge Polymer NIF Scale Indirect Drive Capsules," Fusion Sci. Technol. **41**, 220 (2002).

[3-133] S.A. Letts, D.W. Myers, and L.A. Witt, "Ultrasmooth Plasma Polymerized Coatings for Laser Fusion Targets," J. Vac. Sci. Technol. **19**, 739 (1981).

[3-134] H. Huang et al., "Nondestructive Quantitative Dopant Profiling Technique by Contact Radiography" this report.

4. PUBLICATIONS

Items with GA/Schafer efforts supported by the contract for Target Component Fabrication and Technology Development Support are marked with an asterisk.

4.1. LIST OF PUBLICATIONS

Alfonso, E.L., J.S. Jaquez, and A. Nikroo, "Using Mass Spectrometry to Characterize Permeation Half-Life of ICF Targets," 16th Target Fabrication Specialists Meeting, May 1-5, 2005, Scottsdale, Arizona, to be published in Fusion Sci. Technol.; General Atomics Report GA-A25054 (2005).

Chen, K.C., R.C. Cook, H. Huang, S.A. Letts, and A. Nikroo, "Fabrication of Graded Germanium-Doped CH Shells," 16th Target Fabrication Specialists Meeting, May 1-5, 2005, Scottsdale, Arizona, to be published in Fusion Sci. Technol.; General Atomics Report GA-A25086 (2005).

Chen, K.C., and A. Nikroo, "Improvement of Surface Smoothness of Vapor-Deposited Polyimide Coatings Using a Plastic Mesh Container as Bounce Pan," 16th Target Fabrication Specialists Meeting, May 1-5, 2005, Scottsdale, Arizona, to be published in Fusion Sci. Technol.; General Atomics Report GA-A25087 (2005).

Frederick, C.A., R.R. Paguio, A. Nikroo, J.H. Hund, O. Acenas, and M. Thi, "Controlling the Pore Size and Gelation Time of Resorcinol Formaldehyde Foam for Fabrication of Direct Drive Targets for ICF Experiments," 16th Target Fabrication Specialists Meeting, May 1-5, 2005, Scottsdale, Arizona, to be published in Fusion Sci. Technol.; General Atomics Report GA-A25104 (2005).

Frey, D.T., D.T. Goodin, R.W. Stemke, R.W. Petzoldt, T.J. Drake, W. Egli, B.A. Vermillion, R. Klasen, M.M. Cleary, "REP-Rated Target Injection for Inertial Fusion Energy," Proc. 16th ANS Top. Mtg. on Technology of Fusion Energy, September 14-16, 2004, Madison, Wisconsin, in Fusion Sci. Technol. **47**, 1143 (2005); General Atomics Report GA-A24820 (2004).

Goodin, D.T., N.B. Alexander, G.E. Besenbruch, A.S. Bozek, L.C. Brown, L.C. Carlson, G.W. Flint, P. Goodman, J.D. Kilkenny, W. Maksaereekul, B.W. McQuillan, A. Nikroo, R.R. Paguio, R.W. Petzoldt, D.G. Schroen, J.D. Sheliak, J. Spalding, J.E. Streit, M.S. Tillack, B.A. Vermillion, "Developing a Commercial Production Process for 500,000 Targets per Day — A Key Challenge for Inertial Fusion Energy," 47th Annual Meeting of the Division of Plasma Physics, October 24-28, 2005, Denver, Colorado, to be published in Phys. Plasmas; General Atomics Report GA-A25258 (2005).

Goodin, D.T., A. Nobile, N.B. Alexander, R. Gallix, J.L. Maxwell, R.W. Petzoldt, W.S. Rickman, E.I. Valmianski, "Progress in Heavy Ion Driven Target Fabrication and Injection," presented at the 15th Intl. Symp. on Heavy Ion Inertial Fusion, June 7-11, 2004, Princeton, New Jersey, Nucl. Instr. and Methods in Physics Research A **544**, 34 (2005); General Atomics Report GA-A24727 (2004).

Goodin, D.T., N.B. Alexander, L.C. Brown, D.A. Callahan, P. Ebey, D.T. Frey, R. Gallix, D. Geller, C.R. Gibson, J. Hoffer, J.L. Maxwell, B.W. McQuillan, A. Nikroo, A. Nobile, C. Olson, R.W. Petzoldt, R. Raffray, W.S. Rickman, G. Rochau, D.G. Schroen, J. Sethian, J. Sheliak, J.E. Streit, M. Tillack, B.A. Vermillion, and E.I. Valmianski, "Demonstrating a Target Supply for Inertial Fusion Energy," Proc. 16th ANS Top. Mtg. on Technology of Fusion Energy, September 14-16, 2004, Madison, Wisconsin, in Fusion Sci. Technol. **47**, 1131 (2005); General Atomics Report GA-A24816 (2004).

Huang, H., R.B. Stephens, S.A. Eddinger, J. Gunther, A. Nikroo, K.C. Chen, H. Xu "Nondestructive Quantitative Dopant Profiling Technique by Contact Radiography," 16th Target Fabrication Specialists Meeting, May 1-5, 2005, Scottsdale, Arizona, to be published in Fusion Sci. Technol.; General Atomics Report GA-A25057 (2005).

Huang, H., R.B. Stephens, J.B. Gibson, and I. Valmianski, "3D Surface Reconstruction of ICF Shells after Full Surface Spheremapping," 16th Target Fabrication Specialists Meeting, May 1-5, 2005, Scottsdale, Arizona, to be published in Fusion Sci. Technol.; General Atomics Report GA-A25056 (2005).

Hund, J.F., R.R. Paguio, C.A. Frederick, A. Nikroo, and M. Thi, "Silica, Metal Oxide, and Doped Aerogel Development for Target Applications," 16th Target Fabrication Specialists Meeting, May 1-5, 2005, Scottsdale, Arizona, to be published in Fusion Sci. Technol.; General Atomics Report GA-A25093 (2005).

Jaquez, J.S., E.L. Alfonso, and A. Nikroo, "Development of Sputtered Coated Glass Permeation Barrier," 16th Target Fabrication Specialists Meeting, May 1-5, 2005, Scottsdale, Arizona, to be published in Fusion Sci. Technol.; General Atomics Report GA-A25123 (2005).

Kaae, J.L., D.M. Woodhouse, "The Effect of Corners on Electroplating of Hohlraum Mandrels," 16th Target Fabrication Specialists Meeting, May 1-5, 2005, Scottsdale, Arizona, to be published in Fusion Sci. Technol.; General Atomics Report GA-A25077 (2005).

Mauldin, M.P., A.L. Greenwood, M.N. Kittelson, C.H. Shearer, J.N. Smith, Jr., and D.M. Woodhouse, "Micromachining of Fast Ignition Targets," 16th Target Fabrication Specialists Meeting, May 1-5, 2005, Scottsdale, Arizona, to be published in Fusion Sci. Technol.; General Atomics Report GA-A25078 (2005).

Nikroo, A., J. Pontelandolfo, A.L. Greenwood, J.L. Stillwell, D.A. Callahan, "Fabrication of Capsules with an Angle Dependent Gold Shim for Hoholraum Drive Symmetry Correction," presented at the 15th Intl. Symp. on Heavy Ion Inertial Fusion, June 7-11, 2004, Princeton, New Jersey, Nucl. Instr. and Methods in Physics Research A **544**, 42 (2005); General Atomics Report GA-A24774 (2004).

Paguio, R.R., S.P. Paguio, C.A. Frederick, A. Nikroo, and O. Acenas, "Improving the Yield of Target Quality OMEGA Size Pams Mandrels by Modifying Emulsion Components," 16th Target Fabrication Specialists Meeting, May 1-5, 2005, Scottsdale, Arizona, to be published in Fusion Sci. Technol.; General Atomics Report GA-A25122 (2005).

Petzoldt, R.W., R. Gallix, D.T. Goodin, E. Valmianski, W.S. Rickman, and The Aries Team, "Materials Selection for Heavy Ion Fusion Hohlraums," to be published in Fusion Sci. Technol.; General Atomics Report GA-A24923 (2005).

Petzoldt, R.W., K. Jonestrask, "IFE Target Injection Tracking and Position Prediction Update," Proc. 16th ANS Top. Mtg. on Technology of Fusion Energy, September 14-16, 2004, Madison, Wisconsin, in Fusion Sci. Technol. **47**, 1126 (2005); General Atomics Report GA-A24817 (2004).

Project Staff, "Target Injection, Tracking, Fabrication and Characterization Development in Support of the NRL Laser-Plasma Program, Annual Report to the U.S. Department of Navy, April 18, 2004 through April 17, 2005," General Atomics Report GA-A25105 (2005).

Steinman, D.A., R.B. Stephens, and M.L. Hoppe, "A Novel Technique for Precisely Measuring the Thickness of Witness Plates," 16th Target Fabrication Specialists Meeting, May 1-5, 2005, Scottsdale, Arizona, to be published in Fusion Sci. Technol.; General Atomics Report GA-A25059 (2005).

Stephens, R.B., S.P. Hatchett, M. Tabak, C. Stoeckl, H. Shiraga, S. Fujioka, M. Bonino, A. Nikroo, R. Petraso, T.C. Sangster, J. Smith, and K.A. Tanaka, "Implosion Hydrodynamics of Fast Ignition Targets," presented at the 46th Annual Meeting of Division of Plasma Physics, November 14-19, 2004, Savannah, Georgia, and to be published in Phys. Plasmas; General Atomics Report GA-A24906 (2005).

Stephens, R.B., G. Flint, "Precise Characterization of NIF Shell Opacity," Bull. Am. Phys. Soc. **49**, 284 (2004).

Stephens, R.B., D.A. Steinman, M.L. Hoppe, "White Light Interferometry for the Optical Characterization of Transparent ICF Shells," 16th Target Fabrication Specialists Meeting, May 1-5, 2005, Scottsdale, Arizona, to be published in Fusion Sci. Technol.; General Atomics Report GA-A25055 (2005).

Vermillion, B.A., B.W. McQuillan, L.C. Brown, D.T. Goodin, R. Paguio, J.E. Streit, D.G. Schroen, P.C. Goodman, W. Maksaereekul, "Mass Production Methods for IFE Targets," Proc. 16th ANS Top. Mtg. on Technology of Fusion Energy, September 14-16, 2004, Madison, Wisconsin, in Fusion Sci. Technol. **47**, 1139 (2005); General Atomics Report GA-A24827 (2004).

Wilkens, H.L., J. Gunther, M.P. Mauldin, A. Nikroo, J.R. Wall, D.R. Wall, and R.J. Wallace, "Progress in Coating Multi-Layered Cocktail Hohlraums," 16th Target Fabrication Specialists Meeting, May 1-5, 2005, Scottsdale, Arizona, to be published in Fusion Sci. Technol.; General Atomics Report GA-A25063 (2005).

Wilkens, H.L., A.V. Hamza, A. Nikroo, and N.E. Teslich, "Investigating the Potential of Using Focused Ion Beam Technology to Bore Holes in and Attach Fill-Tubes to a Beryllium Ablator," 16th Target Fabrication Specialists Meeting, May 1-5, 2005, Scottsdale, Arizona, to be published in Fusion Sci. Technol.; General Atomics Report GA-A25062 (2005).

Xu, H., A. Nikroo, J.R. Wall, R. Doerner, M. Baldwin, and J.H. Yu, "Be Coatings on Spherical Surface for NIF Target Development," 16th Target Fabrication Specialists Meeting, May 1-5, 2005, Scottsdale, Arizona, to be published in Fusion Sci. Technol.; General Atomics Report GA-A25058 (2005).

4.2. LIST OF PRESENTATIONS

Alexander, N.B., "Laser Welding of Microholes in Beryllium," 16th Target Fabrication Specialists Meeting, Scottsdale, Arizona, May 1-5, 2005.

Alfonso, N., "Fill Tube Target Development," 16th Target Fabrication Specialists Meeting, Scottsdale, Arizona, May 1-5, 2005.

Alfonso, N., "Glass Permeation Barrier Characterization by Mass Spectrometry," 16th Target Fabrication Specialists Meeting, Scottsdale, Arizona, May 1-5, 2005.

Beg, F., "Compact X-pinch X-ray Source for Characterization of Inertial Confinement Capsules," 16th Target Fabrication Specialists Meeting, Scottsdale, Arizona, May 1-5, 2005.

Bernat, T., "Ignition Target Fabrication and Fielding for the National Ignition Facility," 4th Intl. Conf. on Inertial Fusion Sciences and Applications, Biarritz, France, September 4–9, 2005.

*Bittner, D., "D-T Absorption Coefficient Measurements," 16th Target Fabrication Specialists Meeting, Scottsdale, Arizona, May 1-5, 2005.

Bozek, A., "Update on Mass Production Layering," High Average Power Laser (HAPL) Meeting, LLNL, Livermore, California June 20–21, 2005.

*Breden, E., "Equation of State Target Characterization Challenges," 16th Target Fabrication Specialists Meeting, Scottsdale, Arizona, May 1-5, 2005.

*Burmann, J., "Fill Tube Targets for Room Temperature Transport," 16th Target Fabrication Specialists Meeting, Scottsdale, Arizona, May 1-5, 2005.

*Carter, S., "Assembly of ICF Targets," 16th Target Fabrication Specialists Meeting, Scottsdale, Arizona, May 1-5, 2005.

Chen, K.C., "Fabrication of Graded Germanium-Doped CH Shells," 16th Target Fabrication Specialists Meeting, Scottsdale, Arizona, May 1-5, 2005.

Chen, K.C., "Vapor Deposited Polyimide Shells with Improved Surface Smoothness," 16th Target Fabrication Specialists Meeting, Scottsdale, Arizona, May 1-5, 2005.

Eddinger, S., "Design of Ultra-High Precision Radiography System," 16th Target Fabrication Specialists Meeting, Scottsdale, Arizona, May 1-5, 2005.

Flint, G., "Integration of IFE Beamlet Co-Alignment, Target Tracking, and Beam Steering," VTC with NRL, 2005.

Fredrick, C., "Controlling the Pore Size and Gelation Time of Resorcinol Formaldehyde Foam for Fabrication of Direct Drive Targets for ICF Experiments," 16th Target Fabrication Specialists Meeting, Scottsdale, Arizona, May 1-5, 2005.

Fredrick, C., "Controlling the Pore Size of Resorcinol Formaldehyde Foam Targets for Fusion Experiments," Materials Research Society, 2005.

Gallix, R., "Concept for a 1000 MW ZPinch IFE Power Plant," 4th Intl. Conf. on Inertial Fusion Sciences and Applications, Biarritz, France, September 4–9, 2005.

Gallix, R., "Proposed Design and Fabrication Concepts for Z-Pinch Wire Arrays," 16th Target Fabrication Specialists Meeting, Scottsdale, Arizona, May 1-5, 2005.

Gibson, J., "Full Shell AFM Spheremapping and 3-D Surface Reconstruction Improved Capability for Thick Shell Wall Measurements," 16th Target Fabrication Specialists Meeting, Scottsdale, Arizona, May 1-5, 2005.

Gibson, J., "Full Shell AFM Spheremapping and 3-D Surface Reconstruction Improved Capability for Thick Shell Wall Measurements," 16th Target Fabrication Specialists Meeting, Scottsdale, Arizona, May 1-5, 2005.

Giraldez, E., "Fabrication of Hemispherical Cryogenic Liquid Fuel Capsule Components For Z-Pinch-Driven Fast Ignition Experiments," 16th Target Fabrication Specialists Meeting, Scottsdale, Arizona, May 1-5, 2005.

Goodin, D., "An Introduction to the Target Fabrication, Injection, and Engagement Sessions," High Average Power Laser (HAPL) Meeting, LLNL, Livermore, California June 20–21, 2005.

Goodin, D., "Status of Target Fabrication (and Injection)," High Average Power Laser (HAPL) Meeting, LLNL, Livermore, California June 20–21, 2005.

Goodin, D., "Summary of Target Fabrication and Injection Workshop," US/Japan Workshop, San Diego, California, March 21–22, 2005.

Goodin, D., "Target Manufacturing – A 'Grand Challenge' for IF," 4th Intl. Conf. on Inertial Fusion Sciences and Applications, Biarritz, France, September 4–9, 2005.

Goodin, D., "The Current Development Status of Target Fabrication and Injection for IFE," 16th Target Fabrication Specialists Meeting, Scottsdale, Arizona, May 1-5, 2005.

Greenwood, A., "Application of Thermal Gravimetric Analysis to Target Fabrication," 16th Target Fabrication Specialists Meeting, Scottsdale, Arizona, May 1-5, 2005.

*Grine-Jones, S., "Recent Advancements in ICF Target Assembly Techniques at SNL," 16th Target Fabrication Specialists Meeting, Scottsdale, Arizona, May 1-5, 2005.

*Holt, R., "The Importance of Target Characterization Reports," 16th Target Fabrication Specialists Meeting, Scottsdale, Arizona, May 1-5, 2005.

Hoppe, M., "Polishing of BE Capsules to Meet NIF Specifications," 4th Intl. Conf. on Inertial Fusion Sciences and Applications, Biarritz, France, September 4–9, 2005.

*Hsieh, E., "Techniques to Fabricate a 1.5 μm Thick 12 x 11 mm Free Standing Cu/Au Cylindrical Shell," 16th Target Fabrication Specialists Meeting, Scottsdale, Arizona, May 1-5, 2005.

Huang, H., "3D Surface Reconstruction from Spheremapping Traces," 16th Target Fabrication Specialists Meeting, Scottsdale, Arizona, May 1-5, 2005.

Huang, H., "Measuring Dopant Concentration in Graded ICF Targets through Quantitative Contact Radiography," 16th Target Fabrication Specialists Meeting, Scottsdale, Arizona, May 1-5, 2005.

Huang, H., "Quantitative Radiography of HED Targets," 4th Intl. Conf. on Inertial Fusion Sciences and Applications, Biarritz, France, September 4–9, 2005.

Huang, H., "Radiographic Dimension Measurement of Dry DVB Foam Shells," High Average Power Laser (HAPL) Meeting, LLNL, Livermore, California June 20–21, 2005.

Hund, J., "Silica and Metal Oxide Aerogel Development at General Atomics," 16th Target Fabrication Specialists Meeting, Scottsdale, Arizona, May 1-5, 2005.

Hund, J., "Silica and Metal Oxide Aerogel Materials for Target Applications," 2005 High-Energy-Density-Physics (HEDP) Summer School, Berkeley, California, August 7-13, 2005.

Jaquez, J., "Development of Sputtered Coated Glass Permeation Barrier," 16th Target Fabrication Specialists Meeting, Scottsdale, Arizona, May 1-5, 2005.

Kaae, J., "Machining of Three-Dimensional Shapes for HED," JOWOG Conf., February 21, 2005.

Kaae, J., "The Effect of Interior and Exterior Radii on the Nature of Gold Electroplating of Hohlraum Mandrels," 16th Target Fabrication Specialists Meeting, Scottsdale, Arizona, May 1-5, 2005.

Kilkenny, J., "The Role of Experimental Science in ICF," Teller Award Lecture, 4th Intl. Conf. on Inertial Fusion Sciences and Applications, Biarritz, France, September 4–9, 2005.

Kilkenny, J.D., "Innovation in Target Fabrication has Increased the Margin for Ignition. Further Innovation and Transition to Production is Needed," presented at the National Ignition Planning at LLNL, January 26, 2005.

Kilkenny, J.D., "Prospects for IFE," 26th Anniversary Meeting and Symposium on Fusion and Energy Policy, Fusion Power Associates, October 11-12, 2005.

*Krych, W., "Doped TPX Foams and Embedded Foil Foams for the Z Accelerator at Sandia National Labs," 16th Target Fabrication Specialists Meeting, Scottsdale, Arizona, May 1-5, 2005.

Lundgren, E., "Producing Gas Filled Beryllium Shells Using a High Pressure Glue Sealing Apparatus," 16th Target Fabrication Specialists Meeting, Scottsdale, Arizona, May 1-5, 2005.

Mathias, P., "Phase Equilibria and Thermodynamic Properties of the Sulfur-Iodine Cycle," AIChE Spring Meeting Atlanta, Georgia, April 12, 2005.

Mathias, P., "Quantitative Analysis of the Sulfur-Iodine Cycle Through Process Simulation," AIChE Spring Meeting Atlanta, Georgia, April 12, 2005.

Mauldin, M., "Micromachining of Inertial Confinement Fusion Fast Ignition Targets," 2005 High-Energy-Density-Physics (HEDP) Summer School, Berkeley, California, August 7-13, 2005.

Mauldin, M., "The Role of Micromachining in Target Fabrication for Fast Ignition Experiment," 16th Target Fabrication Specialists Meeting, Scottsdale, Arizona, May 1-5, 2005.

McQuillan, B., "Some Potential Solutions to the Overcoat Survival Issue," High Average Power Laser (HAPL) Meeting, LLNL, Livermore, California June 20–21, 2005.

Miller, W., "Management Review of the IFT Quality System," Qtr. Management Review 2005.

Miller, W., "Quality Management for Target Fabrication Production: ISO 9001:2000," JOWOG Conf., Albuquerque, New Mexico, 2005.

Miller, W.J., "Management Review of the IFT Quality System," presented at the Quarterly Review of the IFT QMS System (ISO 9001:2000).

*Motta, B., "Diamond Turned Thick Aluminum Coatings on Lithium Fluoride Substrates," 16th Target Fabrication Specialists Meeting, Scottsdale, Arizona, May 1-5, 2005.

Paguio, R., "Fabrication Capabilities for Foam Targets Used in ICF Experiments," 16th Target Fabrication Specialists Meeting, Scottsdale, Arizona, May 1-5, 2005.

Paguio, S., "Improving Pams Mandrel Quality by Increasing the Interfacial Surface Tension of the Emulsion," 16th Target Fabrication Specialists Meeting, Scottsdale, Arizona, May 1-5, 2005.

Petzoldt, R., "A 50 m/s Mechanical Injector Should Significantly Reduce IFE Target Injection Costs," Video Webcam with NRL, February 15, 2005.

Petzoldt, R., "Target Injection Update," High Average Power Laser (HAPL) Meeting, LLNL, Livermore, California June 20–21, 2005.

Petzoldt, R., "Update on Various Target Issue," High Average Power Laser (HAPL) Meeting, LLNL, Livermore, California June 20–21, 2005.

*Russell, C., "Dual Theta Assembly and Characterization System," 16th Target Fabrication Specialists Meeting, Scottsdale, Arizona, May 1-5, 2005.

*Schroen, D., "Overview of Target Fabrication in Support of Sandia National Laboratories," 16th Target Fabrication Specialists Meeting, Scottsdale, Arizona, May 1-5, 2005.

Sheliak, J., "Recent and On-going IFE Studies of DT Solid Layering Inside Varying Cell Types," Seminar at General Atomics, San Diego, California, January 19, 2005.

Steinman, D.A., "Witness Plate Thickness Measurement," 16th Target Fabrication Specialists Meeting, Scottsdale, Arizona, May 1-5, 2005.

Stemke, R., "HWA's When is One Required?" Seminar at GA, January 19, 2005.

*Stefanescu, D., "Monitoring H2O Ice Condensation on Cryogenic Targets Using a Quartz Crystal Deposition Device," 16th Target Fabrication Specialists Meeting, Scottsdale, Arizona, May 1-5, 2005.

Stephens, R.B., "Design Review for Precision Radiograph," presented to ICF managers at LLNL, Livermore, California, February 1, 2005.

Stephens, R.B., "Fast Ignition — Target Design, Fuel Assembly, and Hydro Experiments," presented to the Campaign-10 Meeting on Pulsed Power and Fast Ignition/Petawatt Lasers at UR/LLE, Rochester, New York, October 5–6, 2005.

Stephens, R.B., "Fast Ignition Targets and Experiments," US/Japan Workshop, San Diego, California, March 21–22, 2005.

Stephens, R.B., "Fuel Assembly Considerations for the Fast Ignition Target," Frontier Science Research Conf. on Laser-Matter Interaction in La Jolla, California, October 29–30, 2005.

Stephens, R.B., "High Energy Electron Transport in Solids," 4th Intl. Conf. on Inertial Fusion Sciences and Applications, Biarritz, France, September 4–9, 2005.

Stephens, R.B., "Precise Radiography Measurements on NIF shells," presented to ICF managers at LLNL, Livermore, California, October 27, 2004.

Stephens, R.B., "Quantitative Radiographic Characterization of HEDP Targets," JOWOG37, Sandia National Laboratories, Albuquerque, New Mexico, February 21–25, 2005.

Stephens, R.B., "US-Japan Collaboration – Fast Ignition and HEDP 2006 thru 2010," presentation to DOE-OFES, Germantown, February 4, 2005.

Stephens, R.B., "X-Ray Opacity Uiformity Validation of NIF Cryo-Ignition Shells," 16th Target Fabrication Specialists Meeting, Scottsdale, Arizona, May 1–5, 2005.

*Stewart, J., "Capsule Tritium Fill Fixture and Transporter Unit," 16th Target Fabrication Specialists Meeting, Scottsdale, Arizona, May 1-5, 2005.

*Stolp, J., "Applying Database Technology to ISO 9001," 16th Target Fabrication Specialists Meeting, Scottsdale, Arizona, May 1-5, 2005.

Vermillion, B., "Divinylbenzene Foam Shell Studies: Improving Non-Concentricity and Yield for IFE Target Production," High Average Power Laser (HAPL) Meeting, LLNL, Livermore, California June 20–21, 2005.

Vermillion, B., "Foam Shells, Non-Concentricity, Overcoats, and Characterization Methods," High Average Power Laser (HAPL) Meeting, LLNL, Livermore, California June 20–21, 2005.

Vermillion, B., "Target Fabrication Activities in Support of the HAPL Program and IFE," 2005 High-Energy-Density-Physics (HEDP) Summer School, Berkeley, California, August 7-13, 2005.

Vermillion, B.A., "Meeting 'Ignition Quality' Requirements for IFE Targets: Improving Wall Thickness Uniformity in Divinylbenzene Foam Shells," 16th Target Fabrication Specialists Meeting, Scottsdale, Arizona, May 1-5, 2005.

West, M., "Simulation of Electron Beam Analysis of Inertial Confinement Fusion Targets," 16th Target Fabrication Specialists Meeting, Scottsdale, Arizona, May 1-5, 2005.

Wilkens, H., "Developments in Sputtering Multi-Layered Depleted Uranium and Gold for use in 'Cocktail' Hohlraums," 2005 High-Energy-Density-Physics (HEDP) Summer School, Berkeley, California, August 7-13, 2005.

Wilkens, H., "Multi-layered Depleted Uranium and Gold Cocktail Hohlraums for Research in Inertial Confinement Fusion," 12th Intl. Conf. on Composites/Nano Engineering (ICCE-12), Tenerife, Canary Islands, Spain, August 1-6, 2005.

Wilkens, H., "Progress in Coating Multi- Layered Cocktail Hohlraum," 16th Target Fabrication Specialists Meeting, Scottsdale, Arizona, May 1-5, 2005.

Wilkens, H., "Understanding the Fabrication Process of Multilayered Cocktail Coatings," 47th Annual Mtg. of the Divison of Plasma Physics, Denver, Colorado, October 24-28, 2005.

Wilkens, H., "Using Focused Ion Beam Technology to Drill Holes in Cryogenic Inertial Confinement Fusion Targets," 16th Target Fabrication Specialists Meeting, Scottsdale, Arizona, May 1-5, 2005.

Wong, B., "Construction Materials Development for Sulfur-Iodine Thermochemical Water Splitting Process for Hydrogen Production," AIChE Spring Meeting Atlanta, Georgia, April 12, 2005.

Wong, B., "Corrosion and Crack Growth Studies of Heat Exchanger Candidate Structural Materials in HIx," High Temperature Heat Exchanger (HTHX), UNLV Research Foundation Nuclear Hydrogen Initiative, Project Quarterly University Consortium Meeting, University of California, Berkeley, California, September 12, 2005.

Wong, B., "Corrosion Studies of Heat Exchanger Candidate Structural Materials in HIx Environment as Functions of Metallurgical Variables," presentation at UNLV in December 2004.

Wong, B., "HIx is Very Corrosive. Success of the S-I Cycle Depends on Finding Suitable Materials of Construction," Presentation @ ORNL, 2005.

Wong, B., "Progress Update — Corrosion Studies of Heat Exchanger Candidate Structural Materials in HIx Experiments," UNLV Qtr. Mtg., 2005.

Wong, B., "To Identify Pilot and Demo Scale Construction Materials for HI Decompositon," INERI Meeting, 2005.

Xu, H., "Be Coatings on Spherical Surface for NIF Target Development," 16th Target Fabrication Specialists Meeting, Scottsdale, Arizona, May 1-5, 2005.

Xu, H., "Be Coatings on Spherical Surface for NIF Target Development," 2005 High-Energy-Density-Physics (HEDP) Summer School, Berkeley, California, August 7-13, 2005.

ACKNOWLEDGMENT

This report of work was prepared for the U.S. Department of Energy under Contract No. DE-AC03-01SF22260.